WIRELESS ANTENNA SENSORS FOR BOILER CONDITION MONITORING

by

FRANCK ERIC MBANYA TCHAFA

Presented to the Faculty of the Graduate School of
The University of Texas at Arlington in Partial Fulfillment
of the Requirements
for the Degree of

DOCTOR OF PHILOSOPHY

THE UNIVERSITY OF TEXAS AT ARLINGTON

August 2018

DEDICATIONS

This dissertation is dedicated to my parents–Emilienne Tchafa and Thomas Tchafa–who have supported me throughout my undergraduate and graduate studies. I am forever grateful for their endless love, support, and encouragement that cannot be put into writing.

ACKNOWLEDGEMENTS

This dissertation could not have been written without Dr. Haiying Huang, who not only served as my Ph.D. supervisor but also encouraged and challenged me throughout my academic program. I thank her for helping me develop my scientific acuity by accepting nothing but the very best. Her passion and attitude toward research greatly impacted me.

Besides my supervisor, I would like to thank my Ph.D. committee members–Dr. Kent Lawrence, Dr. Bo P. Wang, Dr. Ashfaq Adnan, and Dr. Ankur Jain–for their interest in my research and their academic advice. They and other faculty members at the University of Texas at Arlington provided quality teaching. I wholeheartedly thank them all.

I would like to thank my friends and colleagues at the Advanced Sensor Technology Laboratory. I thank Dr. Jun Yao for his collaboration. To Jalal Sola, Abhay Singh, and Kranthi Balusu, I thank you for your friendship and advice more than I can express on paper.

Finally, my joy knows no bounds in expressing my profound gratitude to my wonderful wife–Alimatou Tchafa, a woman with a golden heart–for supporting and encouraging me along this journey. I also thank several of my family members who have helped and motivated me throughout my studies.

August 28, 2018

ABSTRACT

WIRELESS ANTENNA SENSORS FOR BOILER CONDITION MONITORING

Franck Eric Mbanya Tchafa, Ph.D.
Supervising professor: Haiying Huang, Ph.D.

Structural Health Monitoring (SHM) is a vital technology that implements real-time condition monitoring or damage detection mechanisms for the safety assurance of structural systems such as power stations, aircrafts, bridges, dams, buildings, large machinery, and more. Without proper and timely maintenance, mechanical systems are prone to failures since they experience detrimental factors such as harsh environments, excessive loads, and vibrations. Several sensing technologies exist for SHM applications. Patch antennas are among the list of these technologies, and they are an attractive choice due to their compact size, light weight, ease of manufacturing, and low fabrication cost. Patch antennas have been studied not only for wireless communication but as sensors for condition monitoring. A typical patch antenna, consisting of a dielectric substrate, a radiation patch, and a ground plane, is an electromagnetic (EM) resonator with specific fundamental frequencies. These frequencies depend on the radiation patch dimensions and the antenna's effective dielectric constant, which is a contribution of the dielectric constants of all layers (i.e., substrate and superstrate) and their respective thicknesses. Any change in the antenna dimensions or the material properties due to temperature, mechanical strain, and ash

accumulation will cause a shift in the antenna resonant frequencies. Thus, it is possible to use patch antennas as sensors.

The objectives of this research are to (a) extract multiple measurands (i.e., temperature, strain, ash thickness) from the antenna's response; (b) demonstrate wireless interrogation of passive antenna sensors without electronics; and (c) establish a procedure for characterizing the dielectric properties of substrates. Measuring the dielectric property is important as substrate materials could be engineered based on the trade-off between the sensitivity of the antenna sensor to the three sensing parameters to achieve optimal sensor performance and facilitate simple data processing. Furthermore, these dielectric properties could be used in simulation tools to perform parametric studies on the substrate properties and to define the design space.

In this dissertation, we demonstrate simultaneous measurement of multiple parameters using a single patch antenna. For simultaneous strain and temperature sensing, we exploit the two fundamental resonant frequencies of the antenna. The theoretical relationship between the antenna resonant frequency shifts, the temperature, and the applied strain was first established to guide the selection of the dielectric substrate, based on which an antenna sensor with a rectangular radiation patch was designed and fabricated. A tensile test specimen instrumented with the antenna sensor was subjected to thermo-mechanical tests. Experiment results validated the theoretical predictions that the normalized antenna resonant frequency shifts are linearly proportional to the applied strain and temperature changes. By comparing the temperature and strain inversely determined from the measured frequencies to actual thermocouple and strain gauge readings, we achieved measurement uncertainties of $\pm 0.4^{o}C$ and $\pm 17.22\ \mu\varepsilon$ for temperature and strain measurements, respectively.

Furthermore, we demonstrate simultaneous measurement of temperature and superstrate thickness using the antenna sensor. Since the temperature causes a change in the material

properties, and the superstrate thickness variation causes a change in the antenna effective dielectric constant, the superstrate thickness and the temperature can be inversely determined simultaneously from the antenna frequencies. To demonstrate simultaneous measurement of these two parameters, the antenna sensor was designed, fabricated, and tested to characterize its performance. Using ash from charcoal briquettes as a superstrate, we achieved measurement uncertainties of ±0.58°C and ±58.05 μm for temperature and superstrate thickness, respectively.

We also demonstrate wireless interrogation of a high-temperature antenna sensor without electronics. This specific achievement is a collaboration with Dr. Jun Yao. The sensor node is entirely passive and consists of an Ultra-wide Band (UWB) transmitting/receiving (Tx/Rx) antenna and a microstrip patch antenna serving as the temperature sensing element. A microstrip transmission line connecting the UWB Tx/Rx antenna and the antenna sensor delays the signal reflected from the sensing element and separates it from the background clutter. The operation principle of the wireless sensing scheme, the design, and simulations of the sensor node circuitry are discussed in this research. Furthermore, a digital signal processing algorithm that extracts the antenna resonant frequency from the wirelessly received signal is also described. Temperature tests were conducted to validate the performance of the wireless antenna sensor inside a high-temperature furnace.

Finally, the broad range of microwave applications requires detailed knowledge of the dielectric properties of substrate materials. Due to the variability that exists in the material properties of fabricated printed circuit boards (PCBs), we investigate the use of a microstrip line resonator for dielectric measurement of PCBs. Using Rogers 3006 commercial PCB, we obtained a good agreement between the manufacturer specified dielectric constant of 6.15 and the measured dielectric constant of 6.17.

TABLE OF CONTENTS

DEDICATIONS iii

ACKNOWLEDGEMENTS iv

ABSTRACT v

LIST OF ILLUSTRATIONS xii

INTRODUCTION 1

CHAPTER 1: BACKGROUND 5

1.1 Introduction to structural health monitoring 5

1.2 A review of wireless sensors 6

1.2.1 Active wireless sensors 6

1.2.2 Passive wireless sensors 7

1.2.2.1 Wireless RFID enabled sensors 7

1.2.2.2 Wireless surface acoustic wave sensors 10

1.2.2.3 Wireless inductively coupled sensors 12

1.3 A review of the wireless interrogation mechanisms of antenna sensors 14

1.4 A review of the superstrate effect on the antenna performance 16

1.5 A review of the dielectric permittivity measurement of PCBs 18

2. Research objectives and impacts 20

CHAPTER 2: ANALYSIS OF PATCH ANTENNAS FOR SENSING APPLICATIONS 21

CHAPTER 3: MICROSTRIP PATCH ANTENNA FOR SIMULTANEOUS STRAIN AND TEMPERATURE SENSING 25

3.1 Introduction 25

3.2 Antenna sensor design and fabrication 26

3.2.1 Substrate selection and antenna design 26

3.2.2 Sensor fabrication 28

3.3 Instrumentation and experimental setup 30

3.4 Results and discussion 32

3.5 Conclusion 37

CHAPTER 4: MICROSTRIP PATCH ANTENNA FOR SIMULTANEOUS SUPERSTRATE THICKNESS AND TEMPERATURE SENSING 38

4.1 Introduction 38

4.2 Principle of operation 38

4.3 Antenna sensor design and fabrication 40

4.4 Instrumentation and experimental setup 46

4.5 Results and discussion 47

4.5.1 Results obtained using Rogers 3003 as superstrate 47

4.5.2 Results obtained using ash from charcoal briquettes as superstrate 51

4.6 Conclusion 55

CHAPTER 5: FAR-FIELD INTERROGATION OF A MICROSTRIP PATCH ANTENNA TEMPERATURE SENSOR WITHOUT ELECTRONICS 56

5.1 Introduction 56

5.2 Principle of operation 57

5.3 Sensor node implementation 59

5.3.1 Design of temperature antenna sensor 59

5.3.2 Design of the UWB Tx/Rx microstrip antenna 62

5.4 Instrumentation and experimental setup 65

5.5 Digital signal processing 68

5.6 Results and discussion 69

5.7 Conclusion 72

CHAPTER 6: MEASUREMENT OF THE DIELECTRIC PERMITTIVITY OF PRINTED CIRCUIT BOARD USING MICROSTRIP RESONATORS 73

6.1 Introduction 73

6.2 Theory of the measurement technique 73

6.2.1 Calculation of the dielectric constant 75

6.2.2 Calculation of the dissipation factor 76

6.3 Design and fabrication of the microstrip line resonator 79

6.4 Instrumentation and experimental setup 81

6.5 Discussion 82

CHAPTER 7: CONCLUSIONS AND FUTURE WORK 84

7.1 Conclusions 84

7.2 Future work 85

REFERENCES 87

LIST OF ILLUSTRATIONS

Figure 2.1. Configuration of a rectangular patch antenna. The radiation patch and the ground plane are made of conductive materials. 21

Figure 3.1. The physical design of the antenna sensor edge fed by a microstrip transmission line. 27

Figure 3.2. A dog-bone sample instrumented with the antenna sensor; (a) front view; (b) back view. 28

Figure 3.3. A comparison between simulated and measured S_{11} curves of the antenna sensor. . 29

Figure 3.4. (a) The experimental setup for thermo-mechanical testing of the antenna sensor (b) dog-bone specimen with bonded antenna sensor and thermocouple. 31

Figure 3.5. Strain measurements along the loading and transverse directions under different loading levels. 32

Figure 3.6. Effect of strain on the resonant frequencies of the patch antenna sensor: (a) measured S_{11} parameters of the TM_{010} mode at different strain levels; (b) linear shifts of the normalized antenna frequency with the applied strain. 33

Figure 3.7. Effect of temperature on the resonant frequencies of the patch antenna sensor: (a) measured S_{11} parameters of the TM_{010} mode at different temperatures; (b) linear shifts of the normalized frequency with the temperature increase. 34

Figure 3.8. The normalized antenna frequency shifts with the applied strain under different temperatures; (a) TM_{010} mode and (b) TM_{001} mode. 35

Figure 3.9. Differences between (a) temperature and (b) strain inversely determined from the normalized frequency shifts and those measured using a thermocouple and strain gauges respectively. 36

Figure 4.1. An illustration of a microstrip patch antenna temperature sensor covered with a superstrate dielectric layer. 39

Figure 4.2. (a) The three-dimensional (3D) model of the superstrate thickness and temperature sensor simulated using Sonnet Pro; (b) physical design of the antenna sensor fed by an inset-feed microstrip transmission line. 40

Figure 4.3. The simulated effect of superstrate dielectric constant on the resonant frequencies of the patch antenna and the effective dielectric constant derived from the frequency shift. 42

Figure 4.4. The simulated effect of superstrate thickness on the antenna resonant frequencies. . 43

Figure 4.5. The simulated effect of temperature on the antenna resonant frequencies. 43

Figure 4.6. The simulated effect of temperature and superstrate thickness variations on the resonant frequencies of the patch antenna sensor: (a) f_{10} frequency and (b) f_{01} frequency. 43

Figure 4.7. (a)The antenna sensor fabricated on Rogers 3210 printed circuit board (PCB) using print-etching technique; and (b) a comparison between simulated and measured S_{11} curves of the antenna sensor. 45

Figure 4.8. The experimental setup for characterizing the antenna sensor. 45

Figure 4.9. The thermocouple temperature measurements during the antenna sensor characterization. 47

Figure 4.10. The measured effect of temperature on the resonant frequencies of the microstrip patch antenna sensor fabricated on Rogers 3210 PCB: (a) S_{11} curves of the f_{10} frequency at different

temperatures; (b) linear shifts of the antenna sensor's resonant frequencies with temperature increase. 48

Figure 4.11. The measured effect of Rogers 3003 superstrate thickness on the resonant frequencies of the antenna sensor at 23°C: (a) S_{11} curves of the f_{10} frequency with different thicknesses of superstrate; (b) the antenna frequencies shifts with an increase in superstrate thickness..... 49

Figure 4.12. The measured effects of temperature and superstrate thickness on the (a) f_{10} and (b) f_{01} antenna resonant frequencies. Rogers 3003 dielectric material is serving as superstrate..... 49

Figure 4.13. A comparison between Rogers 3003 superstrate thickness and temperature inversely determined from the antenna frequencies and actual inputs: (a) temperature, and (b) superstrate thickness..... 51

Figure 4.14. The measured effect of ash accumulation on the resonant frequencies of the microstrip patch antenna sensor at 23°C: (a) S_{11} curves of the f_{10} frequency with different thicknesses of ash; (b) shifts of the antenna resonant frequencies with increase in ash thickness. 52

Figure 4.15. The measured effects of ash accumulation and temperature changes on the (a) f_{10} and (b) f_{01} frequencies of the antenna sensor. 53

Figure 4.16. A comparison between ash thickness and temperature inversely determined from the antenna sensor frequencies and actual inputs: (a) temperature, and (b) ash thickness. 54

Figure 5.1. A block diagram of the wireless temperature sensing system. 57

Figure 5.2. The physical dimensions and feeding structure of the designed microstrip antenna sensor. 60

Figure 5.3. The simulated relationship between the antenna sensor's normalized resonant frequency shift and the temperature. 60

Figure 5.4. The fabricated antenna-senor with the microstrip delay line. 61

Figure 5.5. The time domain signal converted from the measured S_{11} parameter of the fabricated antenna sensor with the delay line. 61

Figure 5.6. UWB Tx/Rx antenna; (a) dimensions of the radiation patch; (b) dimensions of the ground plane; (c) top view of the fabricated antenna; (d) bottom view of the fabricated antenna. 62

Figure 5.7. A comparison between the simulated and measured S_{11} parameter of the UWB Tx/Rx antenna. 64

Figure 5.8. The measured radiation gain of the fabricated UWB Tx/Rx antenna. 65

Figure 5.9. The fabricated wireless temperature sensor node; (a) top view (b) bottom view. 65

Figure 5.10. The experimental setup for characterizing the antenna for high-temperature sensing. 66

Figure 5.11. The wireless sensor node placed at the entrance of the oven. 67

Figure 5.12. The digital signal processing algorithm; (a) flow diagram; (b) signals corresponding to the various processing blocks. 68

Figure 5.13. The time domain backscattered signal converted from the measured S_{21} parameter. 70

Figure 5.14. The spectrogram of the backscattered signal..... 70

Figure 5.15. The spectra of the gated time-domain signals at different temperatures. 71

Figure 5.16. The measured relationship between the antenna sensor's normalized resonant frequency shift and the temperature change. 71

Figure 6.1. An illustration of a microstrip line resonator: (a) a typical ring resonator; (b) the proposed resonator. 74

Figure 6.2. The physical design of the proposed microstrip resonator. 79

Figure 6.3. (a)The proposed microstrip line resonator fabricated on Rogers 3006 printed circuit board (PCB) using print-etching technique; and (b) a comparison between simulated and measured S_{21} curves of the resonator. 80

Figure 6.4. The experimental setup for measuring the temperature dependency of the dielectric constant of PCB on which a microstrip line resonator was fabricated 81

Figure 6.5. The measured relationship between the Rogers 3006 dielectric constant and the temperature change. 82

INTRODUCTION

Today, many structures are in service well beyond their intended lifetime. With the growing concern toward safety and with the stringent societal, environmental, financial, and operational requirements, it is essential to accurately monitor the condition of these structures. For example, the safe and efficient operation of boilers relies on accurate measurements of temperature and ash accumulation [1]. Ash accumulation hinders efficient heat transfer and can lead to damage of boiler turbines, either through corrosive action or the sheer weight of deposits hanging from pendant superheaters. Operational procedures to control ash fouling are site-dependent and should be studied under particular circumstances and constraints [2]. This is because boiler plant design features–furnace size and geometry, spacing of convection tube banks, burner arrangement–impact ash slagging and fouling [3]. In addition, ash fouling depends on the types of minerals that are present in coal [2], [4]. Nevertheless, ash blowing using superheated water, steam, and air is common to all coal-fired boilers [5]. This process is controlled based on an initial assessment of the plant, operating experience, and predetermined sequences often based on numerical models that mimic the behavior of the plant [6], [7]. These models are not accurate due to the complexity of the ash fouling phenomena. Given that this cleaning process (i.e., the ash blowing process) has a variable response depending on fouling mechanisms and can accelerate abrasion of surfaces, it should be kept to a minimum [2], [8]. This limitation has given rise to smart blowing, a process that consists of actively monitoring boiler data such as heat transfer, exit gas temperature, and emissions levels to determine if ash blowing is required [1], [9]–[12].

To avoid excessive slagging or superheater material failure, Zhang *et al.* [9] used acoustic pyrometry technology, which is primarily used in boiler control, to measure flue gas temperature [11]. Acoustic pyrometers send sound waves across the boiler relying on the fact that the speed of sound depends on gas temperature. A drawback to acoustic methods is that the speed of sound depends significantly on the gas composition and can also be affected by ash particles and the refraction of the sound wave front by density and temperature gradients [1]. Based on the review of published literature, it is essential to decouple the effect of temperature and ash to ensure safe and efficient operations of these structural systems. Moreover, due to safety concerns, we need to monitor the strain variation of steam pipes. Thus, for the safe and efficient operation of boilers, we have identified three key measurands–temperature, strain, and ash thickness–that must be extracted from the antenna sensor response. In addition, due to the high-temperature environment, we propose wireless interrogation of the antenna sensor without electronics to circumvent the requirements for wiring inside the high temperature environment.

To achieve our objectives, which are to ensure safe and efficient operation of structural systems by monitoring multiple parameters from the response of a single sensor and by wirelessly interrogating the antenna sensor from a long distance without electronics, first, we introduce the proposed sensing technology (i.e., the patch antenna) in chapter 2. In this chapter, we also cover the design and the analysis of the microstrip patch antenna particularly for sensing purpose. Mathematical expressions are established to help select the substrate material for the antenna sensor based on sensing applications.

In chapter 3, we demonstrate the use of a single antenna sensor for simultaneous strain and temperature sensing. To resolve the problem of cross-sensitivity between temperature and strain, we exploit the two fundamental resonant frequencies of a single antenna sensor with a rectangular

radiation patch. Based on the transmission line model, the normalized antenna resonant frequency shifts were found to be linearly proportional to the strain and temperature change. By selecting the dielectric substrate material with a right thermal response, the theoretical prediction was validated by experimental measurements. Curve-fitting the normalized antenna resonant frequency shifts as linear functions of the strain and temperature change enables inversely determining the strain and temperature changes from the measured antenna resonant frequency shifts.

In chapter 4, we demonstrate simultaneous measurement of temperature and superstrate thickness (i.e., ash) using a single microstrip patch antenna. To decouple the effect of temperature variations and superstrate accumulation on the antenna sensor, we exploit the two fundamental resonant frequencies of a single antenna sensor with a rectangular radiation patch. Since the antenna resonant frequencies depend on the radiation patch dimensions and the antenna effective dielectric constant, which is a contribution of the dielectric constants of all layers (i.e., substrate and superstrate) and their respective thicknesses, it is possible to extract temperature and superstrate thickness from the response of the antenna sensor.

In chapter 5, far-field interrogation of an antenna sensor without electronics is demonstrated for high-temperature sensing applications. The sensor node consists of a microstrip patch antenna serving as the temperature sensing unit and an UWB Tx/Rx antenna with a Reactive Impedance Surface (RIS) ground plane. The entire sensor node was implemented on Rogers 3210 commercial PCB using simple fabrication techniques such as chemical etching. The temperature information is encoded in the signals backscattered by the sensor node, and a time domain gating technique is developed to extract the resonant frequency of the antenna sensor from the backscattered signal.

In chapter 6, due to the variability that exists in the fabricated PCBs, and since the broad range of microwave applications requires detailed knowledge of the dielectric properties of materials, we investigate the use of a microstrip line resonator for dielectric property measurement of PCB. By comparing the extracted material properties (i.e., the dielectric constant and dissipation factor) to values specified by the manufacturer of the PCB, we conclude that the configuration of the proposed microstrip line resonator is suitable for measuring the dielectric properties of PCB.

The final chapter of this dissertation (chapter 7) highlights the main findings of the project and presents the scientific impacts of the research. The findings presented in this dissertation will help coal power plants progressively evolve to meet the growing demand for safe and efficient power generation. Moreover, this will reduce the downtime usually associated with routine maintenance and will reduce the high maintenance cost of current technologies utilizing thermocouple as temperature sensors.

CHAPTER 1: BACKGROUND

1.1 Introduction to structural health monitoring

Structural Health Monitoring (SHM) is a vital technology that implements real-time condition monitoring or damage detection mechanisms to assure the safety of structural systems such as aircraft, power stations, bridges, dams, buildings, large machinery, and more. [13]. This process involves monitoring the system using in-situ sensors. The acquired measurements enable analysis that determine the current health state of the system [14]–[16]. Worden and Dulieu-Barton, and Fu-Kuo Chang have presented a more comprehensive description of SHM [16], [17]. The motivation for SHM technology development comes from the potential life-saving and economic impact of this technology [15]. Nearly all private and government industries want to detect damage at the earliest possible time not only in the products they manufacture but also in their manufacturing facilities. These industries do implement some form of SHM. For example, the semiconductor manufacturing industry is implementing SHM to decrease the need for redundant equipment necessary to prevent inadvertent downtime at their manufacturing facilities as downtime costs millions of dollars [18]. Aerospace companies in the United States along with some government agencies are currently exploring SHM technology for damage identification in the space shuttle control surfaces hidden by heat shields [15]. This damage identification technology has significant safety implications. As a result of economic issues, many structures in civil, mechanical and aerospace engineering are used beyond their initial design life despite aging and the associated damage accumulation. Moreover, with the complexity of today's structures that need to address more stringent societal, financial, environmental, and operational requirements, it is essential to monitor the health of structures for safe and efficient operation.

The safety and economic benefits that the SHM technology offers can only be realized if the condition monitoring system offers sufficient warning such that corrective actions can be taken to prevent failure of the structure. For SHM applications, there exist several types of sensors; almost all of them convert physical properties into electric signals [19]–[22]. In general, sensors can be classified as wired or wireless. Some commonly used wired sensors are thermocouples [23]–[25], strain gauges [26]–[29], and optical fiber sensors [30]–[34]. These sensors have an inherent drawback as they can only be interrogated via a wired connection, which limits the mobility of dynamic systems. Moreover, wired sensors usually incur high maintenance costs especially for high-temperature applications [35]–[37]. Wireless sensing allows us to circumvent the problems inherent to wired sensors [38], [39]. A typical wireless sensor comprises of two parts: a wireless sensor whose primary objective is to encode the measurand of interest into a Radio Frequency (RF) signal, and a wireless reader whose primary objective is to decode the received RF signal and extract the necessary information [40]. Wireless sensors can be classified as either active or passive. This is solely based on whether the sensor requires an onboard battery as a power source. A review of wireless sensors is presented below.

1.2 A review of wireless sensors

1.2.1 Active wireless sensors

Active wireless sensors are sensors that require an onboard battery to power the sensor node circuitry. Active wireless sensors usually have a circuitry consisting of a microcontroller chip that is used for sensing signal processing and wireless transmission [41]–[43]. Most active wireless sensors are designed based on the Berkeley-Mote platform [44]–[46] because of the availability of tiny driven operating systems, which provide support for efficiency, modularity, and concurrency-

intensive operation [47]. This operating system, called TinyOS, fits in 178 bytes of memory. TinyOS has an open architecture capable of scaling with current technological trends, supporting smaller, more tightly integrated designs, as well as implementing software components into hardware [45]. Although the user can design and fabricate a custom sensor board based on application needs, these sensors are not suitable for high-temperature SHM applications because of the onboard battery and electronic components. Moreover, recharging or replacing the onboard battery presents a significant maintenance challenge [48]. As such, the maximum operating temperature and life of the sensor are limited by the specifications of the battery on board.

1.2.2 Passive wireless sensors

In contrast to active wireless sensing, passive wireless sensing is becoming increasingly popular as it eliminates the high maintenance cost typically associated with onboard batteries [49]. Passive wireless sensors consume little to no power. If power is needed, the power consumption is so low that it can be harvested from other energy sources [50], [51]. These types of sensors can be grouped into two main categories depending on whether electronics components are present at the sensor node. Popular passive sensors with electronics at the sensor node are those that utilize Radio Frequency Identification (RFID) technology. Non-electronics passive sensors comprise inductive sensors, Surface Acoustic Wave (SAW) sensors, and antenna sensors.

1.2.2.1 Wireless RFID enabled sensors

A typical RFID system consists of an interrogator (also known as reader) and a transponder (or tag). Depending on applications, tags can be divided into three groups: active, semi-passive, and passive. An active tag has both an internal power source and a tag transmitter. The semi-passive tag has a power source, but there is no transmitter. Semi-passive tags use backscattering to transmit data to the reader [40], [52]–[54]. Since semi-passive and active do have a power supply

on board, they fall into the category of active sensors and are not covered in this section. In contrast to semi-passive and active tags, passive tags are the least complex and cheapest as they have no internal power supply since energy is harvested from the electromagnetic (EM) field transmitted by the reader [52]. When the tag is in the range of the reader, it receives an EM signal through its antenna. Energy from the signal is then stored in an onboard capacitor. This energy is used to power the internal RFID tag's circuitry, which transmits a modulated signal to the reader through one of two methods: load modulation (typically for frequencies below 100 MHz), and backscatter (for frequencies higher than 100 MHz) [52], [54]. Load modulation consists of releasing energy from the capacitor to the tag coils in variable strengths over time. Any variation of the current in the tag's coil causes a small current variation in the reader's coil due to the mutual inductance between the two, and the variation is detected by the reader [52]. This method is commonly utilized for near-field coupling. On the other hand, the backscatter coupling is a process in which the tag's circuit changes the resistance of the tag's antenna. Part of the energy incident on a tag's antenna is reflected due to impedance mismatch between the antenna and the load circuit. Changing the mismatch or loading on the antenna can vary the amount of reflected energy. These changes in resistance will be picked up and demodulated by reader [52], [54], [55]. This approach is commonly used for far-field coupling.

Passive RFID sensors are widely used in transportation, personnel access control, animal tracking (or livestock ID), electronic transport/toll-collection (such as E-ZPass), SHM applications, and many more [52], [54]. This is due to their long-distance detection capability, and in some applications for their low-cost implementation [55]. In general, passive RFID sensors can be divided into chip-based or chipless RFID sensors. The fundamental difference between chip-based and chipless RFID tags is the presence or absence of an onboard silicon chip or integrated

circuit (IC) chip [56]. In recent years, chip-based RFID sensors have been proposed for temperature sensing [57]–[62] and for strain sensing [63]–[68]. Bhattacharyya *et al.* measured the changes in temperature by monitoring the power backscattered by the tag [58]. Sample e*t al.* developed a Wireless Identification and Sensing Platform (WISP) to enable an RFID tag to interrogate different sensors to sense temperature, voltage levels, light, and more. [59]. Occhiuzzi *et al.* employed a meandering line antenna in an RFID tag for strain measurement [69]. The dimensions of the antenna change with the applied strain, which in turn causes a change in the power backscattered by the tag. Therefore, it was possible to measure strain from the backscattered power. Merilampi *et al.* proposed a printed RFID antenna to measure strain from changes in the power of the backscattered signal [68]. One of the limitations of an RFID-based wireless sensor is that the size of the RFID tags is quite large because of their low operation frequency. Yi *et al.* proposed an antenna folding technique using vias to reduce the dimension of the RFID antenna; the performance of the proposed sensor was validated by tensile testing, and the strain was extracted from the measured resonant frequency of the antenna [63]. Further reduction in the size of the RFID antenna was achieved by adding slots to the radiation patch [66]. The slots increase the current path and thus lower the frequency of the antenna. Since the RFID sensor can only measure strain along one direction, Li *et al.* proposed a rosette configuration made of three antenna sensors for measuring multi-axial strain fields [67]. Despite these advances, the major drawbacks of RFID sensors, like the large antenna sizes and the slow interrogation speed, remain. Moreover, RFID sensors can measure either temperature or strain but not both parameters because they are interrogated at a single frequency.

Chipless RFID tags eliminate the IC chip by either using the length of the delay line or multiple resonators for tag identification [70], [71]. Girbau *et al.* realized passive temperature

sensing based on time-coded chipless RFID tags. The sensor comprised of a UWB antenna connected to a delay line loaded with a resistive temperature sensor [71]. Preradovic *et al.* presented a chipless RFID sensor with an integrated thermistor for temperature sensing [70]. In both cases, variations in temperature will cause a change in the resistance of the sensor. The resulting impedance mismatch between the tag antenna and the sensor, in turn, changes the backscattered power. Since a sensor element must be implemented in these chipless RFID tags, they cannot sense more than one parameter. To circumvent these challenges, Karmakar proposed the use of smart materials rather than external resistors [56]. The proposed sensor employs two spatially separated electric-inductive-capacitive resonators to sense multiple parameters. To differentiate different sensing parameters, the resonators were coated with smart materials tailored to measure a specific parameter; one resonator was coated with polyvinyl alcohol for relative humidity sensing while the other resonator was coated with 0.2 mm thick phenanthrene for temperature detection. However, the problem of cross-sensitivity between these two parameters was not addressed in their work. Moreover, coating the resonators with smart materials increases the thickness and cost of the sensor tag.

1.2.2.2 Wireless surface acoustic wave sensors

Surface acoustic wave (SAW) sensors are a class of microelectromechanical systems (MEMSs) that rely on the modulation of surface acoustic waves to sense a physical phenomenon. In general, a wireless SAW system comprises an EM transducer and a SAW sensor node [72]–[75]. The transducer transmits the interrogation signal (EM wave) to the sensor node and processes the reflected EM wave. The sensor comprises a piezoelectric substrate that is connected to a passive antenna. In addition, there are reflectors on the piezoelectric substrate a short distance from the antenna connection. When an incoming EM signal is transmitted by the

transducer, it is first received by the antenna. This signal is then sent to the piezoelectric substrate to generate SAWs. Once generated, the SAWs propagate along the substrate and are reflected back to the antenna upon reaching the reflector. The waves will be trapped or modified while propagating, and variation of substrate physical properties will be encoded in the reflected waves. The SAWs will be converted back into an EM signal and retransmitted to the transducer, therefore, allowing the measurand of interest to be decrypted in the transducer.

Reindl *et al.* demonstrated wireless temperature sensing using a SAW sensor [76]. The authors were able to measure temperature because of the temperature effect on the propagation speed of the SAW. Although the proposed sensor was demonstrated to work up to 200^{o}C, passive wireless SAW sensors are not suitable for high-temperature harsh environments [77], [78]. Wireless strain sensing has also been demonstrated using SAW sensors [79], [80]. SAW sensors have been developed for other applications: automotive applications (torque and tire pressure sensors) [74], medical applications (chemical sensors) [81]–[83], and industrial and commercial applications (vapor, humidity, and mass sensors) [73], [84]–[86].

SAW sensors are competitively priced, sensitive, and intrinsically reliable [87]. Like many technologies, SAW sensors have some drawbacks. Not all substrate materials can be used to fabricate the sensors. The most commonly used substrates are quartz (SiO_2), lithium tantalate ($LiTaO_3$), and lithium niobate ($LiNbO_3$) [83]. Each substrate presents specific advantages and disadvantages, which include cost, temperature dependence, attenuation, and propagation velocity [72], [88]. Moreover, SAW sensors operate at low frequencies (typically 25-500 MHz) to keep the propagation loss low [87], [89]. These frequency limitations make the miniaturization of such sensors very difficult; it is a limiting factor for specific applications, particularly those with sensor weight restrictions.

1.2.2.3 Wireless inductively coupled sensors

Like most wireless sensing systems, an inductively coupled sensing system consists of a wireless reader or interrogator and a wireless resonance sensor. The sensor node is essentially a resistor, inductor, and capacitor circuit whose frequency can be detected via inductive coupling between the sensor and reader coils [90], [91]. Depending on the applications, the measurand of interest will affect the capacitance, inductance, or resistance of the sensor circuit. For example, Loh *et al.* proposed localized strain and corrosion detection using thin film wireless strain and a pH sensor that utilized inductive coupling technology [92]. The authors purposely designed the thin film to change electrical properties with applied strain and variation in pH stimulus. Wireless communication was achieved using traditional magnetic coil antennas. With applied strain, the inductance of the sensor changed, causing a change in the resonant frequency. The strain was inversely determined from the measured resonant frequencies. Zhang *et al* [93] utilized this technology to demonstrate pressure sensing. They presented a readout system for wireless pressure sensing, which comprises a pressure-sensitive capacitor and an inductance coil to form an LC circuit. Pressure variations caused the LC resonant frequency to shift. This technology was also utilized for other applications: pressure garment applications [94] and medical, biomedical, and chemical sensing applications [95]–[97].

Despite the simple configuration and relatively small size of inductively coupled sensors, they are not suitable for SHM applications due to the short interrogation distance, which is usually limited to a few centimeters since the sensor and the reader must be nearby. Moreover, for SHM applications, an array of sensors is usually required–sensors can be placed at locations that are inaccessible during operation of the structures (e.g., boilers). Consequently, these sensors are not suitable due to the short interrogation distance.

1.2.2.4 Wireless antenna sensors

Wireless sensing using antenna sensors is becoming increasingly popular as it eliminates the high maintenance cost usually associated with cable connections, especially for high-temperature applications [43], [49]. Antenna sensors have been studied not only for wireless communication but for SHM. They are especially attractive due to their compact size, light weight, ease of manufacturing, and low fabrication cost [98]. Moreover, if the antennas are fabricated on flexible substrates, they can readily conform to nonplanar surfaces [99]. Since the resonant frequency of an antenna sensor depends on its physical dimensions and the dielectric properties of the substrate, any change in these parameters will shift the resonant frequency of the antenna. Consequently, one can use them as sensing elements by changing the antenna dimensions and/or the dielectric properties.

In the past, patch antennas have been used for the single modality sensing of temperature, strain, cracks, and pressure [100]–[113]. Tata *et al.* demonstrated the use of antenna sensors for strain measurement [107]. The fabricated antenna sensor was bonded on a cantilever beam, and the load was applied at the beam tip to generate mechanical strain in the beam. Since the resonant frequency of an antenna depends on the physical dimension of the radiation patch, mechanical strain applied to the antenna caused changes in the antenna dimensions and, consequently, a shift in the antenna resonant frequency. Therefore, the applied strain was inversely determined from the antenna resonant frequency after a correlation was established between the input values (applied strain) and the output values (measured antenna resonant frequencies). The strain sensitivity of the antenna sensor obtained by experiments agreed with the analytical prediction developed by the authors. Although successfully demonstrated for strain sensing applications, temperature variations have a major influence on the measurement accuracy of an antenna sensor [114]. As a

temperature compensation techniques, Maurya *et al.* suggested an increase in substrate height of the antenna sensor [100], [101]. However, increasing the substrate height results in a larger antenna – an approach not desirable for many applications due to the increase in cost and weight of the antenna sensor. Given these limitations, Sanders *et al.* evaluated the effect of temperature on the antenna resonant to adopt the patch antenna as a temperature sensor [106]. The authors obtained excellent linearity between the measured resonant frequency shifts and temperature changes. Temperature extracted from these measured frequencies agreed with the thermocouple measurements.

Antenna sensors have also been studied for crack detection and crack orientation in structures [102], [112], [113]. Mohammad *et al.* [112] and Xu *et al.* [113] showed that the presence of a crack in the ground plane of the antenna sensor increases the electrical length of the antenna. These changes in electrical lengths result in shifts of the resonant frequencies. Compared to other sensors, and based on previous studies, it is evident that antenna sensors are a viable solution for SHM applications as they eliminate the high maintenance cost usually associated with cable connections, especially for high-temperature applications [43], [49]. Since the antenna sensor resonates at various frequencies depending on the current direction, by measuring the shifts in resonant frequencies, changes in physical properties of the structures and environmental conditions (e.g., temperature, superstrate accumulation) can be measured.

1.3 A review of the wireless interrogation mechanisms of antenna sensors

Like many wireless systems, the wireless interrogation mechanism of antenna sensors consists of two parts: the wireless interrogator and the wireless antenna sensor package. This interrogation mechanism is based on antenna backscattering. When an interrogation signal is

transmitted to the antenna sensor, the signal will be received by the antenna sensor, which will then encode the sensing information and reflect the received signal to the interrogator. This reflected signal is referred to as the antenna backscattering [43], [106]. The signal received by the wireless interrogator usually consists of both the background clutter (structural mode) and the antenna sensor backscattered signal. A significant challenge of passive wireless interrogation of antenna sensors is the problem of "self-jamming," when the antenna backscattered signal is jammed by the background clutter [43]. Many techniques have been developed to tackle this challenge, notably the time gating approach [71], [105], [115]–[118]. This approach relies on delaying the sensor signal using a high-quality-factor resonator or a delay line. Time gating can then be applied to separate the sensing signal from the background clutter [117]. Due to the time domain processing, Fast Fourier Transformation (FFT) must be applied to the time-gated signal to extract the frequency information of the sensing signal. The FFT operation, however, usually has a low-frequency resolution that severely limits the measurement resolution [119]. The FFT operation was replaced by frequency-stepping technique to achieve higher frequency resolution, but the interrogation speed was compromised [118]. To address the self-jamming setback, Xu and Huang introduced the technique of modulating the antenna backscattered signal at the sensor node to separate it from the backscattered clutter [120]. The amplitude modulation was achieved by implementing a microwatt impedance switching circuit at the sensor node. To achieve completely passive operations, the circuit was powered by a photocell. To demodulate the received signal at the wireless interrogator end, the authors used a down-conversion mixer. The resonant frequency of the antenna sensor was obtained from the signal spectrum by stepping the interrogation frequency. By doing this, the authors successfully achieved higher frequency resolution than the time gating technique.

Near-field wireless interrogation of the antenna sensor was demonstrated up to 1050°C by Cheng *et al.* [105]. The patch antenna was simultaneously considered a temperature sensor and an integrated antenna. Therefore, the patch antenna was directly interrogated at a short distance without the use of electronics. Time gating was applied to determine the antenna resonant frequency of the antenna–this allows for the environmental temperature of the antenna sensor to be indirectly determined since a change in temperature causes a shift in the resonant frequency. Although this interrogation technique was successfully demonstrated, wireless interrogation using this mechanism is limited to just a few centimeters because of the relative low-quality factor of the antenna sensor [121].

1.4 A review of the superstrate effect on the antenna performance

Like many technologies, antenna sensors are used for long durations; and during their years in service, environmental conditions (ash, water, ice, snow, etc.) cause variations in the sensor performance due to superstrate build-up on the radiation patch [122]. The study of the effect of a dielectric layer on the antenna sensor performance dates back to as early as 1980 [123]–[128]. From a design aspect, Bahl showed that a superstrate layer above the radiation patch drastically affects the antenna characteristics [123]. This is because the antenna frequency is a function of the antenna effective dielectric constant, which also depends on the substrate and superstrate dielectric constants and their respective thicknesses [98], [122]. Hammas reported a decrease in the antenna sensor frequency with an increase in superstrate thickness [128]. Meanwhile, Alexópoulos and Jackson reported that a superstrate-loaded antenna might be desirable to maximize antenna gain and radiation efficiency [126]. They established criteria for choosing suitable dielectric materials and dimensions for which surface waves are eliminated and radiation efficiency is maximized.

This study is particularly important since a high gain of the antenna sensor is desired for wireless communication [105], [129]. For sensing purposes, Stolarczyk *et al.* [130] proposed an ice detection system comprising of a network of thin, flexible microstrip antennas placed at critical locations on an aircraft wing. The system also includes a thermocouple for temperature measurement and a set of acoustic sensors to measure physical properties (density and viscosity) of the superstrate. This combination of sensors helps measure mixtures that accumulate over the antenna. A computer processes the measured data to discern the presence and thickness of ice, water frost, ethylene-glycol, or slush. A major drawback of such a system is that cable connections (i.e., thermocouples used for temperature measurements) could incur high installation and maintenance costs, especially for high-temperature sensing applications.

Thus far, coating the antenna sensor to reduce or eliminate the effect of environmental conditions or hazard has been the conventional approach [131]–[133]. However, this approach presents some technical and practical challenges. From a practical standpoint, the commercial viability of a sensor depends on its size and cost. In this former respect, coating the antenna sensor increases its thickness and results in a bulkier sensor, which is undesirable for many applications. From a technical standpoint, the effect of temperature on the dielectric layers (i.e., substrate and superstrate) must be accurately accounted for. Temperature changes the dielectric constant and, hence, the effective dielectric constant of the antenna sensor, which results in a shift of the antenna frequency. Although coating the antenna sensor may be suitable in some cases (e.g., protecting the antenna from ultraviolet radiations), it is undesirable for boiler condition monitoring as their safe and efficient operation relies on accurate measurements of the environmental temperature and ash build-up on surfaces [2], [8], [134]. Since our objective is to ensure safe and efficient operations of boilers, decoupling these environmental conditions from the antenna sensor output is necessary.

Based on published literature, operational procedures to fight against ash fouling are site-dependent and should be studied under the particular circumstances and constraints of the site [2]. This is because boiler plant design features–the size and geometry of the furnace, the spacing of convection tube banks, the burner arrangement, and many more–impact slagging and fouling [3], and ash build-up depends strongly on the types of minerals present in coal [2]. Nevertheless, ash blowing using superheated water, steam, and air is common to all coal-fired boilers [5]. This process is adjusted based on an initial assessment of the plant and experience. Moreover, it relies on predetermined sequences based on numerical models that mimic the behavior of the plant–an inaccurate model due to the complexity of the ash fouling phenomena. Given that this cleaning process varies depending on fouling mechanisms and can accelerate abrasion of boiler surfaces, it should be kept to a minimum [2], [8]. This request has given rise to smart blowing, a process that consists of actively monitoring boiler data such as heat transfer, exit gas temperature, and emissions levels to determine if and where ash blowing is required [1], [9], [10], [12]. Detailed mechanisms are not discussed here; the reader should refer to the work of the cited authors. For safe and efficient operations of structural systems, it is essential to decouple the effect of temperature and superstrate build-up on the antenna sensor output.

1.5 A review of the dielectric permittivity measurement of PCBs

A dielectric permittivity is a complex number, and its measurement is important for practical applications as well as research. The real part of the dielectric permittivity, also called the dielectric constant, is a quantity that measures the ability of a material to be polarized in the presence of an external electric field. The imaginary part of the dielectric permittivity, also known as the dissipation factor, is a quantity that determines the loss rate of energy from a material or a

substance due to the existence of an electric field. Measuring the dielectric permittivity is very important, and the benefits depend on applications. For example, in agriculture, these measurements are useful for applications such as the drying process of grains, the treatment of seed to boost the germination process, and the control of insects in stored grain [135]. In RF applications, measurement of the dielectric permittivity of PCB is important for ensuring the quality and the reliability of electronic devices.

Several techniques have been established for measuring the dielectric permittivity, and a comprehensive review is presented by Venkatesh [136]. Some of the methods developed are the transmission/reflection line technique, free space technique, open-ended coaxial probe technique, and resonant technique. In general, factors such as frequency range, required accuracy of measurement, material properties, material form, sample size, convenience, and cost play an important role in selecting an adequate measurement technique. Among all these methods, measurements using microstrip resonators have gained increased popularity since the method was first proposed by Troughton [137]. It is undoubtedly because of the simplicity of the structure, the ease of fabrication, the accuracy of the measurement technique, the wide frequency band provided by a single microstrip resonator, and the negligible radiation losses due to the absence of the end-effects [138]. Since Troughton's work, various researchers have used microstrip ring resonators (MRR) for the dielectric permittivity measurement of substrate materials. Sofin *et al.* [139] and Rashidian *et al.* [140] measured the dielectric permittivity of materials under tests (MUT) by using a single MRR fabricated on substrate materials with a known dielectric constant. The MUT was overlaid on the MRR, and the dielectric constant was extracted from the shift in the frequency response of the MRR. Although the technique allows for the use of a single MRR to measure the dielectric constant of multiple MUT, the appropriate location of the overlaid MUT and the air gaps

between the overlaid MUT and the MRR play a vital role in the accuracy of the measurements. Heinola characterized the dielectric permittivity of PCB by fabricating the MRR structure directly on the material to be evaluated [141]. The disadvantages of these MRR are the local radial distortion of the field near the coupling gaps, the curvature effect, and field interactions across the ring [142].

Since the MRR is a microstrip line that forms a loop, as part of this research, we will investigate various shapes (e.g., square, rectangle) of the MRR with bend compensation techniques [143] to reduce radial distortion of the field near the coupling gaps, reduce or eliminating the curvature effect, and ultimately improve the accuracy of measurements.

2. Research objectives and impacts

The goal of this research is to study the sensor design, multivariant analysis, and wireless interrogation of flexible antenna sensors to realize distributed condition monitoring of coal-fired boilers at low cost. Monitoring the operational condition of the coal-fired boiler is an important task that could bring tremendous benefits, including in-situ process control, real-time health assessment of structural components, improved heat exchange efficiency, and reduced downtime associated with maintenance. Moreover, this will provide large- scale in-situ measurement data that will enable the development and refinement of simulation models. Unfortunately, low-cost distributed sensing is challenging due to the high-temperature, high-pressure, and corrosive environment. To solve the limitations of existing sensing technologies, this research will focus on: (a) establishing a procedure for characterizing the dielectric properties of flexible substrates, (b) extracting multiple measurands from the response of a single antenna sensor, and (c) demonstrating wireless interrogation of passive antenna sensors without electronics.

CHAPTER 2: ANALYSIS OF PATCH ANTENNAS FOR SENSING APPLICATIONS

Microstrip antennas have received substantial attention since the 1970s, although the notion of a microstrip antenna can be traced to 1953 and a patent in 1955 [98]. A microstrip antenna, as illustrated in Figure 2.1, consists of a radiation patch, a ground plane, and a dielectric layer. The radiating patch may have different shapes: rectangular, square, thin strip (dipole), circular, elliptical, triangular, or any other configuration. The most commonly used configurations are square, rectangular, and circular because of the ease of analysis, fabrication, and their attractive radiation characteristics [98], [144].

Several models have been developed to analyze the microstrip patch antenna. The most prevalent models are the transmission line, cavity, and full wave (which includes primarily integral equations/Moment Method) [145]–[147]. Given that the transmission line model is the easiest of all and provides good physical insight [98], it will be used for the analysis of a rectangular patch

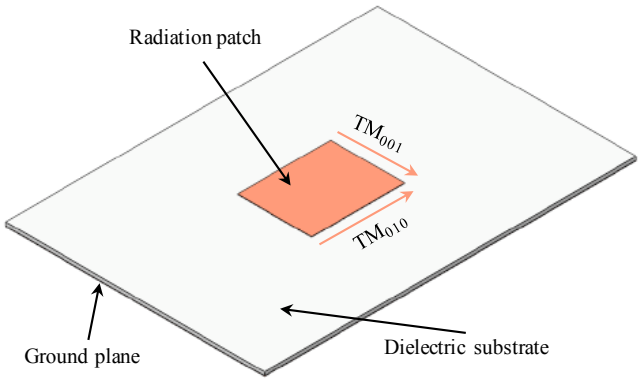

Figure 2.1. Configuration of a rectangular patch antenna. The radiation patch and the ground plane are made of conductive materials.

antenna (RPA) for temperature and strain sensing. An RPA possesses two fundamental resonant modes; the TM_{010} mode with current flowing along the length direction and the TM_{001} mode with current flowing along the width direction of the radiation patch. Per the transmission line model, the resonant frequency of the TM_{010} mode, i.e., the f_{10} frequency, can be calculated as

$$f_{10} = \frac{c}{2(L + 2\Delta L)\sqrt{\varepsilon_{re}}}, \tag{2.1}$$

where c, L, and ε_{re} represent the speed of light, the length of the radiation patch, and the effective dielectric constant, respectively [98]. The effective dielectric constant of the antenna ε_{re}, when no superstrate is present, depending on the substrate height h, the width of the radiation patch W, and the dielectric constant of the substrate ε_r, can be expressed as

$$\varepsilon_{re} = \frac{\varepsilon_r + 1}{2} + \frac{\varepsilon_r - 1}{2\sqrt{1 + 10h/W}}. \tag{2.2}$$

Because of the finite dimensions of the RPA along the length and width, the radiation fields extend beyond the edges of the radiation patch, forming fringing. As such, the length of the antenna is increased by ΔL, which is a function of ε_{re}, W and h, that is

$$\Delta L = 0.412h \frac{(\varepsilon_{re} + 0.3)(W/h + 0.264)}{(\varepsilon_{re} - 0.258)(W/h + 0.813)}. \tag{2.3}$$

If the height of the substrate is much smaller than the radiation patch dimensions (i.e., $h \ll W$ and $h \ll L$), the effective dielectric constant can be approximated as the dielectric constant of the substrate (i.e., $\varepsilon_{re} \approx \varepsilon_r$). In addition, the line extension ΔL can be neglected. In this case, equation (2.1) can be reduced to

$$f_{10} = \frac{c}{2L\sqrt{\varepsilon_r}}. \tag{2.4}$$

The shift of the antenna frequency δf_{10} can be expressed in terms of variations in the patch length L and the substrate dielectric constant ε_r as

$$\delta f_{10} = \frac{\partial f_{10}}{\partial \varepsilon_r}\delta\varepsilon_r + \frac{\partial f_{10}}{\partial L}\delta L \cdot \tag{2.5}$$

$\partial f_{10}/\partial \varepsilon_r$ and $\partial f_{10}/\partial L$ can be derived from equation (2.4) as

$$\frac{\partial f_{10}}{\partial \varepsilon_r} = -\frac{1}{2\varepsilon_r}\frac{c}{2L\sqrt{\varepsilon_r}} = -\frac{1}{2\varepsilon_r} f_{10} \tag{2.6a}$$

and

$$\frac{\partial f_{10}}{\partial L} = -\frac{1}{L}\frac{c}{2L\sqrt{\varepsilon_r}} = -\frac{1}{L} f_{10} \tag{2.6b}$$

The normalized frequency shift $\delta f_{10}/f_{10}$ can then be written as

$$\frac{\delta f_{10}}{f_{10}} = -\frac{1}{2}\frac{\delta\varepsilon_r}{\varepsilon_r} - \frac{\delta L}{L} \tag{2.7}$$

The first term in the right-hand side of equation (2.7) represents the normalized dielectric constant change. For sensing purposes, it is important to select a substrate with a normalized dielectric constant change that varies linearly with temperature, that is

$$\frac{\delta\varepsilon_r}{\varepsilon_r} = \alpha_{\varepsilon_r L}\delta T, \tag{2.8}$$

where $\alpha_{\varepsilon_r L}$ is the thermal coefficient of dielectric constant (TCD_k) of the substrate along the length direction [145]. The second term in the right-hand side of equation (2.7) can be expanded into two parts: the contribution due to temperature change and the contribution due to applied mechanical strain, that is

$$\frac{\delta L}{L} = \frac{\delta L_T}{L} + \frac{\delta L_\varepsilon}{L}, \tag{2.9}$$

in which $\delta L_\varepsilon/L = \varepsilon_L$ is the applied mechanical strain along the patch antenna length. Representing the coefficient of thermal expansion (CTE) of the radiation patch along the length direction as α_{TL}, we can express $\delta L_T/L$ as

$$\frac{\delta L_T}{L} = \alpha_{TL}\delta T \cdot \tag{2.10}$$

Substituting equations (2.8), (2.9) and (2.10) in (2.7) gives

$$\frac{\delta f_{10}}{f_{10}} = -\left(\frac{1}{2}\alpha_{\varepsilon_r L} + \alpha_{TL}\right)\delta T - \varepsilon_L \cdot \tag{2.11}$$

The normalized frequency shift δf_{01} of the TM01 mode can be derived following the same process. Assuming the sensor is under uniaxial loading condition and has a Poisson's ratio v, the normalized frequency shift $\delta f_{01}/f_{01}$ can be expressed as

$$\frac{\delta f_{01}}{f_{01}} = -\left(\frac{1}{2}\alpha_{\varepsilon_r W} + \alpha_{TW}\right)\delta T + v\varepsilon_L, \tag{2.12}$$

in which $\alpha_{\varepsilon_r W}$ and α_{TW} are the TCD_k and the CTE of the substrate along the width direction, respectively. A general form of equations (2.11) and (2.12) can be written as

$$\frac{\delta f_{10}}{f_{10}} = -K_{TL}\delta T - K_{\varepsilon L}\varepsilon_L \tag{2.13a}$$

and

$$\frac{\delta f_{01}}{f_{01}} = -K_{TW}\delta T + K_{\varepsilon W}\varepsilon_L, \tag{2.13b}$$

in which $K_{\varepsilon L}$ and $K_{\varepsilon W}$ represent the strain sensitivities along the patch length and width respectively while K_{TL} and K_{TW} represent the temperature sensitivities along the patch length and width, respectively.

CHAPTER 3: MICROSTRIP PATCH ANTENNA FOR SIMULTANEOUS STRAIN AND TEMPERATURE SENSING

3.1 Introduction

In Chapter 2, we derive an analytical model that demonstrates temperature and strain both influence the resonant frequencies of the patch antenna as the antenna dimensions and the dielectric constant is subject to change with applied temperature and/or strain. Among all the work previously mentioned, the patch antennas have only been used for single modality sensing of either temperature or strain. Ignoring the problem of cross-sensitivity between temperature and strain is voluntarily accepting measurement errors that can lead to catastrophes depending on applications. For boiler applications, since the pressure in the steam pipes can lead to pipe rupture, it is essential to accurately monitor the strain experienced by these structures. One easy way to solve this problem is to add a second or reference sensor. However, such an approach is unattractive for SHM applications as it generally increases the cost, size, and weight of the sensor. An elegant approach to circumvent this problem is to take advantage of the fact that the patch antenna is capable of resonating at different frequencies. For temperature and strain sensing, two resonant frequencies of the patch antenna can be used if they have different strain and/or temperature sensitivities [148].

In this chapter, we demonstrate the use of a single microstrip patch antenna for simultaneous strain and temperature sensing. Since the resonant frequencies of the patch antenna depend on the patch dimensions and the dielectric constant of the substrate, any change in these parameters due to temperature and strain will cause a shift in the resonant frequencies of the

antenna sensor. In this study, we take advantage of the two lowest fundamental resonant frequencies of the patch antenna to demonstrate simultaneous temperature and strain sensing.

3.2 Antenna sensor design and fabrication

3.2.1 Substrate selection and antenna design

The equations derived above provide the theoretical foundation for selecting the substrate material. Since the purpose is to measure strain and temperature simultaneously, it is important that the temperature sensitivities K_{TL} and K_{TW} do not overwhelm the strain sensitivities $K_{\varepsilon L}$ and $K_{\varepsilon W}$ or vice versa. After researching the properties of commercial substrates, we have selected Rogers RT/duroid 5880 as the substrate material for the antenna sensor. Rogers RT/duroid 5880 is a high-frequency Polytetrafluoroethylene composite laminate with reinforced glass microfibers. The randomly oriented microfibers result in dielectric constant uniformity. The dielectric constant ε_r of the selected laminate is 2.2 and the TCD_k is -125 ppm/^{o}C. The CTE values are 31 ppm/^{o}C, 48 ppm/^{o}C, and 237 ppm/^{o}C in x-, y-, and z- directions, respectively. Since the TCD_k is larger than the CTE values, it will contribute predominantly to the temperature sensitivity of the RPA. If this substrate is subjected to thermo-mechanical tests without being bonded on any structures, based on its properties and the theoretical expression derived in (2.13), we predict a K_{TL} value of 31.5 ppm/^{o}C. Since the strain sensitivity K_L is equal to -1, the thermal contribution to the normalized frequency change due to 1^{o}C change is equivalent to that of 31.5 με in strain. By selecting this substrate, applications are limited to temperatures below 350°C, which is the glass transition temperature (Tg) of the substrate [149]. The maximum operating temperature of the sensor is also limited by the operational temperature of the adhesive used in bonding the sensor to the structural

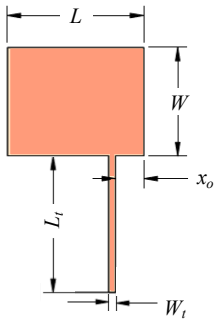

Figure 3.1. The physical design of the antenna sensor edge fed by a microstrip transmission line.

system. The lowest temperature between these two limits determines the maximum operating temperature for the sensor. Therefore, one must select the appropriate adhesive and substrate based on the applications. The substrate thickness was selected to be 0.79 mm. Since we have demonstrated wireless vibration sensing using a substrate with a similar thickness [110], and wireless strain sensing using a substrate of 76 μm [111], we are confident the substrate thickness will not be a limiting factor for the wireless capability of the proposed sensor.

The sensor was designed to operate at the fundamental frequencies of approximately f_{10} of 5 GHz and f_{01} of 6 GHz, which gives a length of 15.9 mm and a width of 19.5 mm for the radiation patch. Since an inset-feed would disturb the current fields of the radiation modes, we selected to feed the radiation patch at the edge using a microstrip transmission line, as illustrated in figure 3.1. As a result, impedance matching of only one resonant mode, that is, the TM_{010} mode, can be realized by adjusting the feeding position x_o. The width of the transmission and thus its impedance was selected taking the fabrication limitation and the feeding location into consideration. We selected the width of the transmission line W_t to be 0.7 mm, leading to an impedance of 100 Ω for the transmission line. In addition, the transmission line also serves as a quarter-wave transformer that matches the impedance of the radiation patch to the 50 Ω SubMiniature version A (SMA)

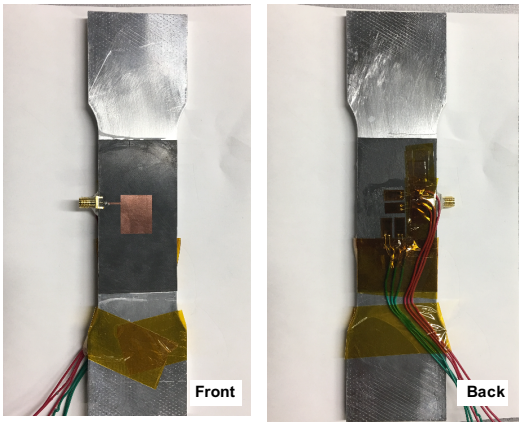

Figure 3.2. A dog-bone sample instrumented with the antenna sensor; (a) front view; (b) back view.

connector. Therefore, its length L_t was calculated to be 11.3 mm at the f_{10} frequency of 5 GHz. Finally, the impedance of the TM_{010} mode was calculated from the impedance of the transmission line and the SMA connector as 200 Ω, based on which the feeding position x_o was chosen to be 3.8 mm [98].

3.2.2 Sensor fabrication

The antenna sensor was fabricated by the print-etching technique. The sensor pattern was first drawn using CAD software and then printed on PCB transfer paper film (Techniks PNPB20). The printed pattern was then transferred from the film to the selected PCB using a clothing iron as the heat source. Subsequently, the PCB was submerged in ferric chloride for chemical etching to remove the exposed copper surfaces. After chemical etching, the PCB was given a final chemical bath in acetone to remove the ink residue.

The antenna sensor was bonded on a dog-bone specimen using LOCTITE superglue. The front and back views of the instrumented specimen are shown in figure 3.2. The dog-bone specimen was made of aluminum 6061-T6 as per ASTM standard E8/E8M - 16a. The dog-bone specimen has a thickness, width, and gauge length of 6.5 mm, 40 mm, and 85 mm, respectively.

The gauge length was chosen as 85 mm to ensure uniaxial loading at the sensor location. To ensure a symmetric configuration of the instrumented specimen, the same substrate used for fabricating the antenna sensor was bonded on the back of the dog-bone specimen. Thin film strain gauges (OMEGA SGD5/350 LY13) were bonded on the substrate on the back to measure strain in both transverse and loading directions, as shown in figure 3.2(b). The pin of the SMA connector was attached to the feed line by soldering. Since the dog-bone specimen also serves as the ground plane to the antenna sensor, the ground of the SMA connector was electrically connected to the dog-bone specimen using conductive epoxy (CircuitWorks CW2400).

To release the specimen from any residual strains due to fabrication, the specimen was subjected to three thermal cycles up to 100^{o}C at a rate of 2^{o}C/minute. Once the maximum temperature was achieved, the sample was allowed to cool naturally to 30^{o}C. After fabrication and annealing, the resonant frequencies of the antenna sensor were determined by measuring the scattering parameters S_{11} using a vector network analyzer (VNA, Rohde & Schwarz ZVA24). Figure 3.3 presents a comparison between the simulated and measured S_{11} parameters of the antenna. The simulated results were obtained using a High Frequency Structure Simulator (HFSS). The fabricated antenna does resonate at 5 GHz and 6 GHz as per the design, and there is an

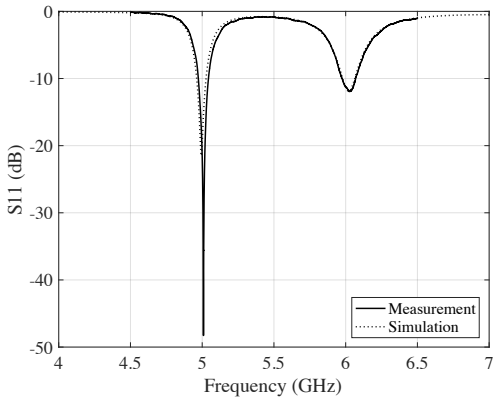

Figure 3.3. A comparison between simulated and measured S_{11} curves of the antenna sensor.

agreement between simulation and measurement. The very slight difference between both S_{11} parameters is most likely due to the fabrication and/or the parasitic capacitance introduced by the SMA connector [107]. The TM01 mode displayed a return loss below -10 dB, even though the impedance of this radiation mode does not match the impedance of the transmission feed line.

3.3 Instrumentation and experimental setup

The experimental setup for characterizing the simultaneous effects of temperature and strain on the antenna sensor's frequency response is presented in figure 3.4(a). A tensile tester (SHIMADZU AG-X plus) equipped with an oven was used to apply the mechanical load and temperature changes on the instrumented specimen. The door of the oven was replaced by a foam box with an opening of 100 mm by 120 mm. When the sample was installed in the tensile tester, the antenna sensor faced the opening so that no reflection was generated by the foam. The foam panel provided thermal insulation of the specimen while avoiding the reflections usually generated by a metallic oven door. Due to the small opening, hot air leaked from the oven to the surrounding environment. Thus, a thermocouple (OMEGA T-type) was placed near the antenna sensor to measure the sensor temperature, as demonstrated in figure 3.4(b). Having a manufacturer specified measurement error of 0.5°C or 0.4% of the measured temperature value (whichever is greater), this thermocouple was selected given its lowest measurement error and cost. To measure the antenna resonant frequency, the antenna sensor was connected to the VNA using a coaxial cable. The VNA was set to sweep 40,000 points between 4.5 GHz and 6.5 GHz, corresponding to a frequency resolution of 50 kHz. By connecting the VNA to a personal computer (PC) through Ethernet, a LabVIEW program running in the PC could be used to acquire and save the S_{11} scattering

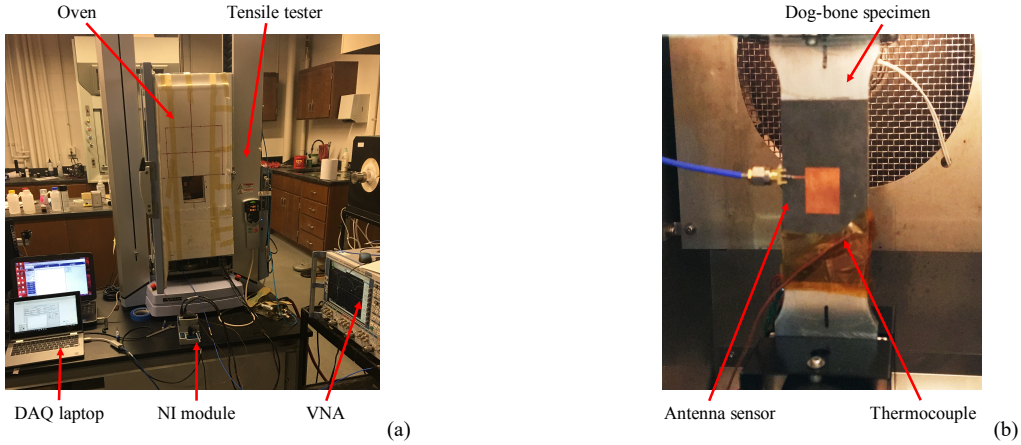

Figure 3.4. (a) The experimental setup for thermo-mechanical testing of the antenna sensor (b) dog-bone specimen with bonded antenna sensor and thermocouple.

parameters measured by the VNA along with the measurement data from a strain gauge module (National Instrument, NI 9237) and a thermocouple module (National Instrument, NI 9211).

The instrumented specimen was loaded in increments of 1000 N at a rate of 20 N/s. Figure 3.5 presents the strain gauges' measurements during the antenna sensor characterization. Although the strain gauges are self-temperature compensated for aluminum, which has a CTE that differs from the antenna substrate, the thermal output from the strain gauges due to the CTE mismatch are not present in the strain measurements. This was achieved by balancing the strain gauge module to zero strain once the desired temperature was achieved and before any load was applied to the specimen. As such, the thermal outputs of the strain gauges were eliminated from the strain gauge' measurements, that is, the strain measurements are contributed by the mechanical load only. As presented in figure 3.5, 1000 N of load generates strains of 55 $\mu\varepsilon$ and -18.4 $\mu\varepsilon$ along the loading and transverse directions. These values agree with the theoretical prediction of 54.5 $\mu\varepsilon$ and -18 $\mu\varepsilon$ along these two directions. Dividing the measured sensitivity in the transverse direction to the loading direction gives 0.335 – a solid agreement with the Poisson's ratio of aluminum 6061-T6

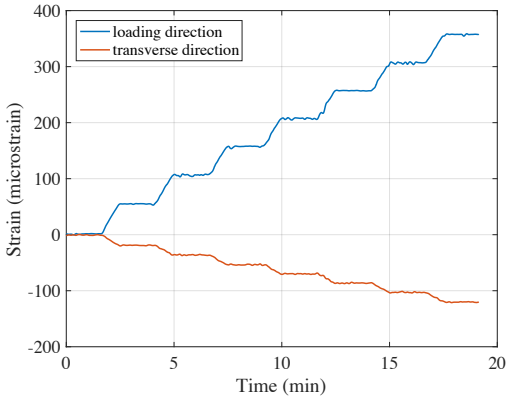

Figure 3.5. Strain measurements along the loading and transverse directions under different loading levels.

and confirmation that the instrumented specimen is under the uniaxial loading condition. As presented in figure 3.5, the specimen was held for a duration of 100 seconds at each load increment. After each load increase, the specimen was first allowed to rest for approximately 43 seconds before any measurements were taken from the antenna sensor. All S_{11} curves, temperature, and strain measurements were time stamped for ease of correlation during data analysis.

3.4 Results and discussion

Before subjecting the antenna sensor to thermo-mechanical tests, the theoretical prediction was first validated by evaluating the sensor's performance due to the applied strain and temperature changes separately. To assess the sensor's performance under strain only, the antenna sensor was subjected to tensile loads along the TM_{010} mode (i.e., along the length of the antenna sensor). With an increase in strain under constant temperature, as derived in (2.11), the S_{11} curves of the TM_{010} mode are expected to shift to the left. This effect is presented in figure 3.6(a) where the f_{10} resonant frequency of the antenna sensor decreases with the applied strain. figure 3.6(b) presents the

normalized resonant frequency shifts of the antenna sensor as a function of applied strain. The measured strain sensitivities were -0.74 ppm/$\mu\varepsilon$ and 0.43 ppm/$\mu\varepsilon$ for the TM_{010} and TM_{001} modes respectively. The data presented in figure 3.6(b) display excellent linearity given the R^2 values of 0.9914 and 0.9844 for the TM_{010} and TM_{001} modes, respectively. The measured strain sensitivities differ slightly from the theoretical prediction, which predicts a 1:1 ratio between the applied strain and the normalized resonant frequency shift. This difference is probably due to the shear lag introduced by the bonding layer [107].

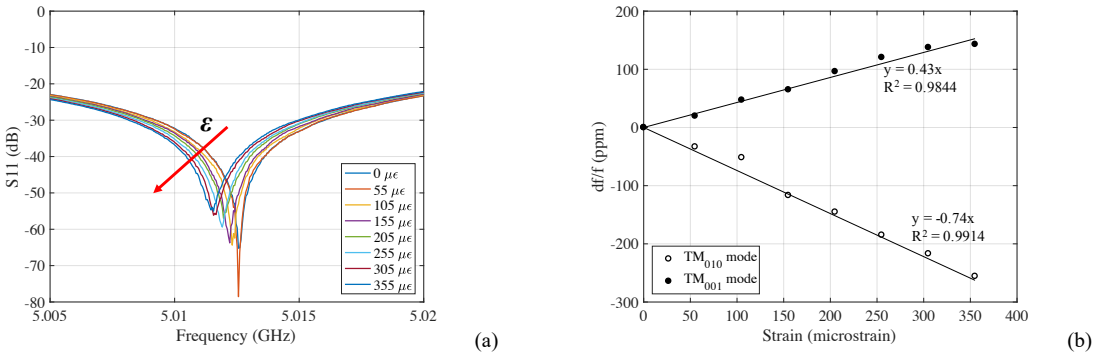

Figure 3.6. Effect of strain on the resonant frequencies of the patch antenna sensor: (a) measured S_{11} parameters of the TM_{010} mode at different strain levels; (b) linear shifts of the normalized antenna frequency with the applied strain.

Since the TCD_k of the substrate, Rogers RT/duroid 5880, is negative and much greater in magnitude than the CTE of aluminum, an increase in temperature under zero load causes the S_{11} curves of the antenna sensor to shift to the right, as validated by the experiment results presented in figure 3.7(a). The temperature sensitivity of both the TM_{010} and TM_{001} modes were obtained by plotting the normalized resonant frequency shifts as a function of temperature presented in figure 3.7(b). The temperature sensitivity of TM_{010} mode was measured as 38.2 ppm/^{o}C while the temperature sensitivity of the TM_{001} mode was measured as 40.5 ppm/^{o}C. The data presented in figure 3.7(b) display excellent linearity judging from the R^2 values of 0.9968 and 0.9994 for the

TM_{010} and TM_{001} modes respectively. Given the TCD_k of the substrate and the CTE of aluminum of 23.4 ppm/°C [150], the theoretical prediction for the temperature sensitivity of the antenna sensor as derived in (2.13) is 39.1 ppm/°C. The measured sensitivity of the antenna sensor along the TM_{010} mode is 2.3% smaller than the theoretical prediction while the measured temperature sensitivity along the TM_{001} mode is 3.6% greater than the theoretical prediction–a good agreement between the theory and the measurements.

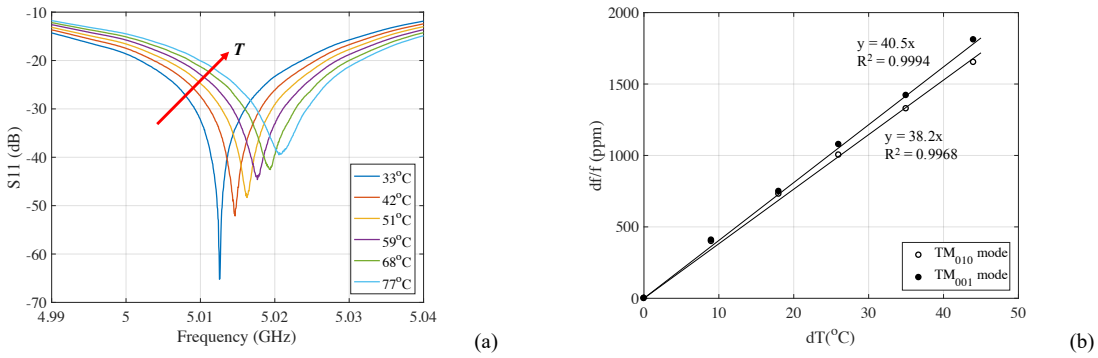

Figure 3.7. Effect of temperature on the resonant frequencies of the patch antenna sensor: (a) measured S_{11} parameters of the TM_{010} mode at different temperatures; (b) linear shifts of the normalized frequency with the temperature increase.

The simultaneous effect of temperature and strain on the antenna frequencies is presented in figure 3.8 for both the normalized resonant frequency shifts of the TM_{010} and TM_{001} modes. The antenna sensor was loaded in increments of 55 $\mu\varepsilon$ up to 355 $\mu\varepsilon$ while being exposed to temperatures from 33°C to 77°C. Since the thickness of the dog-bone specimen was chosen as 6.5 mm and its modulus of elasticity is seventy times higher than that of the substrate, the substrate was expected to expand at the same rate as the dog-bone specimen under the applied strain. As expected, the normalized f_{10} frequencies, under constant temperature, decreased with increases in the applied strain since the strain was applied in the TM_{010} mode direction. The opposite effect is shown in figure 3.8(b), where the normalized f_{01} frequency at a constant temperature increased

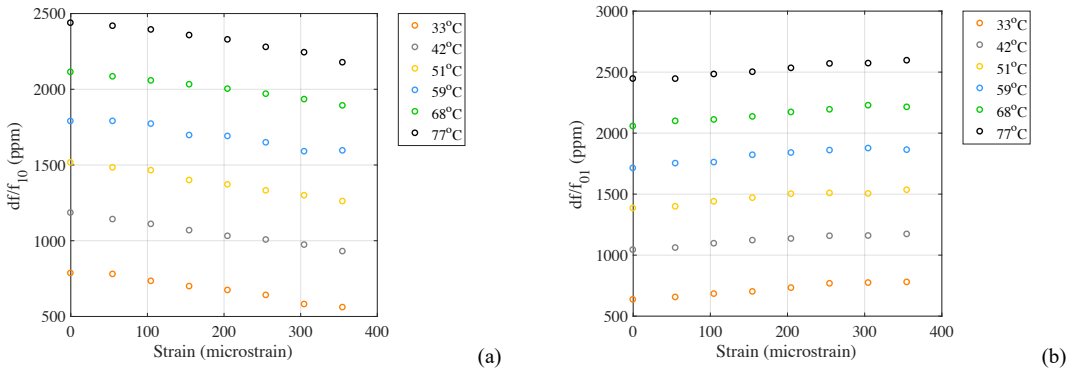

Figure 3.8. The normalized antenna frequency shifts with the applied strain under different temperatures; (a) TM_{010} mode and (b) TM_{001} mode.

with the applied strain due to the Poisson's effect. This agrees with the theory derived in (2.13). The effect of temperature is noticeable as the normalized resonant frequencies of both modes increase with temperature increase at constant strain values. Both normalized resonant frequencies appear to be linearly proportional to strain, as well as temperature. Therefore, they are curve-fitted to linear functions using the curve-fitting tool in MATLAB, which leads to

$$\frac{\delta f_{10}}{f_{10}} = 37.53\delta T - 0.6511\varepsilon_L \qquad (3.1a)$$

and

$$\frac{\delta f_{01}}{f_{01}} = 40.63\delta T + 0.4313\varepsilon_L \qquad (3.1b)$$

where δT represents the change in temperature and ε_L is the applied tensile strain. The curve-fitting indicated excellent linearity, yielding a R^2 value of 0.9979 for the TM_{010} mode and 0.9992 for the TM_{001} mode.

By applying a range of known input values (i.e., temperature and strain) and by observing the output values (i.e., the antenna sensor resonant frequency shifts) a direct relationship between input and output was established and presented in (3.1a) and (3.1b). This process is known as

calibration, and it is a standard technique for establishing a functional relationship between input and output so that the sensor or measurement system can be used in subsequent measurements to determine the unknown input values based on the output values [151], [152]. Since our objective was to extract the temperature changes and the applied strain from the normalized antenna resonant frequency shifts, inversing (3.1a) and (3.1b) gives the temperature and strain changes as functions of $\delta f_{10}/f_{10}$ and $\delta f_{01}/f_{01}$ as

$$\begin{bmatrix} \varepsilon_L \\ \delta T \end{bmatrix} = \begin{bmatrix} -0.6511 & 37.53 \\ 0.4313 & 40.63 \end{bmatrix}^{-1} \times \begin{bmatrix} \dfrac{\delta f_{10}}{f_{10}} \\ \dfrac{\delta f_{01}}{f_{01}} \end{bmatrix} \begin{pmatrix} \mu\varepsilon \\ {}^{o}C \end{pmatrix} \qquad (3.2)$$

Equation (3.2) represents the direct calibration curve and allows for easy discrimination between temperature and strain from the response of the RPA fabricated on Rogers 5880. Therefore, for any given measurements of the normalized resonant frequency shifts of the antenna sensor, equation (3.2) can be used to obtain the applied strain and/or temperature. The differences between the strain and temperature determined using equation (3.2) and the actual measurements from the strain gauges and the thermocouple are presented in figure 3.9. The measurement errors for temperature are within -0.7°C and 1°C while the measurement errors for strain are within ±40 $\mu\varepsilon$.

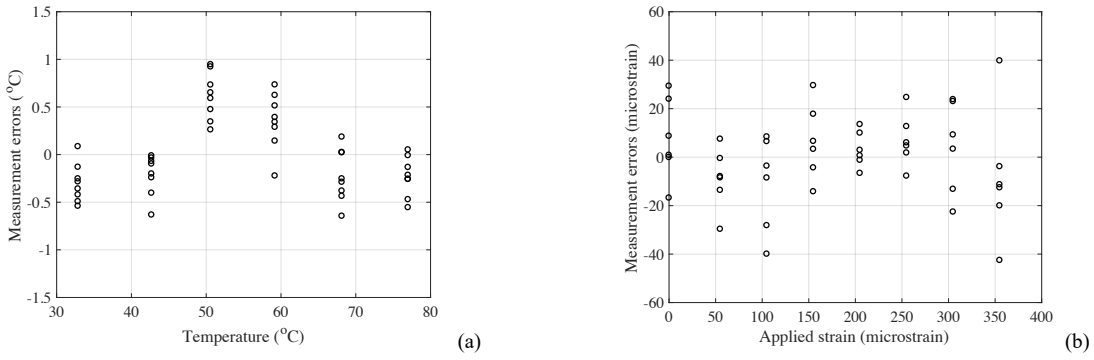

Figure 3.9. Differences between (a) temperature and (b) strain inversely determined from the normalized frequency shifts and those measured using a thermocouple and strain gauges respectively.

One standard deviation gives a temperature error of ±0.42°C and a strain error of ±17.45 $\mu\varepsilon$. The temperature error is well within the manufacturer's specified error value of ±0.5°C. These results validate the capability of a single RPA for simultaneous strain and temperature sensing.

3.5 Conclusion

In this study, we demonstrated that a single microstrip patch antenna with a rectangular radiation patch is capable of sensing strain and temperature simultaneously. A theoretical model representing the normalized antenna resonant frequency shift as linear functions of strain and temperature changes was established and validated by experimental measurements. The theoretical model also suggests that the thermal response of the dielectric substrate should be selected properly to achieve a balanced response of the antenna sensor to temperature and strain changes. By extracting the temperature and the strain from the measured antenna frequencies, the uncertainties in the measurements are ±0.42°C and ±17.45 $\mu\varepsilon$ for temperature and strain, respectively. The temperature measurement error is well within the manufacturer's specified thermocouple measurement error of ±0.5°C.

CHAPTER 4: MICROSTRIP PATCH ANTENNA FOR SIMULTANEOUS SUPERSTRATE THICKNESS AND TEMPERATURE SENSING

4.1 Introduction

The safe and efficient operation of boilers relies on accurate measurements of temperature as well as ash build-up on surfaces. Ash accumulation hinders efficient heat transfer and can lead to damage of boiler turbines, either through corrosive action or the sheer weight of deposits hanging from pendant superheaters. In this chapter, we demonstrate the simultaneous sensing of temperature and superstrate thickness using a single microstrip patch antenna. To decouple the effect of temperature variations and superstrate accumulation on the antenna sensor, we exploit the two fundamental resonant frequencies of a single antenna sensor with a rectangular radiation patch.

4.2 Principle of operation

An RPA with a superstrate, also known as a loaded RPA, is illustrated in figure 4.1. The RPA consists of a rectangular radiation patch, a dielectric substrate, a ground plane, and a superstrate above the radiation patch. The radiation patch and the ground plane are conductive materials. When separated by a dielectric material, these two components form an EM resonator with two fundamental radiation modes; the TM_{010} mode corresponds to current flow along the length direction of the radiation patch while the TM_{001} mode corresponds to current flow along the width direction of the radiation patch.

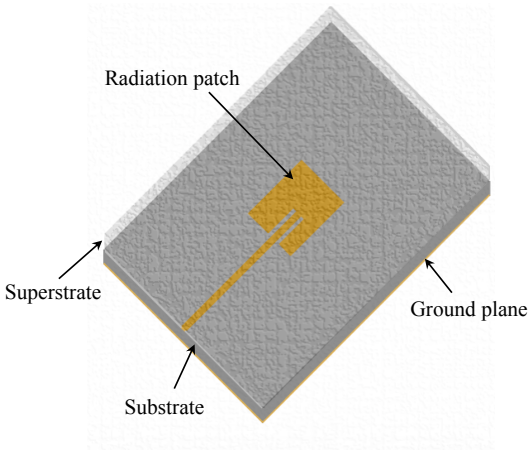

Figure 4.1. An illustration of a microstrip patch antenna temperature sensor covered with a superstrate dielectric layer.

Per the transmission line model [98], the fundamental resonant frequencies of these two fundamental modes can be determined as

$$f_{mn}=\frac{c}{2\pi\sqrt{\varepsilon_{re}}}\sqrt{\left(\frac{m\pi}{L}\right)^2+\left(\frac{n\pi}{W}\right)^2} \qquad (4.1)$$

where ε_{re}, *c, L, and W* represent the effective dielectric constant, the speed of light, the length, and the width of the radiation patch, respectively. If the dielectric constant of the superstrate is 1, that is, the superstrate is air, the RPA is called an unloaded RPA and its effective dielectric constant is approximated the same way as the dielectric constant of the substrate. However, when the RPA is loaded (i.e., the superstrate has a dielectric constant above 1.0), the dielectric constant and the thickness of the superstrate contribute to effective dielectric constant [123]. Since temperature influences the dielectric constant of the substrate and superstrate as well as the radiation patch dimensions, and the superstrate thickness affects the antenna effective dielectric constant, these two parameters can be inversely determined from the measured antenna resonant frequencies.

4.3 Antenna sensor design and fabrication

A commercial high-frequency PCB, Rogers RO3210, was selected as the substrate dielectric material for the antenna sensor due to its high dielectric constant of 10.8, and its TCD_k of -459 ppm/°C in the 0°C to 100°C range [153]. The high dielectric allows for easy miniaturization of the antenna sensor while the high TCD_k allows for high-temperature sensitivity. By selecting this substrate material, applications are limited to temperatures below 350°C as this appears to be the glass transition temperature (Tg) of the substrate. Following the design procedure described by Sanders *et al.* [106], the resonant frequencies of the antenna sensor were selected as 2.7 GHz and 3.4 GHz for the f_{10} and f_{01} frequencies respectively. The antenna sensor was modelled first using the numerical electromagnetic simulation tool Sonnet Pro 16.54. A three-dimensional (3D) view of the simulation model is presented in figure 4.2(a). The cell size of the simulation box was 0.1 mm x 0.1 mm. The top surface above the radiation patch, as illustrated in figure 4.2(a), was sectioned into two boxes with each box having a specific thickness and dielectric constant. For the box directly above the radiation patch, a dielectric constant of 1 corresponds to the

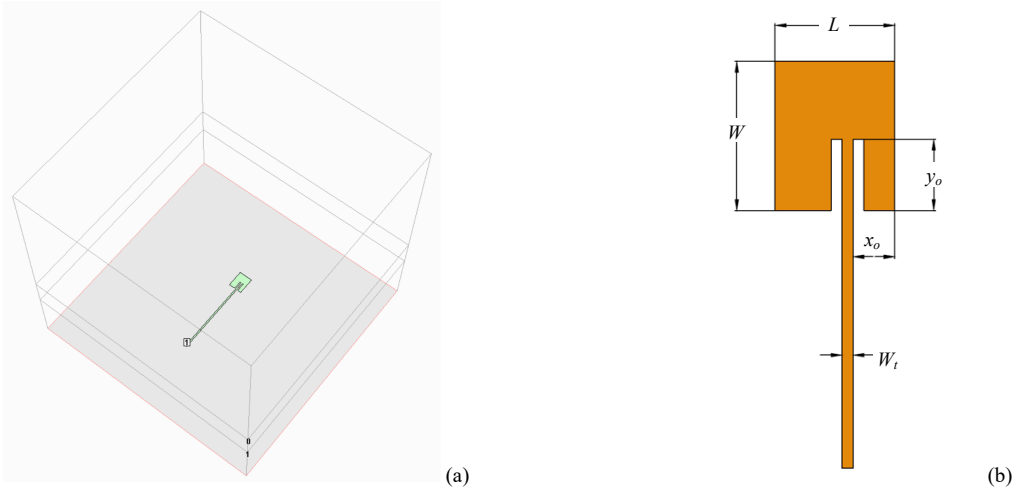

Figure 4.2. (a) The three-dimensional (3D) model of the superstrate thickness and temperature sensor simulated using Sonnet Pro; (b) physical design of the antenna sensor fed by an inset-feed microstrip transmission line.

unloaded condition. Changing the dielectric constant of this box/layer to any value other than 1 will be considered the loaded condition and thus represents the presence of a superstrate above the radiation patch. The second box above the radiation patch was considered air and thus assigned a dielectric constant of 1. To excite the fundamental radiation modes of the antenna, the antenna sensor was inset-fed using a 50 Ω microstrip transmission line that terminated with a 50 Ω SMA connector. Figure 4.2(b) presents the physical design of the antenna sensor with the microstrip transmission line. Due to the inset-feed design, there is coupling between the impedances of the two antenna resonant modes. Therefore, to find an optimized feeding location of the antenna sensor, a parametric sweep in x_0 and y_0 was carried out. Given the desired resonant frequencies, the manufacturer specified substrate dielectric constant ε_{r1} of 10.8 and a substrate thickness of 1.27 mm, the radiation patch dimensions were calculated as 13.6 mm in length and 10.9 mm in width. The 50 Ω microstrip line width, W_t was calculated as 1.1 mm. Based on the parametric study, the inset-feed position was selected as 3.8 mm and 6.5 mm for x_0 and y_0 respectively.

After determining the dimensions of the radiation patch, the next step was to study the effect of the superstrate dielectric constant ε_{r2} on the antenna sensor. For this study, the superstrate thickness was kept as 1 mm while its dielectric constant was varied from 1 to 6 in steps of 0.5. Figure 4.3 presents the simulated antenna resonant frequencies as a function of the superstrate dielectric constant. The resonant frequencies of the antenna decrease linearly with an increase in the superstrate dielectric constant. The effective dielectric constant of the loaded antenna sensor can be determined from the f_{01} resonant frequency [123], that is,

$$f_{01}=\frac{c}{2W\sqrt{\varepsilon_{re}}} \qquad (4.2)$$

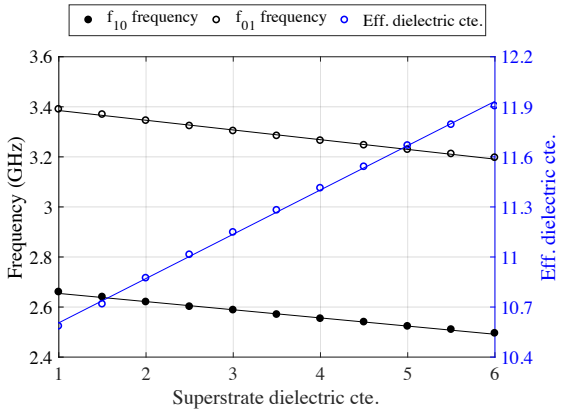

Figure 4.3. The simulated effect of superstrate dielectric constant on the resonant frequencies of the patch antenna and the effective dielectric constant derived from the frequency shift.

Calculated from the simulated antenna frequency using equation (4.2), figure 4.3 shows a linear increase of the effective dielectric constant of the loaded antenna sensor as a function of the superstrate dielectric constant. In the unloaded condition (i.e., $\varepsilon_{r2} = 1$), the extracted effective dielectric constant obtained by simulation is 10.67 and this agrees with the substrate dielectric constant of 10.8. This agreement confirms that in the unloaded condition, the effective dielectric constant can be approximated as the substrate dielectric constant. The effective dielectric constant of the antenna can also be extracted using the f_{10} frequency (i.e., the resonant frequency along the length direction of the antenna). If using the f_{10} frequency, one must consider the effective length of the antenna because the current flow along this direction is significantly affected by the inset-feed design, which causes a significant current deviation in the length direction. When accounting for this current deviation, the effective dielectric constant extracted from the f_{01} and f_{10} resonant frequencies are in good agreement. We observed a maximum difference of 0.07 and a minimum difference of 0.002 between both extracted values.

The next step was to simulate the effect of superstrate thickness and temperature changes on the antenna sensor frequencies. Before selecting the superstrate dielectric constant for this step,

at this point, it is worth mentioning that the broad range of microwave applications demands a detailed knowledge of the dielectric properties of materials. Considering the broad range of dielectric constants of various dielectric materials [154], the antenna sensor should be characterized for specific applications. If the dielectric properties of the superstrate are unknown, they can be extracted using well-established microwave material characterization techniques [136], [139], [155]–[157]. Since the simulated study will have to be validated by experiments so we can achieve our primary objective, which is to demonstrate simultaneous superstrate thickness and temperature detection using an antenna sensor, we have chosen Rogers 3003 as superstrate material due to the detailed literature available on the properties of this PCB.

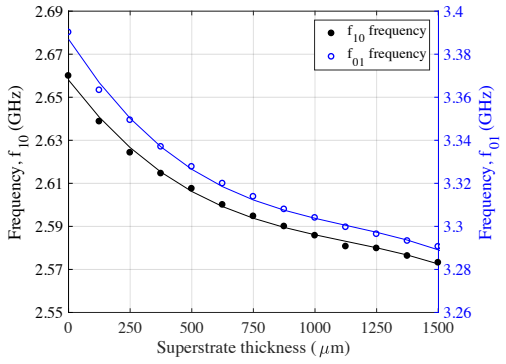

Figure 4.4. The simulated effect of superstrate thickness on the antenna resonant frequencies.

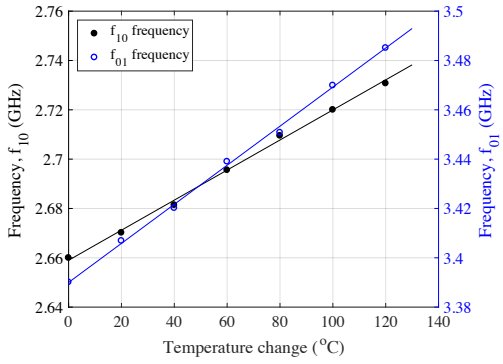

Figure 4.5. The simulated effect of temperature on the antenna resonant frequencies.

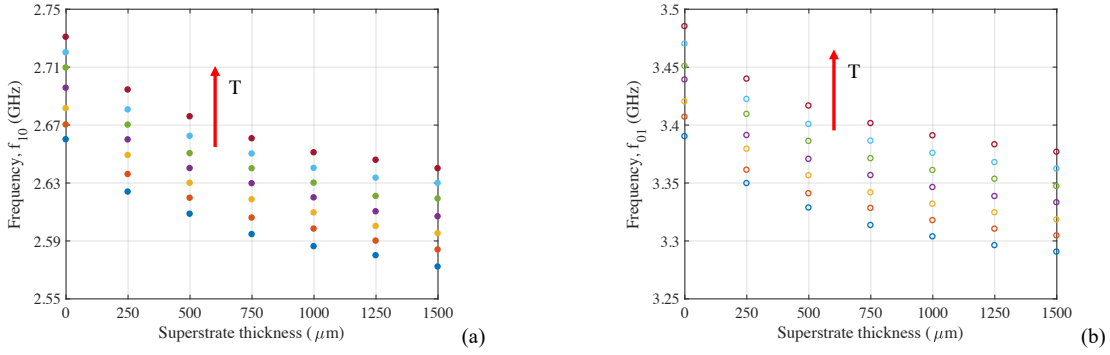

Figure 4.6. The simulated effect of temperature and superstrate thickness variations on the resonant frequencies of the patch antenna sensor: (a) f_{10} frequency and (b) f_{01} frequency.

Rogers 3003 has a dielectric constant of 3 and a TCD_k of -3 ppm/^oC [158]. Therefore, to study the effect of superstrate thickness on the antenna frequencies at a constant temperature, the superstrate dielectric constant was set to 3, and its thickness was increased in increments of 125 μm up to a maximum of 1500 μm. Figure 4.4 presents the simulated results; the resonant frequencies of the antenna sensor decrease with an increase in superstrate thickness. Judging from the trend, a polynomial function is a good fit between the simulated antenna frequencies and the superstrate thickness. To simulate the effect of temperature only, the TCD_k of the substrate and superstrate were used. Given a TCD_k of -459 ppm/^oC for the substrate material and a CTE of the conductors of -16 ppm/^oC, the thermal response of the antenna sensor will be dominated by the TCD_k of the substrate material [148]. Therefore, to reduce computational time, we only considered the effect of temperature on the dielectric layer given that the antenna frequency will be predominantly affected by the change in dielectric constant of the substrate. For every 20^oC, the substrate dielectric constant will decrease by 0.1. This value was obtained using the formula $\Delta\varepsilon_r = \varepsilon_r \cdot TCD_k \cdot dT$, where $\Delta\varepsilon_r$ represents the change in dielectric constant and dT the change in temperature; dT equals 0 is considered the room temperature condition. The simulated effect of temperature on the antenna sensor in the unloaded state is presented in figure 4.5. As demonstrated in figure 4.5, the antenna resonant frequencies increase linearly with temperature, as expected, given the TCD_k varies linearly with temperature within the simulated temperature range. As presented in figure 4.4 and 4.5, both temperature and superstrate thickness variations influence the antenna resonant frequencies. Therefore, the two fundamental resonant frequencies of the antenna are needed to decouple the effect of these measurands. Figure 4.6 presents the simulated effect of temperature and superstrate thickness on the resonant frequencies of the antenna. The temperature was simulated in steps of 20^oC up to a maximum temperature change of 120^oC, while the

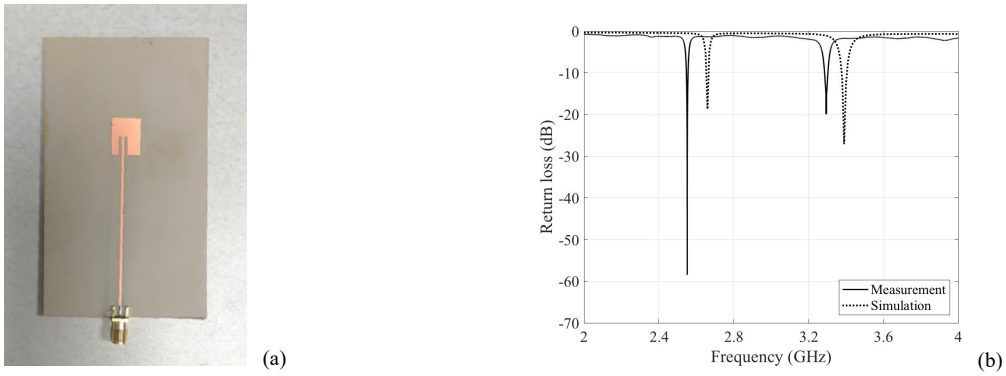

Figure 4.7. (a)The antenna sensor fabricated on Rogers 3210 printed circuit board (PCB) using print-etching technique; and (b) a comparison between simulated and measured S_{11} curves of the antenna sensor.

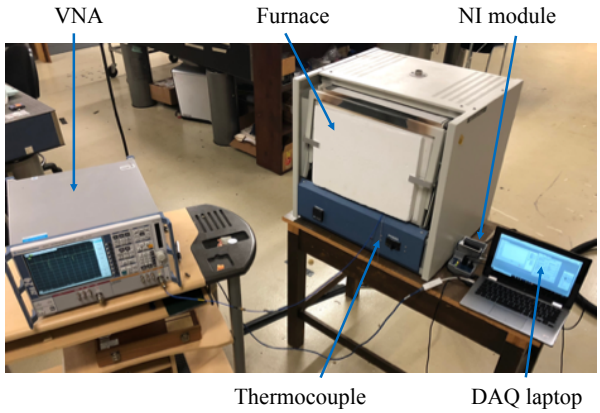

Figure 4.8. The experimental setup for characterizing the antenna sensor.

superstrate thickness was increased from 0 to 1500 µm in steps of 250 µm. As illustrated in figure 4.6, the f_{10} and f_{01} frequencies increase with an increase in temperature at constant superstrate thickness, and the frequencies decrease with an increase in the superstrate thickness at a constant temperature.

After completion of simulations, the RPA was fabricated on Rogers 3210 PCB by print-etching technique. This technique consists of printing the simulated antenna pattern on a transfer paper film (Techniks PNPB20). The printed pattern is then transferred from the film to the selected PCB using a heat source such as a clothing iron. Afterward, the PCB is immersed in ferric chloride for chemical etching of the exposed copper. Finally, acetone is used to remove ink residue from

the PCB. To measure the S_{11} parameters of the antenna sensor, a 50 Ω SMA connector is attached at the end of the microstrip transmission line by soldering. Figure 4.7(a) presents the fabricated antenna sensor on Rogers 3210 while figure 4.7(b) presents a comparison between a simulation obtained in Sonnet Pro and measurements obtained from a VNA, Rohde & Schwarz ZVA24). As shown in figure 4.7(b), the measured resonant frequencies are 2.552 GHz and 3.295 GHz for the f_{10} and f_{01} frequencies respectively. The maximum difference between measurement and simulation is 0.1 GHz. This is most likely due to the fabrication, the difference between the dielectric constant set in the simulation and the actual dielectric constant of the Rogers PCB, and/or the parasitic capacitance introduced by the SMA connector [159]. Due to the difficulty in achieving an exact match between simulation and measurements, the simulated results will only be used for the preliminary design of the patch antenna, while its actual performance will be based on results from experiments.

4.4 Instrumentation and experimental setup

The experimental setup for characterizing the simultaneous effects of temperature and superstrate thickness on the antenna resonant frequencies is presented in figure 4.8. A Thermo-Fisher furnace was used to heat the antenna sensor up to 140ºC. To monitor temperature variations during the heating process, an OMEGA T-type thermocouple was positioned adjacent to the antenna sensor. This thermocouple was selected because of its low measurement errors of ±0.5ºC or ±0.4% of the measured temperature value (whichever is greater). Data from the thermocouple were acquired using a thermocouple module (National Instrument, NI 9211). To acquire the S_{11} curves of the antenna sensor, a coaxial cable was used to connect the 50 Ω termination port of the antenna sensor to the VNA. The VNA was programmed to sweep from 2 GHz to 4 GHz with a

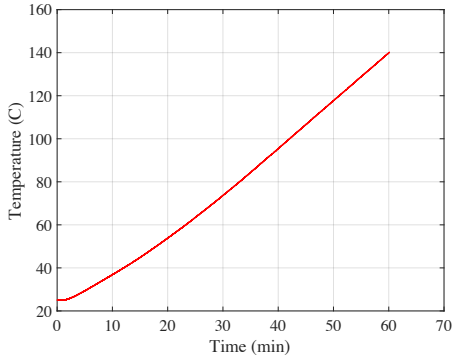

Figure 4.9. The thermocouple temperature measurements during the antenna sensor characterization.

frequency resolution of 200 kHz. Both the thermocouple module and the VNA were controlled using a computer program written in LabVIEW. Data acquired from these instruments were time stamped for ease of correlation during data processing/analysis. The temperature profile during the antenna sensor characterization is presented in figure 4.9; the maximum recorded temperature was 140°C. Given the manufacturer's specifications, the maximum thermocouple measurement error is expected to be ±0.56°C.

4.5 Results and discussion

4.5.1 Results obtained using Rogers 3003 as superstrate

Before characterizing the microstrip antenna sensor for simultaneous superstrate thickness and temperature sensing, the individual effect of each measurand on the antenna sensor response was first examined. For temperature sensing only, since the TCD_k of Rogers 3210 PCB is -459 ppm/°C and is much greater in magnitude than the CTE of the conductors (16 ppm/°C), an increase in temperature will result in a shift to the right of the S_{11} curves. This corresponds to a frequency increase of the antenna sensor, and it is validated by the measurements presented in figure 4.10(a). The temperature sensitivities of both the f_{10} and f_{01} resonant frequencies of the antenna sensor are

presented in figure 4.10(b). The measured temperature sensitivities of the antenna sensor are 449.7 kHz/°C and 623.2 kHz/°C for the f_{10} and f_{01} resonant frequencies, respectively. Both measurements display excellent linearity with R^2 values of 0.9992 and 0.9990 for f_{10} and f_{01} frequencies, respectively. From the measured sensitivities, the extracted TCD_k of the substrate is -403 ppm/°C– this value is 12% smaller than the manufacturer's specified TCD_k of -459 ppm/°C. The extracted TCD_k of the substrate fits well within the 15% variation often reported by Rogers.

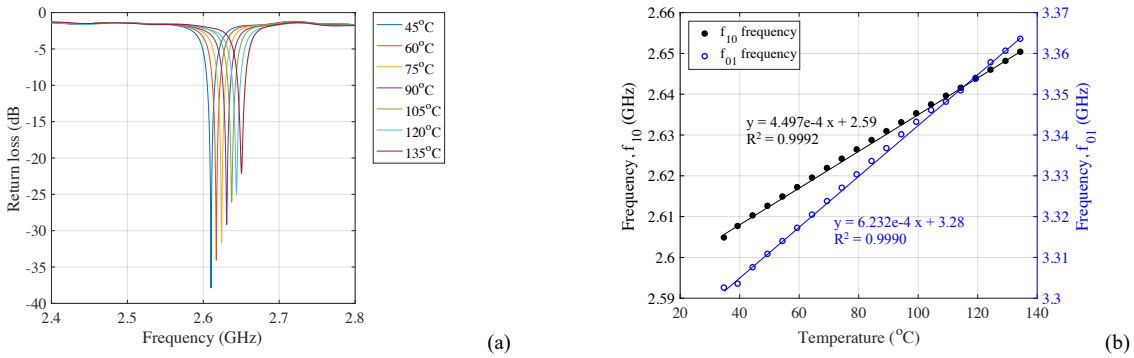

Figure 4.10. The measured effect of temperature on the resonant frequencies of the microstrip patch antenna sensor fabricated on Rogers 3210 PCB: (a) S_{11} curves of the f_{10} frequency at different temperatures; (b) linear shifts of the antenna sensor's resonant frequencies with temperature increase.

To assess the effect of superstrate thickness on the antenna sensor performance, Rogers 3003 dielectric material was stacked on the radiation patch in increments of 250 µm up to a maximum of 1500 µm. At each increment, the antenna S_{11} curves were measured using the VNA, and the results are plotted in figure 4.11(a) for the f_{10} resonant frequency. With an increase in superstrate thickness, the S_{11} curves shift to the left–this indicates a decrease in the antenna resonant frequencies. The measured frequencies are plotted as a function of superstrate thickness in figure 4.11(b) and are curved fitted using quadratic polynomial functions in MATLAB. The established relationship between the measured resonant frequencies (in GHz) and the superstrate

thickness, d (in µm), is given as f_{10} = 1.877e-8 · d^2 – 6.188e-5 · d + 2.551 and f_{01} = 2.799e-8 · d^2 – 8.307e-5 · d + 3.294. The achieved R^2 values were 0.9980 and 0.9963 for the f_{10} and f_{01} resonant frequencies respectively. The simulation and measurements agree when comparing the trend of data in figure 4.10 with figure 4.5, and figure 4.11 with figure 4.4.

To establish a direct correlation between the antenna outputs (i.e., the antenna sensor resonant frequencies f_{10} and f_{01}) and the measurands of interest (i.e., the temperature and superstrate thickness), the standard sensor calibration technique as described by Figliola [151] and Bentley [152] was followed. The antenna sensor was loaded in increments of 250 µm thick

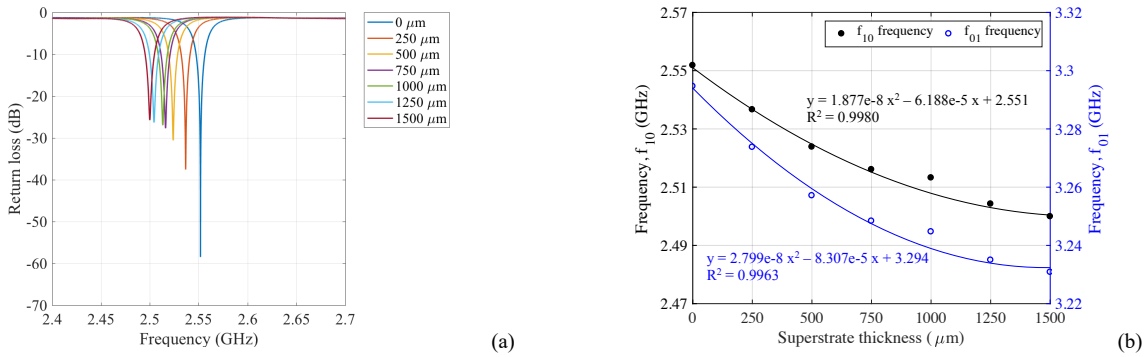

Figure 4.11. The measured effect of Rogers 3003 superstrate thickness on the resonant frequencies of the antenna sensor at 23°C: (a) S_{11} curves of the f_{10} frequency with different thicknesses of superstrate; (b) the antenna frequencies shifts with an increase in superstrate thickness.

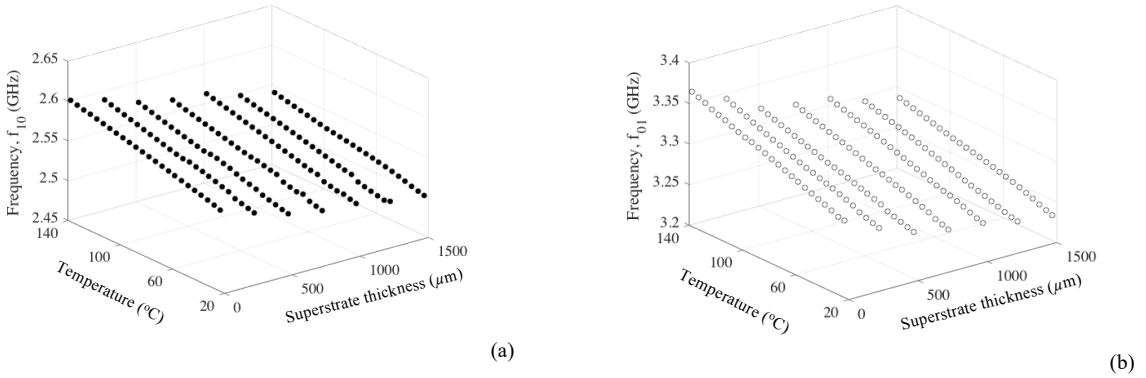

Figure 4.12. The measured effects of temperature and superstrate thickness on the (a) f_{10} and (b) f_{01} antenna resonant frequencies. Rogers 3003 dielectric material is serving as superstrate.

superstrate dielectric material up to a maximum of 1500 μm while being subjected to temperatures from 23°C to 140°C. The measured antenna resonant frequencies to the combined effects of temperature and superstrate thickness are plotted in figure 4.12(a) and 4.12(b). As expected, the f_{10} and f_{01} frequencies, under constant temperature, decreased with increases in superstrate thickness. Under the effect of temperature only (i.e., at constant superstrate thickness), the f_{10} and f_{01} antenna frequencies increased linearly with an increase in temperature. To inversely determine the superstrate thickness and the temperature from the antenna sensor frequencies, the measurements were curve-fitted in MATLAB using quadratic functions for the superstrate thickness and linear functions for the temperature. This yielded:

$$f_{10} = 2.54 - 5.151e^{-5} \cdot d + 12.39e^{-9} \cdot d^2 - 51.62e^{-9} \cdot d \cdot T + 4.617e^{-4} \cdot T \quad (4.3a)$$

and

$$f_{01} = 3.277 - 7.251e^{-5} \cdot d + 23.89e^{-9} \cdot d^2 - 93.84e^{-9} \cdot d \cdot T + 6.338e^{-4} \cdot T \quad (4.3b)$$

where T represents the temperature in °C, d the superstrate thickness in μm, f_{10} and f_{01} the antenna resonant frequencies in GHz. The achieved R^2 values were 0.9911 and 0.9900 for the f_{10} and the f_{01} frequencies, respectively. Given the curve-fitting equations presented in equation (4.3), a computer program was developed to inversely determine the superstrate thickness and the temperature from the measured resonant frequencies of the antenna sensor. The inverse algorithm searches the entire superstrate thickness range in steps of 25 μm. For every assumed value of d, the temperature is solved from equation (4.3), which is now a single-variable linear function since the antenna frequencies are known. The resulting (d, T) pairs are subsequently saved and once the entire superstrate thickness range was searched, the (d, T) set that yielded the lowest difference between actual measurements and estimated values was considered the measured superstrate thickness and temperature. A comparison between the estimated temperature and the superstrate

thickness inversely determined from equation (4.3) and the actual input values is presented in figure 4.13. One standard deviation gives a temperature error of ±0.71ºC and a superstrate thickness error of ±70.69 μm. The temperature error agrees with the thermocouple measurement error of ±0.56ºC, and it represents ±0.51% of the maximum applied temperature of 140ºC. The superstrate thickness error of ±70.69 μm represents 4.7% of the maximum applied thickness of 1500 μm.

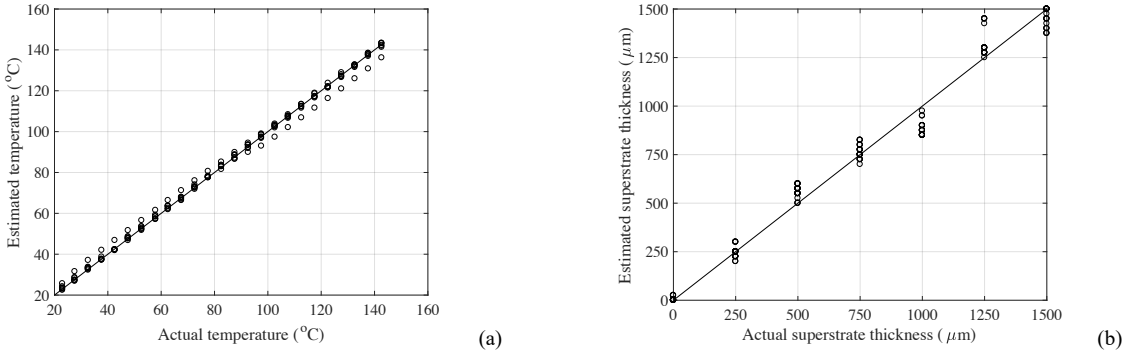

Figure 4.13. A comparison between Rogers 3003 superstrate thickness and temperature inversely determined from the antenna frequencies and actual inputs: (a) temperature, and (b) superstrate thickness.

4.5.2 Results obtained using ash from charcoal briquettes as superstrate

Rogers 3003 dielectric material, previously used as a superstrate, was replaced by ash obtained from burning charcoal briquettes (Embers charcoal briquettes, model 192-355-140). The first step was to extract the dielectric constant of ash since charcoal briquettes can vary widely in composition [160]. The extracted dielectric constant can be used in simulation tools to define the design space by conducting a parametric study of the effect of ash on the antenna frequencies. For the purpose of extracting the dielectric constant of ash, a 1000 μm thick layer of ash was placed on the antenna sensor, and the effective dielectric constant of the loaded antenna was calculated using equation (7) from [123]. Given the effective dielectric constant of the unloaded antenna (ε_{ro}

= 11.21) and the measured antenna resonant frequencies of f_r = 3.231 GHz and f_{ro} = 3.295 GHz corresponding to the loaded and unloaded state of the antenna, respectively, the effective dielectric constant of the ash-loaded sensor was calculated as 11.65. Based on the relationship between the effective dielectric constant of the superstrate-loaded antenna and the dielectric constant of the superstrate shown in figure 4.3, the dielectric constant of ash was determined to be 2.64. The approach used for extracting the dielectric constant of ash is similar to well-established microwave material characterization techniques using microwave resonators [139], [161].

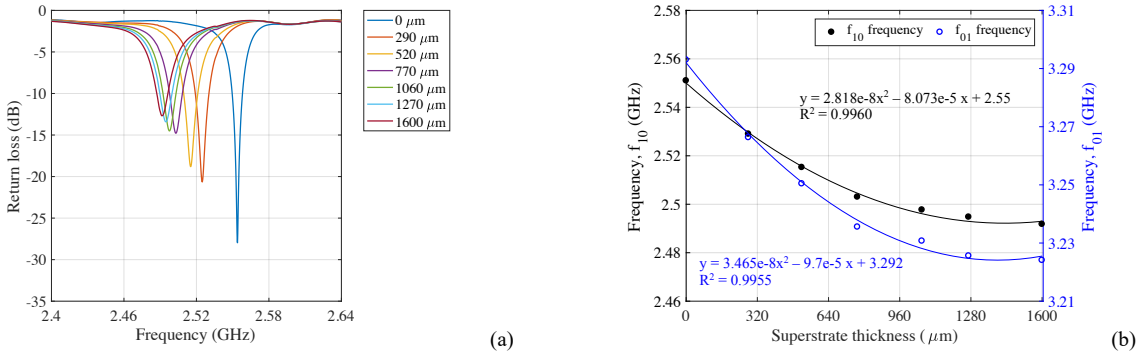

Figure 4.14. The measured effect of ash accumulation on the resonant frequencies of the microstrip patch antenna sensor at 23°C: (a) S_{11} curves of the f_{10} frequency with different thicknesses of ash; (b) shifts of the antenna resonant frequencies with increase in ash thickness.

Before characterizing the microstrip patch antenna for simultaneous ash thickness and temperature sensing, the effect of ash accumulation on the antenna was assessed experimentally. To accomplish this task, the antenna sensor was covered with ash up to 1600 µm. Figure 4.14(a) presents the measured S_{11} curves of the antenna sensor for the f_{10} resonant frequency at each loading increment, while figure 4.14(b) presents the measured frequencies as a function of ash thickness. As illustrated in figure 4.14, the antenna resonant frequencies decrease with an increase in ash accumulation over the radiation patch. The measured data are curve-fitted to establish a relationship between the antenna frequencies (in GHz) and the ash thickness, d (in µm). Using

quadratic polynomial functions in MATLAB, we obtained the curve fit equation as: f_{10} = 2.818e-8 · d^2 – 8.073e-5 · d + 2.55 and f_{01} = 3.465e-8 · d^2 – 9.7e-5 · d + 3.292. The achieved R^2 values were 0.9960 and 0.9955 for the f_{10} and f_{01} resonant frequencies respectively.

Next, the simultaneous effect of ash accumulation and temperature variations on the antenna resonant frequencies was also established by following the standard sensor calibration techniques as described in [151], [152]. The antenna sensor was covered with ash incrementally up to a maximum thickness of 1600 μm while being exposed to temperatures from 23ºC to 140ºC. The measured antenna frequencies to the simultaneous effects of temperature and ash accumulation are plotted in figure 4.15(a) and 4.15(b). As anticipated, the f_{10} and f_{01} antenna frequencies decreased with ash build-up under constant temperature. At constant ash thickness, the f_{10} and f_{01} antenna frequencies increased linearly with an increase in temperature. The measurements were curve-fitted in MATLAB using quadratic functions for the superstrate thickness and linear functions for the temperature. This gives:

$$f_{10} = 2.539 - 7.896e^{-5} \cdot d + 26.08e^{-9} \cdot d^2 - 6.654e^{-9} \cdot d \cdot T + 4.711e^{-4} \cdot T \quad \text{(4.4a)}$$

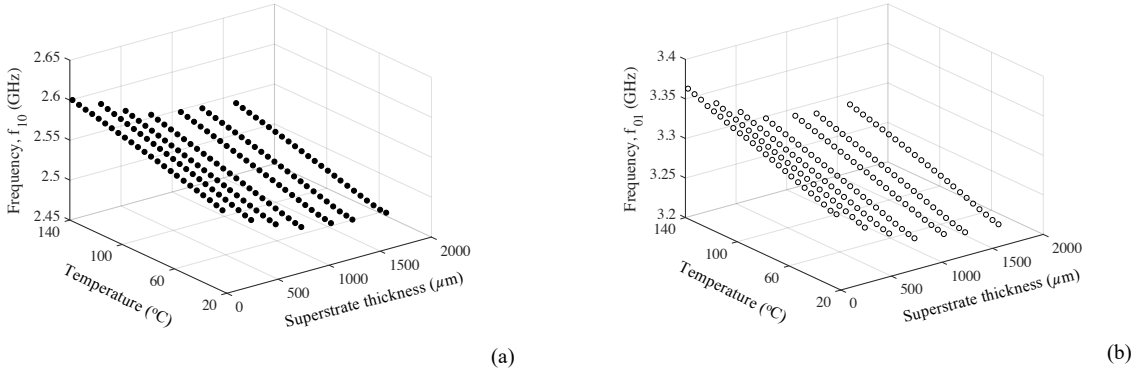

Figure 4.15. The measured effects of ash accumulation and temperature changes on the (a) f_{10} and (b) f_{01} frequencies of the antenna sensor.

and

$$f_{01} = 3.279 - 1.025e^{-4} \cdot d + 38.91e^{-9} \cdot d^2 - 40.51e^{-9} \cdot d \cdot T + 6.099e^{-4} \cdot T \quad (4.4b)$$

where T represents the temperature in ^{o}C, d the ash thickness in μm, f_{10} and f_{01} the antenna resonant frequencies in GHz. The achieved R^2 values were 0.9965 and 0.9982 for the f_{10} and the f_{01} frequencies, respectively. Equation (4.4) enables us to inversely determine the ash thickness and the temperature from the antenna sensor frequencies. A comparison between the ash thickness and the temperature inversely determined from the antenna resonant frequencies using equation (4.4) and actual input values is presented in figure 4.16. The difference between actual and estimated ash thickness varies from -25 μm to 170 μm. The maximum error occurs at an ash thickness of 1270 μm as illustrated in figure 4.16(b). One standard deviation gives an ash thickness error of ±58.05 μm and a temperature error of ±0.58^{o}C. The temperature measurement error agrees with the thermocouple measurement error of ±0.56^{o}C, and it represents ±0.4% of the maximum applied temperature of 140^{o}C. The superstrate thickness error of ±58.05 μm represents 3.6% of the maximum applied ash thickness of 1600 μm.

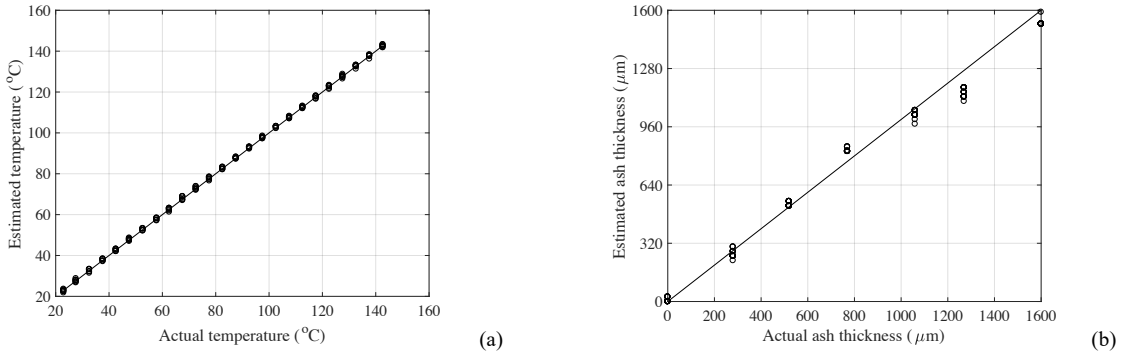

Figure 4.16. A comparison between ash thickness and temperature inversely determined from the antenna sensor frequencies and actual inputs: (a) temperature, and (b) ash thickness.

4.6 Conclusion

In this study, we demonstrated that superstrate thickness and temperature could be simultaneously measured using a dual-frequency rectangular patch antenna. The temperature and the superstrate thickness were inversely determined from the measured antenna resonant frequencies. Experiments were conducted using two dielectric materials (Rogers 3003 and ash from charcoal briquettes) as a superstrate. Using Rogers 3003, by comparing the superstrate thickness and temperature extracted from the measured antenna frequencies to the actual input values, we obtained measurement errors of ±0.71°C and ±70.69 μm for temperature and superstrate thickness, respectively. Using ash as a superstrate, we obtained measurement errors of ±0.58°C and ±58.05 μm for temperature and superstrate thickness respectively. In both cases, the temperature errors agree with the thermocouple measurement error of ±0.56°C.

CHAPTER 5: FAR-FIELD INTERROGATION OF A MICROSTRIP PATCH ANTENNA TEMPERATURE SENSOR WITHOUT ELECTRONICS

5.1 Introduction

Current sensing technologies with onboard electronics are not suitable for high-temperature sensing applications. To overcome the limitations of these sensor technologies and increase the operational temperature, in this chapter, we demonstrate wireless interrogation of a high-temperature antenna sensor without electronics. The work presented in this chapter was achieved in collaboration with Dr. Jun Yao [162]. I focused on the antenna sensor design and the characterization of the antenna sensor package for high-temperature sensing applications. The sensor node is entirely passive and consists of a UWB Tx/Rx antenna and a microstrip patch antenna serving as the temperature sensing element. A microstrip transmission line connecting the UWB Tx/Rx antenna and the antenna sensor delays the signal reflected from the sensing element and thus separates it from the background clutter. Temperature changes the dielectric constant of the substrate because of its thermal coefficient of dielectric constant, and it also changes the radiation patch dimensions because of the coefficient of thermal expansion of the conductors [163]. It was, therefore, possible to extract temperature from the measured antenna frequency since this frequency is a function of the radiation patch dimension and the effective dielectric constant of the antenna. The principle of operation of the wireless sensing scheme, the design, and simulations of the sensor node circuitry are discussed in this chapter. Furthermore, a digital signal

processing algorithm that extracts the antenna resonant frequency from the wirelessly received signal is also described.

5.2 Principle of operation

The wireless sensing system can be separated into two subsystems: a wireless interrogator and a passive wireless sensor node, as illustrated in figure 5.1. The sensor node consists of a patch antenna sensor and a UWB Tx/Rx antenna connected with a microstrip transmission line. The Tx/Rx antenna is used to receive the wideband interrogation signal from the interrogator and rebroadcast the signals reflected by the antenna sensor (i.e., the antenna sensor backscattering) back to the wireless interrogator. To avoid the self-jamming problem [43], the microstrip transmission line is used to introduce a time delay between the background clutter and the antenna sensor backscattering. As long as the transmission line is of sufficient length, the antenna reflection can be distinguished from the background clutter in the time domain. The wireless interrogator is based on measuring the two-port transmission scattering parameter, the S_{21} parameter) between the two interrogation antennas. A linear chirp interrogation signal is generated and broadcasted to the passive wireless sensor through the antenna connected to port 1 of the interrogator. This

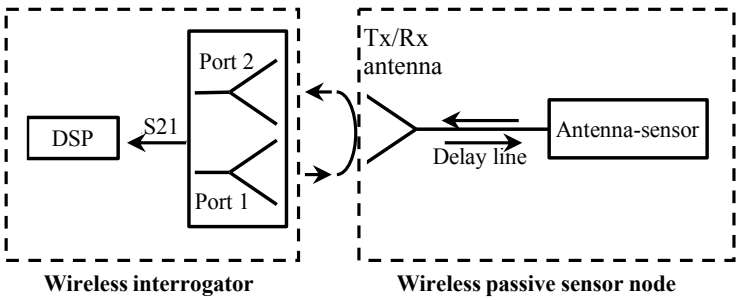

Figure 5.1. A block diagram of the wireless temperature sensing system.

interrogation signal is received by the UWB Tx/Rx antenna of the sensor node and transmitted to the antenna sensor via the microstrip delay line. Upon reaching the antenna sensor, the portion of the interrogation signal that matches the antenna resonant frequency is received and radiated by the antenna sensor. The remaining interrogation signal is reflected by the antenna sensor and broadcasted back to the interrogator via the Tx/Rx antenna. As such, the reflection coefficient of the antenna sensor is encoded into the backscattered signal. The power of the antenna backscattering received by the interrogator can be calculated using the Friis equation:

$$P_r = P_t G_{it} G_{ir} {G_s}^2 \left(\frac{\lambda}{4\pi d} \right)^4 S_{11} L_d \qquad (5.1)$$

where P_t is the power of the transmitted interrogation signal, d is the distance between the wireless interrogator and the Tx/Rx antenna, G_{it} and G_{ir} are the radiation gains of the interrogator Tx/Rx antennas, G_s is the radiation gain of the UWB sensor antenna, λ is the wavelength of the interrogation signal, S_{11} is the reflection coefficient of the antenna sensor, and L_d is the loss introduced by the delay line. The minimum detectable power of the wireless interrogator can be expressed as [118]:

$$P_{r\min} = E \cdot B \cdot F \cdot SNR \qquad (5.2)$$

where E is the thermal energy; B is the bandwidth of the receiver; F is the noise figure of the interrogator receiver, and SNR is the required signal to noise ratio for this system. Substituting (5.1) into (5.2), the theoretical maximum interrogation distance can be calculated as

$$d_{\max} = \frac{\lambda}{4\pi} \left(\frac{P_t G_{tt} G_{tr} {G_r}^2 S_{11} L_d}{E \cdot B \cdot F \cdot SNR} \right)^{\frac{1}{4}} \qquad (5.3)$$

Once the backscattered signals, including the antenna sensor backscattering and the background clutter, are received by the interrogator, they are

processed by a digital signal processing (DSP) program to separate the antenna sensor backscattering from the background clutter. Frequency analysis can then be performed on the antenna sensor backscattering to extract the resonant frequency of the antenna sensor.

5.3 Sensor node implementation

5.3.1 Design of temperature antenna sensor

A commercial high-frequency circuit laminate, Rogers RO3210 [153], was selected as the substrate material for the wireless sensor because of its high thermal coefficient of dielectric constant α_ε, which is -459 ppm/°C in the temperature range from 0°C to 100°C. Compare to α_ε, its thermal expansion coefficient α_T of 13 ppm/°C is much smaller. Based on equation (2.13), the theoretical temperature sensitivity of the normalized frequency shift K_T is calculated to be 216.5 ppm/°C. By selecting this substrate, the sensor is limited to applications with temperatures below 350°C as this appears to be the glass transition temperature (Tg) of the substrate. A material operating above its Tg temperature usually undergoes a drastic change in CTE and becomes mechanically and electrically unstable [158]. Selecting a PCB with high Tg will be part of our future work as this will enable the use of this sensor for many applications such as gas turbines, furnaces, and jet engines.

The radiation patch of an antenna sensor with a designed frequency of 2.45 GHz is shown in figure 5.2. The radiation patch is fed with a 50 Ω microstrip transmission line to excite the fundamental radiation mode along the width direction. To obtain a good impedance matching between the transmission line and the radiation patch, the inset-fed structure was used. The 50 Ω feeding point was calculated at the position of 7.04 mm above the bottom edge of the radiation

patch. The length of the transmission line was selected to be 200 mm to ensure sufficient separation between the UWB Tx/Rx antenna and the antenna sensor.

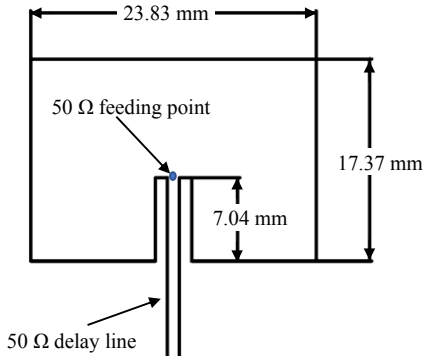

Figure 5.2. The physical dimensions and feeding structure of the designed microstrip antenna sensor.

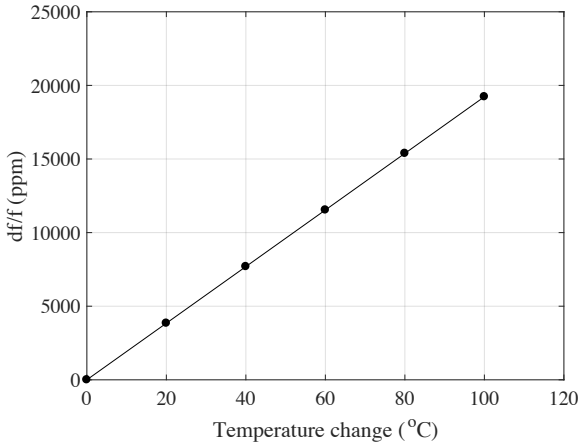

Figure 5.3. The simulated relationship between the antenna sensor's normalized resonant frequency shift and the temperature.

To confirm the antenna design, a 3D model of the designed antenna sensor was developed in HFSS. For a substrate dielectric constant of 10.8 at room temperature (20°C), every 20°C increase in temperature will reduce the dielectric constant by 10.8 x 459 ppm/°C x 20°C = 0.1. Thus, the substrate dielectric constant of the simulation model was varied from 10.9 to 10.4 with a step of -0.1, which corresponds to temperature changes from 0°C to 100°C. The simulated resonant frequencies were normalized with respect to the frequency at room temperature and are

plotted versus the temperature in figure 5.3. The simulated curve displays excellent linearity (R^2 = 0.995) and the resulting temperature sensitivity K_T (i.e., the slope of the trend line) is 192.3 ppm/°C–11.2% smaller than the value of 216.5 ppm/°C predicted by the transmission line model.

The antenna sensor and the delay line were fabricated using a chemical etching technique, as illustrated in figure 5.4. To characterize the round-trip time delay caused by the delay line, a 50 Ω SMA connector was soldered on the end of the delay line. The S_{11} parameter of the fabricated antenna sensor was first measured using a VNA and then converted to the time domain response represented in figure 5.5. The wave packet corresponding to the antenna backscattering starts at 3.5 ns, which is the round-trip time delay between the SMA connector and the antenna sensor.

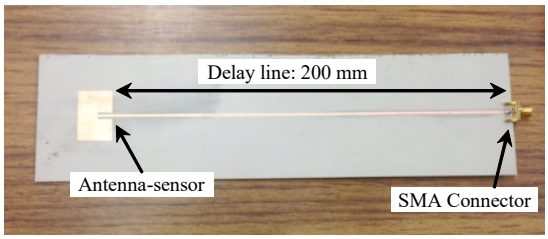

Figure 5.4. The fabricated antenna-senor with the microstrip delay line.

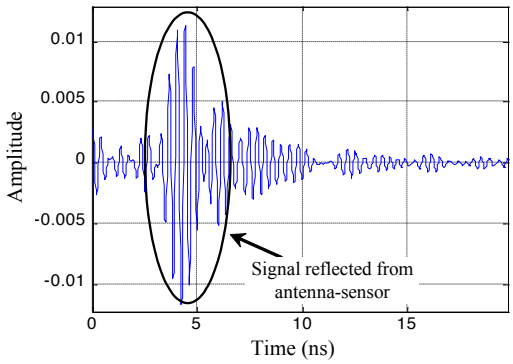

Figure 5.5. The time domain signal converted from the measured S_{11} parameter of the fabricated antenna sensor with the delay line.

5.3.2 Design of the UWB Tx/Rx microstrip antenna

To implement the entire sensor node on PCBs, the UWB Tx/Rx antenna was developed based on a one-layer substrate patch antenna. The radiation patch is a conventional rectangular patch fed at the bottom edge using a 50 Ω microstrip transmission line, as shown in figure 5.6(a). The ground plane, on the other hand, has a grid pattern with periodic cross gaps that divide the metallic ground into small square patches (see figure 5.6(b)). The patterned ground plane and the rectangular radiation patch can be considered a type of metamaterial, namely a RIS structure that acts like a parallel LC resonant circuit [164]. The resonant frequency f_{RIS} of the LC circuit can be

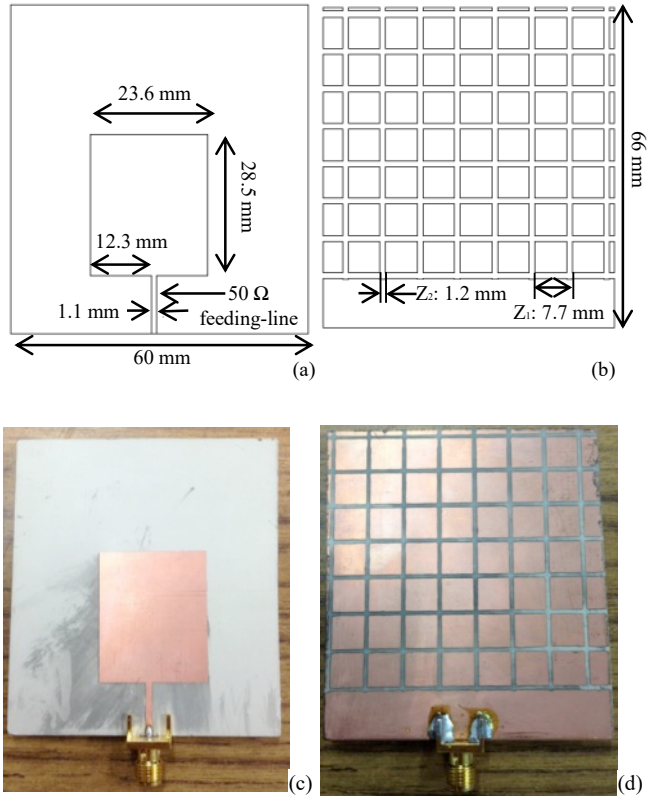

Figure 5.6. UWB Tx/Rx antenna; (a) dimensions of the radiation patch; (b) dimensions of the ground plane; (c) top view of the fabricated antenna; (d) bottom view of the fabricated antenna.

determined when it has the largest impedance. The impedance of the LC circuit can be expressed by the impedance of the equivalent inductor X_L and capacitor X_C,

$$Z_{LC} = j\frac{X_L X_C}{X_C - X_L} \tag{5.4}$$

where X_L and X_C can be calculated as

$$X_L = Z_d \tan(kd) \tag{5.5}$$

and

$$X_C = \frac{K\left(\frac{Z_1}{Z_2}\right)}{2\pi K\left(\sqrt{1-\left(\frac{Z_1}{Z_2}\right)^2}\right)\cdot\left(Z_2 - Z_1\right)} \tag{5.5}$$

in which Z_d and k are the wave impedance and the propagation constant of the substrate material, respectively, d is the substrate thickness, Z_1 and Z_2, as illustrated in figure 5.6(b), define the vertical coordinates of the strip edges, and the function $K(\,)$ is a complete elliptic integral which is defined in [165]. The RIS structure is inductive at frequencies below f_{RIS} while the radiation patch becomes capacitive below its resonant frequency f_{patch}. Therefore, by setting f_{RIS} higher than f_{patch}, the magnetic energy stored in the RIS structure can compensate for the electrical energy stored in the near field of the patch antenna, which results in additional resonances at lower frequencies and thus broadens the bandwidth of the antenna [164].

The design of the UWB Tx/Rx antenna started with a conventional patch antenna having a perfect ground plane. The resonant frequency of the conventional patch antenna f_{patch} was chosen to be at 3.8 GHz, and the resonant frequency of the RIS structure f_{RIS} was selected as 4.2 GHz, which is slightly higher than f_{patch}. Based on the properties of the substrate material and the selected f_{RIS}, the dimensions of the patterned ground, that is, Z_1 and Z_2, can be calculated to be 1.2 mm and

7.7 mm, respectively, using equations (5.4), (5.5) and (5.6). The pictures of the radiation patch and the patterned ground plane of the UWB Tx/Rx antenna, fabricated using the chemical etching technique, are presented in figure 5.6(c) and 5.6(d). The S_{11} parameter of the fabricated antenna was measured and compared with the simulation results in figure 5.7. The bandwidth of the UWB Tx/Rx antenna, determined at the -10 dB reflection coefficient, is 1.6 GHz (i.e., from 1.9 to 3.5 GHz), which matches the simulation well. Compared to the conventional patch antenna, the -10 dB operation bandwidth of the metamaterial antenna increased by more than 100 times. The gain of the Tx/Rx antenna, measured using a two-port transmission test, is presented in figure 5.8. The antenna displayed a relatively flat gain, varying from 3.3 to 4 dBi in frequencies ranging from 2.2 GHz to 3 GHz.

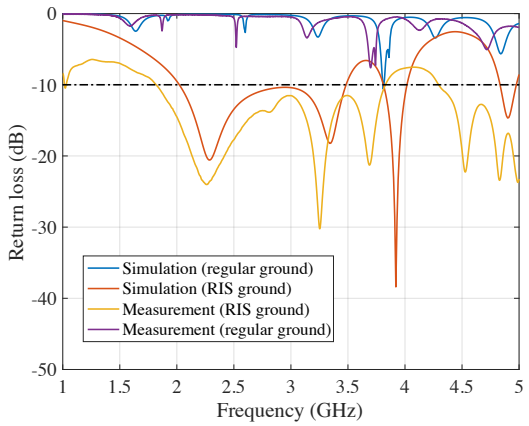

Figure 5.7. A comparison between the simulated and measured S_{11} parameter of the UWB Tx/Rx antenna.

After the performances of the antenna sensor and the Tx/Rx antenna were verified separately using SMA connectors, both antennas were integrated into one RO3210 laminate by connecting them using a 200 mm microstrip transmission line. The entire sensor node was fabricated using chemical etching; the pictures of its front and back surfaces are shown in figure 5.9. This package can be implemented with other temperature resonators; a patch antenna was used

due to ease of fabrication. Although the antenna package was fabricated on the same PCB, a temperature change will have little or no effect on the Tx/Rx antenna as it possesses UWB, and the antenna gain around the operational frequency range is stable (see figure 5.8).

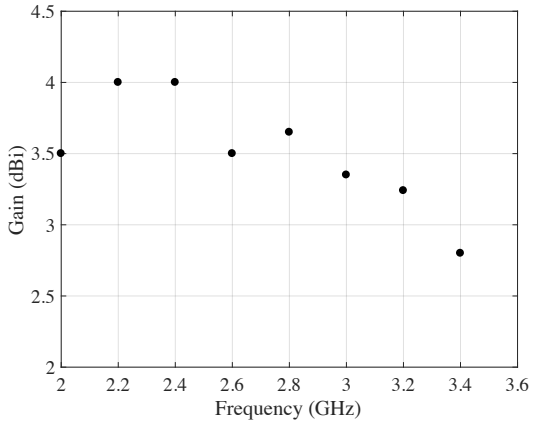

Figure 5.8. The measured radiation gain of the fabricated UWB Tx/Rx antenna.

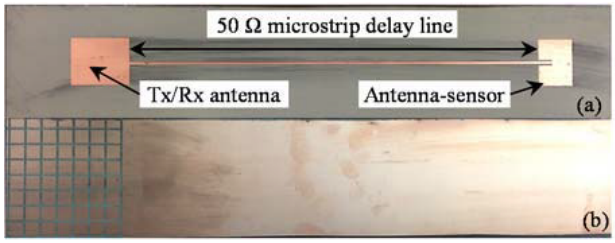

Figure 5.9. The fabricated wireless temperature sensor node; (a) top view (b) bottom view.

5.4 Instrumentation and experimental setup

The experimental setup for validating the temperature sensing capability of the antenna sensor as well as its wireless interrogation is presented in figure 5.10. The sensor node was placed inside an oven so that the environment temperature could be precisely controlled. For wireless interrogation, the metal panel of the oven door was removed but the insulation element was kept in place to prevent heat convention so that a stable temperature could be maintained inside the

oven. The insulation element of the oven was a high-temperature material with a dielectric constant similar to air. Therefore, the insulation material could not introduce any additional changes on the phase or amplitude of the interrogation signal. The wireless interrogator was realized by using a VNA and two horn antennas. The horn antennas were placed at an interrogation distance of 60 cm in front of the temperature oven facing the Tx/Rx antenna. These two horn antennas were connected to a two-port VNA using coaxial cables so that the transmitting S-parameter (i.e., the S_{21} parameter) could be acquired. The VNA was calibrated up to the feeding points of the interrogation antennas, which were 30 cm from the aperture of the interrogation antennas. Therefore, the wireless transmission distance between the feeding points of the integration antennas and the sensor node was 90 cm. The appropriate time gating window was applied during data processing of the acquired signal to extract only the signal from the antenna sensor. Appropriate time gating also helped avoid any reflection from the transmission line if at all there were any. Any temperature gradient along the transmission line will not affect the frequency of the sensor but will affect its amplitude due to impedance mismatch.

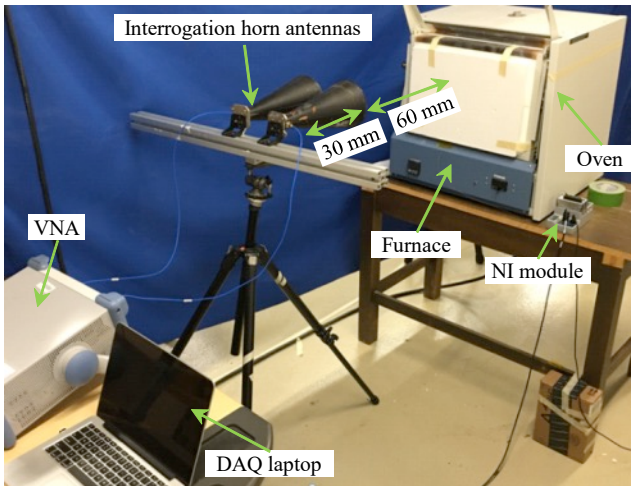

Figure 5.10. The experimental setup for characterizing the antenna for high-temperature sensing.

The sensor node was placed near the entrance of the temperature oven, as indicated in figure 5.11. A T-type thermocouple was installed adjacent to the antenna sensor to obtain the reference temperature. The thermocouple measurements were acquired using a National Instruments (NI) thermocouple module. Both the NI thermocouple module and the VNA were connected to a laptop; the communication between the laptop and the VNA was achieved via a wired local-area-network (LAN) connection while the communication between the computer and the NI module was achieved via a Universal Serial Bus (USB) connection. A LabVIEW program was developed to control the VNA and the NI module. The VNA was programmed to acquire the S_{21} parameters with a frequency resolution of 200 kHz over a frequency range of 2.2 to 3 GHz. The interrogation power was set to be 10 dBm. The S_{21} parameters were recorded every 2.3 seconds. In the meantime, the thermocouple readings were recorded every 0.1 seconds. Both recorded data were time stamped for easy correlation between the thermocouple readings and the resonant frequency extracted from the S21 parameters.

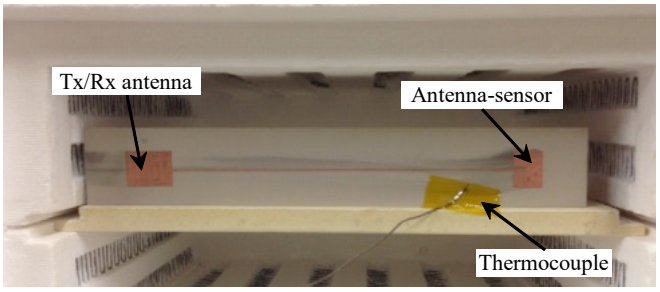

Figure 5.11. The wireless sensor node placed at the entrance of the oven.

5.5 Digital signal processing

A DSP algorithm was developed to extract the resonant frequency of the antenna sensor from the measured S_{21} parameters. The flow chart of the DSP algorithm is provided in figure 5.12(a), and the signals corresponding to each block are presented sequentially in figure 5.12(b). First, the acquired S_{21} parameter, which has a frequency range from f_1 to f_2, is zero padded from the direct current (DC) frequency (i.e., 0 Hz) to f_1. The zero-padded S-parameter is then converted into a time domain signal using Inverse Fast Fourier Transform (IFFT) [166]. Since we are only concerned with the central frequency of the main lobe, applying a window before the first IFFT is not necessary. Representing the backscattered signal in the time domain reveals the arriving times of the signals backscattered by different components. As illustrated in figure 5.12(b), the signals backscattered by the Tx/Rx antenna and the surrounding structures usually have the largest

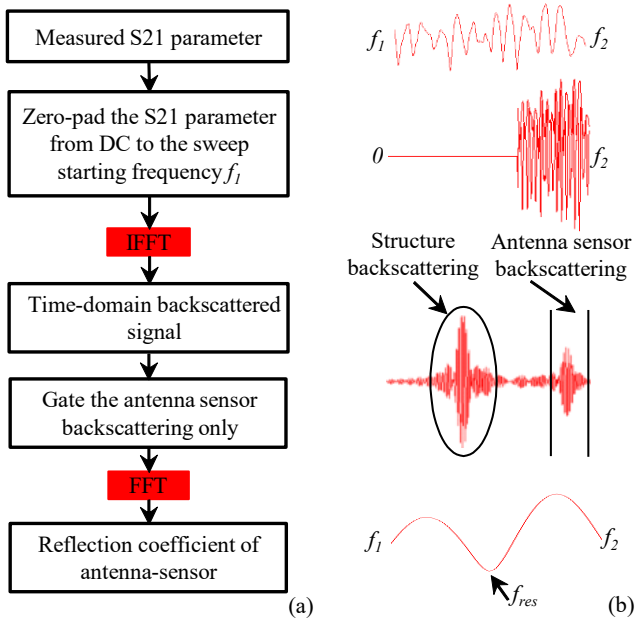

Figure 5.12. The digital signal processing algorithm; (a) flow diagram; (b) signals corresponding to the various processing blocks.

amplitude, but they appear at a different time span from that of the antenna sensor backscattering. Therefore, a time gating window can be applied to the time domain signal to extract the antenna sensor signal. Subsequently, the gated signal is converted back to the frequency domain using FFT, and the resonant frequency of the antenna sensor can be determined as the frequency at which the reflection coefficient has the lowest value.

5.6 Results and discussion

The time domain representation of a typical S_{21} parameter is presented in figure 5.13. Time 0 corresponds to the feeding point of the transmitting interrogation horn antenna. The first wave packet arrives at around 2 ns, which corresponds to a round-trip distance of 0.3 m in the air. This distance coincides with the distance between the feeding point of the interrogation antenna and the antenna aperture. Therefore, we can conclude that this wave packet is due to the cross-talk between the two interrogation horn antennas. The second wave package arrives at around 6 ns, which corresponds to a round-trip distance of 0.9 m in the air, which is the structure mode backscattering generated by the Tx/Rx antenna and the temperature oven. The antenna sensor backscattering occurs at around 9.5 ns. The time difference between the structure mode and the antenna sensor mode is, therefore, around 3.5 ns, which matches the delay time introduced by the transmission line well. In addition, we can also determine the antenna sensor backscattering from the spectrogram of the backscattered signal. The signal backscattered by the antenna sensor should have a low amplitude at its resonant frequency while the structure mode backscattering usually has frequency components over the entire interrogation bandwidth.

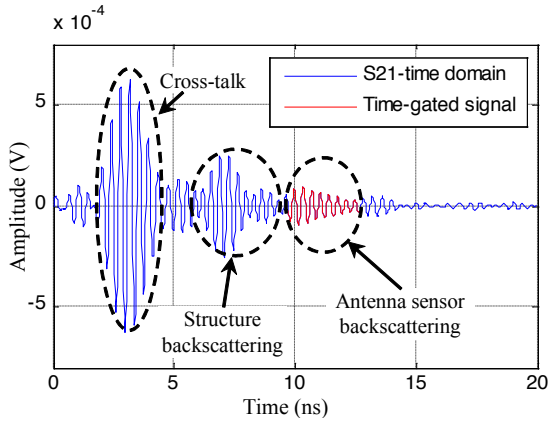

Figure 5.13. The time domain backscattered signal converted from the measured S_{21} parameter.

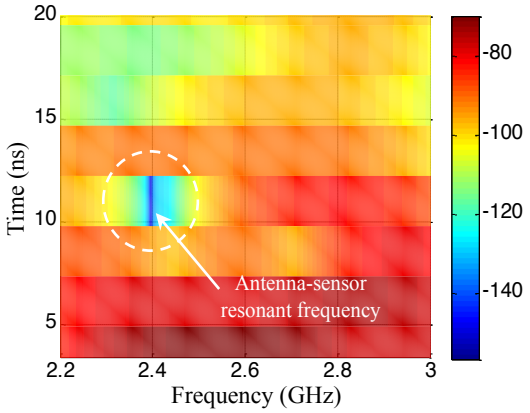

Figure 5.14. The spectrogram of the backscattered signal.

As illustrated in figure 5.14, the spectrogram of the backscattered signal, calculated using Short Time Fourier Transform (STFT), has low energy at around 2.4 GHz starting from 9.5 ns to 12.5 ns, which is the designed antenna resonant frequency. At other time windows, the energy is spread over large frequency spans. Therefore, we can easily determine that the time gating window should be chosen from 9.5 ns to 12.5 ns. The frequency spectra of the time-gated signal at different temperatures are presented in figure 5.15. The resonant frequency of the antenna sensor is determined as the frequencies at which the frequency spectrum has the lowest amplitude. The frequency shifts at different temperatures were normalized with respect to the resonant frequency of the antenna sensor at room temperature. The measured normalized frequency shifts are plotted

versus the temperature change measured from the thermocouple in figure 5.16. The measurement data display a high degree of linearity (R^2 = 0.9972). The slope of the trend line is 195.13 ppm/°C, which is slightly higher than the simulated K_T value of 192.45 ppm/°C. The normalized deviation between the simulated and experimental K_T is 1.39%.

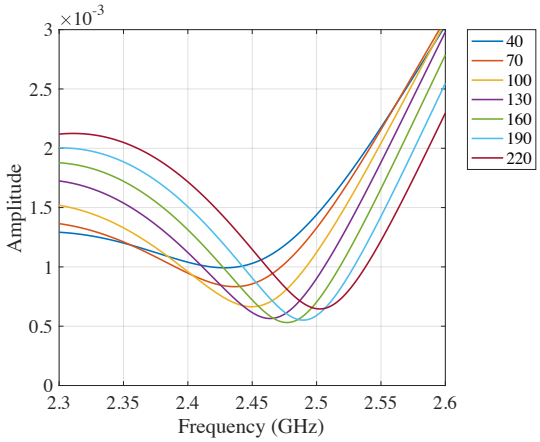

Figure 5.15. The spectra of the gated time-domain signals at different temperatures.

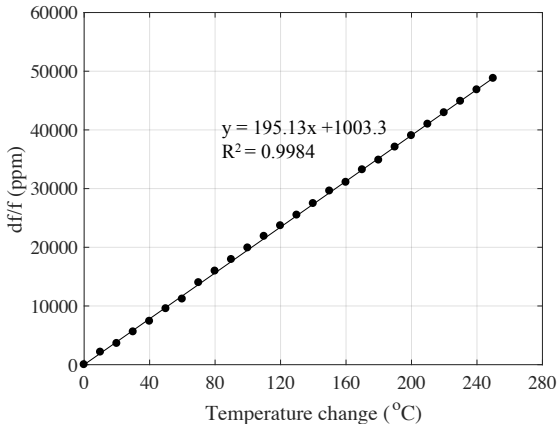

Figure 5.16. The measured relationship between the antenna sensor's normalized resonant frequency shift and the temperature change.

5.7 Conclusion

In this study, a wireless temperature sensor consisting of only microstrip circuit elements and without any electronic components is demonstrated. A wireless interrogation system that can acquire the sensing signal in the far-field of the wireless antenna sensor was developed. Temperature testing up to 280°C was conducted to validate the functionalities of the wireless sensor and its interrogation system. The measured temperature sensitivity of 195.13 ppm/°C agrees with the theoretical prediction.

CHAPTER 6: MEASUREMENT OF THE DIELECTRIC PERMITTIVITY OF PRINTED CIRCUIT BOARD USING MICROSTRIP RESONATORS

6.1 Introduction

The dielectric permittivity measurement is important for practical applications as well as research. Several techniques have been established for measuring the dielectric permittivity of materials [136]. In general, factors such as frequency range, required accuracy of measurement, material properties, material form, sample size, convenience, and cost play an important role in selecting an adequate measurement technique. Among all these techniques, measurements using a microstrip resonator have gained increasing importance since they were first proposed by Troughton [137]. This is probably because of the simplicity of the structure, the ease of fabrication, the accuracy of the measurement technique, the wide frequency band provided by a single microstrip resonator, and the negligible radiation losses [138]. Due to the variability that exists in fabricated PCB, since the broad range of microwave applications requires detailed knowledge of the dielectric permittivity of materials, we investigate the use of a microstrip line resonator (MLR) for dielectric permittivity measurement of PCB.

6.2 Theory of the measurement technique

Troughton presented the first use of a ring-shaped MLR for determining the phase velocities and dispersive characteristics of the microstrip line [137]. After this study, the MLR has gained popularity and has been used for various electromagnetic measurements. The MLR has been widely used for dielectric permittivity measurement of PCBs. The dielectric constant is

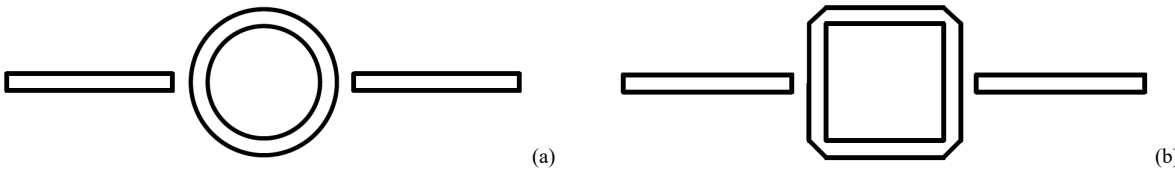

Figure 6.1. An illustration of a microstrip line resonator: (a) a typical ring resonator; (b) the proposed resonator.

inversely obtained by measuring the frequency response of a single port or a two-port MLR using a VNA. Using a two-port MLR, the equation relating the measured frequency response of the MLR and the effective dielectric constant is presented in equation (6.1) as

$$P_m = n\lambda_g \tag{6.1}$$

where P_m is the mean perimeter of the MLR, and $n\lambda_g$ is a harmonic of the wavelength. Figure 6.1(a) presents an illustration of a typical ring-shaped MLR. As shown in figure 6.1, the MLR consists of two microstrip feeding lines, a closed loop transmission line, and the coupling gaps between the microstrip lines and the closed loop transmission line. The main purpose of the microstrip feeding lines and coupling gaps is to couple the signal in and out of the MLR. Because the coupling gaps are capacitive, they cannot be arbitrary and must be carefully chosen to ensure that the frequency response of the MLR does not deteriorate [167]. As suggested in [167], the coupling gaps must be optimized and implemented as a loose coupling to avoid high attenuation caused by large coupling gaps or the shifts in measured resonant frequencies of the MLR caused by small coupling gaps. The coupling gaps can easily be optimized using electromagnetic simulation tools.

The design of the MLR starts by selecting the desired fundamental resonant frequency of the MLR based on an estimated value of the dielectric constant of the PCB used in fabricating the MLR. As presented in equation (6.1), the fundamental resonant frequency of the MLR is obtained by setting n equal to 1. When λ_g increases (i.e., the resonant frequency decreases), the mean

perimeter P_m increases. An inherent advantage of equation (6.1) is that the MLR can be designed for a fundamental frequency that does not match the frequency of interest. One must just ensure that the n^{th} mode of resonance of the MLR corresponds to the desired frequency. For example, if for a given PCB, designing the MLR to operate at a fundamental resonant frequency of 5 GHz makes the ring difficult or impossible to manufacture due to the size of the MLR, one can design the MLR at a fundament frequency of 2.5 GHz. Given that 5 GHz is a multiple of 2.5 GHz, measurements at 5 GHz can be obtained by measuring the frequency response of the second mode of a 2.5 GHz MLR. With the help of a VNA, the frequency response of the MLR can be measured. If the estimated value of the dielectric constant deviates from the actual value of the dielectric constant, the harmonic resonant frequencies of the MLR will deviate from the designed or expected resonant frequencies. From the frequency response and the dimensions of the MLR, the dielectric constant of the PCB can be calculated.

6.2.1 Calculation of the dielectric constant

The dielectric constant at each resonant frequency of the MLR is obtained by iterations based on the method proposed by Kirschning and Jansen [168]. The model accurately predicts the effective dielectric constant of microstrip with validity up to millimeter-wave frequencies. The mathematical expressions presented by Kirschning and Jansen are as follow:

$$\varepsilon_{eff}(f) = \varepsilon_r - \frac{\varepsilon_r - \varepsilon_e}{1 + P(f)} \tag{6.2}$$

where *P(f)* is given as

$$P(f) = P_1 P_2 \left[(0.1844 + P_3 P_4) \times (10 fh) \right] \tag{6.3}$$

P_1, P_2, P_3, and P_4 are expressed as

$$P_1 = 0.27488 + \left[0.6315 + \frac{0.525}{(1 + 0.157 fh)^{20}} \right] \frac{w}{h} - 0.065683 e^{-8.7513 w/h} \tag{6.4}$$

$$P_2 = 0.33622 \cdot \left[1 - e^{-0.3442\varepsilon_r}\right] \quad (6.5)$$

$$P_3 = \left(0.0363e^{-4.6w/h}\right) \cdot \left[1 - e^{-(fh/3.87)^{4.97}}\right] \quad (6.6)$$

$$P_4 = 1 + 2.751 \cdot \left[1 - e^{-(\varepsilon_r/15.916)^8}\right] \quad (6.7)$$

where w, h, ε_r, ε_{eff}, ε_e are the width of the microstrip line, the thickness of the substrate, the dielectric constant, the effective dielectric constant, and the static value of the effective dielectric constant, respectively. To start the iteration process, the measured resonant frequencies of the MLR, the calculated values of the frequency dependent effective dielectric, the initial estimated value of dielectric constant, and the dimensions of the designed MLR are needed.

6.2.2 Calculation of the dissipation factor

The calculation of the dissipation factor at each resonant frequency starts with the determination of the loaded quality factor Q_L at each resonance of the MLR. The loaded quality factor can be calculated using equation (6.8) presented in [167]. The loaded quality factor depends on the resonant frequency f_0 and the bandwidth (usually measured at -3 dB). Q_L can be expressed as

$$Q_L = \frac{f_0}{BW_{-3dB}} \quad (6.8)$$

If the bandwidth cannot be obtained at -3 dB due to asymmetry in the frequency response of the MLR at the desired resonance peak, other techniques such as the Lorenzian fit can be used [169]. This technique has also been suggested for cases where there is a great amount of noise in the frequency response of the MLR.

To determine the dissipation factor, the unloaded quality factor Q_o is needed. Q_o depends on the loaded quality factor Q_L and the measured insertion loss L at the desired resonant frequency of the MLR [167]. Q_o can be expressed as

$$Q_0 = \frac{Q_L}{1-10^{-L/20}} \tag{6.9}$$

where the insertion loss L is in dB. The unloaded quality factor includes conductor losses Q_c, radiation losses Q_r, and dielectric losses Q_d. Therefore, Q_o can be expressed as

$$\frac{1}{Q_0} = \frac{1}{Q_c} + \frac{1}{Q_d} + \frac{1}{Q_r} \tag{6.10}$$

Based on the recommendation found in [142], the radiation losses Q_d can be ignored because there are no open ends in the MLR. Thus, the unloaded quality factor depends only on the conductor losses and the dielectric losses. Q_d and Q_c can be expressed as [170]

$$Q_c = \frac{8.868\pi}{\alpha_c \lambda_g} \tag{6.11}$$

and

$$Qd = \frac{8.868\pi}{\alpha_d \lambda_g} \tag{6.12}$$

where λ_g is the guided wavelength, α_c, and α_d represent the attenuation constants of the conductor and dielectric, respectively. Since the unloaded quality factor depends only on the conductor and dielectric losses of the MLR, the attenuation constant α can be expressed as

$$\alpha = \alpha_c + \alpha_d \tag{6.13}$$

Equation (6.13) can be rearranged to obtain the attenuation constant of the dielectric α_d as

$$\alpha_d = \alpha - \alpha_c = \frac{8.868\pi}{Q_o \lambda_g} - \alpha_c \tag{6.14}$$

Several approximations for the calculation of the attenuation constant of the conductors α_c can be found in textbooks [133], [143]. The most recommended approximations are Pucel *et al.* [171] and Schneider [170]. The surface roughness of the conductors also affects the conductor losses. Morgan [172] proposed an expression to use in conjunction with the equations proposed by Pucel and Schneider to take into account the surface roughness of the conductors when

estimating the attenuation constant of the conductors α_c. The equations for the calculation of the attenuation constant of the conductors used in this study are those proposed by Schneider and they can be found in [143] as

$$\alpha_c = \begin{cases} \dfrac{10}{\pi \ln 10} \cdot \dfrac{R_s}{hZe^{Z/60}} \cdot \left(\dfrac{8h}{w} - \dfrac{w}{4h}\right) \cdot \left(1 + \dfrac{h}{w} + \dfrac{h}{w}\dfrac{\partial w}{\partial t}\right), \dfrac{w}{h} \le 1 \\ \dfrac{ZR_s}{720\pi^2 h \ln 10} \cdot \left[1 + \dfrac{0.44h^2}{w^2} + \dfrac{6h^2}{w^2} \cdot \left(1 - \dfrac{h}{w}\right)^5\right] \\ \times \left(1 + \dfrac{w}{h} + \dfrac{\partial w}{\partial t}\right), \dfrac{w}{h} \ge 1 \end{cases} \tag{6.15}$$

with

$$\frac{\partial w}{\partial t} = \left(\frac{1}{\pi}\right) \ln \frac{4\pi w}{t}, \frac{w}{h} \le \frac{1}{2\pi} \tag{6.16}$$

$$\frac{\partial w}{\partial t} = \left(\frac{1}{\pi}\right) \ln \frac{2h}{t}, \frac{w}{h} \ge \frac{1}{2\pi} \tag{6.17}$$

where ε_{eff} is the effective dielectric constant, η_o is the free space wave impedance [Ω], h is the substrate thickness [m], R_s is the surface resistivity of the conductor strip [Ω/square], t is the thickness of the conductor strip [m], Z the characteristic impedance of the microstrip [Ω], and w the width of the conductor strip (i.e., the microstrip line) [m]. The attenuation constant of the conductors α_c expressed in (6.15) has a unit of dB/unit length. Considering the surface roughness of the conductors, equation (6.15) can be modified as proposed by Morgan [172]. Let α_{cr} be the attenuation constant of the conductors considering the surface roughness of the conductors. α_{cr} can be expressed as [143]

$$\alpha_{cr} = \alpha_c \left\{1 + \frac{2}{\pi} \tan^{-1}\left[1.4\left(\frac{\Delta}{\delta}\right)^2\right]\right\} \tag{6.18}$$

where Δ is the rms surface roughness and δ the skin depth of the electromagnetic wave.

The dissipation factor $\tan\delta$ can be calculated from the dielectric losses using the equation presented by Schneider [173]. Equation (6.19) provides $\tan\delta$

$$\alpha_d = \frac{20\pi}{\ln 10} \cdot \frac{\varepsilon_{eff} - 1}{\varepsilon_r - 1} \cdot \frac{\varepsilon_r}{\varepsilon_{eff}} \cdot \frac{\tan\delta}{\lambda} \tag{6.19}$$

with α_d in dB/unit length.

6.3 Design and fabrication of the microstrip line resonator

Douville [174] conducted an experimental study of microstrip bends and proposed empirical expressions for their compensations. Based on this study, it is suggested to use 45° mitered bends of the microstrip line for optimum compensation. Figure 6.2 presents an illustration of the proposed MLR with a 45° mitered bend. The dimensions of the proposed MLR are obtained using the equations below:

$$a_m = 0.25 P_m \tag{6.20}$$

$$\frac{d_1}{w} = \sqrt{2}\left(1.04 + 1.3e^{-1.35w/h}\right) \tag{6.21}$$

$$d_2 = w\sqrt{2} - d_1 \tag{6.22}$$

where w, a_m, and d_1 represents the microstrip line width, the mean square length, and the mitered bend length, respectively. As presented in (6.19), the length of the bend is a function of the conductor strip w and the thickness of the substrate h. Equation (6.19) is only valid for width to height ratios w/h ≥ 0.25 and $\varepsilon_r \leq 25$.

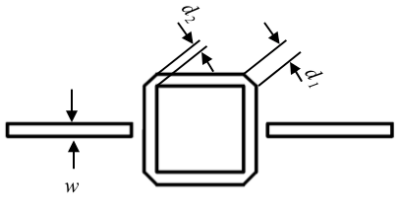

Figure 6.2. The physical design of the proposed microstrip resonator.

For this study, Rogers 3006 was selected as the substrate material for the MLR. The manufacturer specified dielectric constant is 6.15 ± 0.15 with a dissipation factor of 0.002. The substrate thickness was chosen as 1.52 mm. The selected thickness satisfies the width to height ratio *w/h* necessary for the microstrip 45° mitered bend compensation given the microstrip line width *w* of 2.14 mm. The coupling gap g was chosen as 0.53 mm. Based on equation (6.1), the mean square length a_m was calculated as 23.2 mm given the MLR fundamental frequency of 1.5 GHz. The mitered bend length d_1 was calculated as 3.74 mm using equation (6.21). After designing the MLR, it was fabricated using the print-etching technique. Figure 6.3(a) presents the fabricated MLR on Rogers 3006 while figure 6.3(b) presents a comparison between a simulation obtained in Sonnet Pro and measurements obtained from the VNA. As indicated in figure 6.3(b), there was an agreement between simulation and measurement at the resonant frequencies.

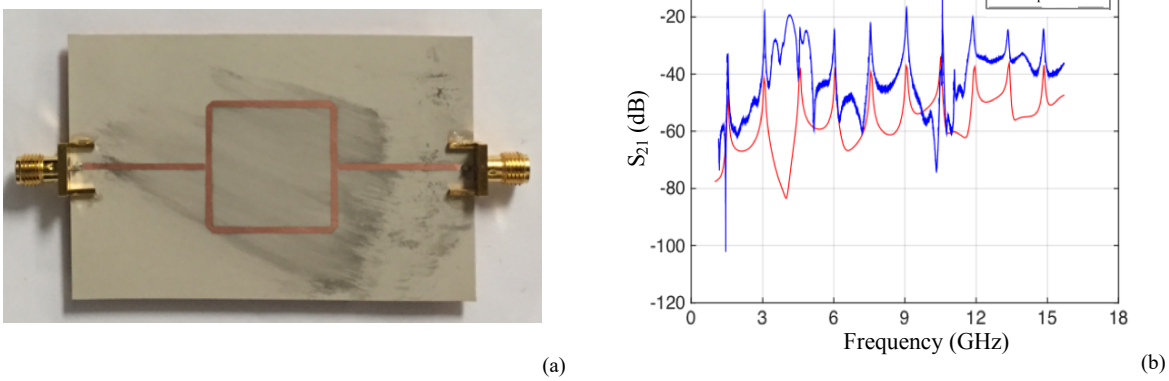

(a) (b)

Figure 6.3. (a)The proposed microstrip line resonator fabricated on Rogers 3006 printed circuit board (PCB) using print-etching technique; and (b) a comparison between simulated and measured S_{21} curves of the resonator.

6.4 Instrumentation and experimental setup

The experimental setup for characterizing the temperature dependency of the dielectric constant of PCB is shown in figure 6.4. A foam box serves as a temperature chamber. To apply heat to the MLR, a hot plate (Cole Parmer, 112001CP) was placed inside the foam box. Since the foam box is not a perfect insulator, a T-type thermocouple was placed adjacent to the MLR to provide temperature readings. The thermocouple was connected to National Instrument NI 9211 thermocouple module for data acquisition. The scattering parameters were acquired using Rohde & Schwarz ZVA24 (i.e., the VNA) connected to the MLR via coaxial cable. Both the VNA and the NI 9211 module were connected to a PC running LabVIEW. The frequency response of the MLR was only measured once the thermocouple reading showed steady-state values of the desired temperature. All measurements were time stamped for ease of correlation during data analysis.

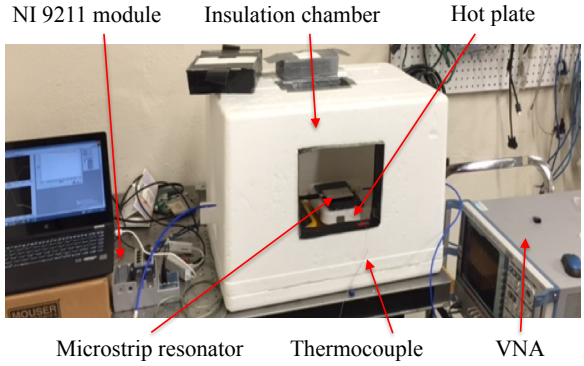

Figure 6.4. The experimental setup for measuring the temperature dependency of the dielectric constant of PCB on which a microstrip line resonator was fabricated

6.5 Discussion

To ensure the proposed MLR is suitable for dielectric property measurement of PCB, the extracted dielectric constant measured at 10 GHz was compared to the manufacturer specified value of 6.15 ± 0.15 with a dissipation factor of 0.002. Using the measurement data and the mathematical equations presented in sections 6.2.1 and 6.2.2, the extracted dielectric constant is 6.17 with a dissipation factor if 0.0022. There is a good agreement between the manufacturer specified values and the measurements. This confirms that the proposed MLR can be used for dielectric constant measurements.

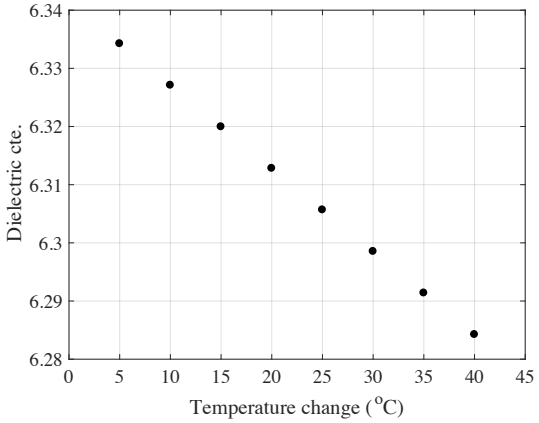

Figure 6.5. The measured relationship between the Rogers 3006 dielectric constant and the temperature change.

One important parameter of PCB is the thermal dependency of the dielectric constant. To measure the thermal coefficient of dielectric constant (TCDk) of the PCB, the MLR was subjected to temperature variations. Figure 6.5 presents the change in dielectric constant due to temperature variation. As shown in figure 6.5, the dielectric constant decreases linearly with an increase in temperature. From the measured data, the extracted TCDk is -226 ppm/^{o}C, which is 14.7% smaller than the manufacturer specified value of -265 ppm/^{o}C, and it is well within the 15% variation often

reported by the manufacturer. Thus, it is important to characterize substrate materials for microwave applications to ensure that the selected substrates or PCB are suitable for the intended applications.

CHAPTER 7: CONCLUSIONS AND FUTURE WORK

7.1 Conclusions

Several achievements were made during this research work. For the first time, simultaneous measurement of multiple parameters using a single antenna sensor was demonstrated. First, we demonstrated that a single microstrip patch antenna with a rectangular radiation patch is capable of sensing strain and temperature simultaneously. A theoretical model representing the normalized antenna resonant frequency shift as linear functions of strain and temperature changes was established and validated by experimental measurements. The theoretical model also suggests that the thermal response of the dielectric substrate should be appropriately selected to achieve a balanced response of the antenna sensor to temperature and strain changes. We also demonstrated that superstrate thickness and temperature could be simultaneously measured using a dual-frequency rectangular patch antenna. The temperature and the superstrate thickness were inversely determined from the measured antenna resonant frequencies. Experiments were conducted using two dielectric materials (Rogers 3003 and ash from charcoal briquettes) as a superstrate. There was a good agreement between the measurands extracted from the frequency response of the antenna sensor to actual input values (i.e., temperature, strain, and superstrate thickness).

In addition to demonstrating multi-modality sensing using a single antenna sensor, we also demonstrated wireless interrogation of a microstrip patch antenna temperature sensor without electronics. The wireless temperature sensor consists only of microstrip circuit elements A wireless interrogation system was also developed to acquire the sensing signal in the far-field of the wireless

antenna sensor. Temperature testing up to 280°C was conducted to validate the functionalities of the wireless sensor and its interrogation system.

Finally, using a microstrip line resonator, we demonstrated adequate measurement of the dielectric constant, the dissipation factor, and the thermal coefficient of the dielectric constant of PCB. The proposed shape of the microstrip line resonator is easy and cost-efficient to fabricate. Using Rogers 3006 commercial PCB as test material, agreement between the measurements and the manufacturer specified values for dielectric constant and dissipation factor was achieved. The findings presented in this dissertation will help coal power plants to progressively evolve to meet the growing demand for safe and efficient power generation.

7.2 Future work

The results presented in this dissertation point to several motivating directions for future work:

1. It is essential to develop flexible dielectric substrates with the desired dielectric permittivity and mechanical properties. These engineered materials could be based on the trade-off between the sensitivities of the antenna sensor to the desired measurands to achieve optimal sensor performance and facilitate simple data processing. This task will further validate the microstrip line resonator method to characterize the dielectric property of the high-temperature material.
2. It would be beneficial to develop an efficient simulation tool of the antenna sensor. This tool would, for instance, aid in sizing the antenna sensor, simulating its scattering parameters, and performing parametric studies on the material properties of the substrate to define the design space.

3. It would be interesting to consider an alternative wireless interrogator system to reduce the interrogator cost while increasing the interrogation speed.
4. It would be beneficial to demonstrate wireless interrogation of multiplexed microstrip patch antennas to realize distributed condition monitoring of structural systems.

REFERENCES

[1] T. Lockwood, “Advanced sensors and smart controls for coal-fired power plant controls for coal-fired power plant,” 2015.

[2] A. Valero and C. Cortés, “Ash fouling in coal-fired utility boilers. Monitoring and optimization of on-load cleaning,” *Prog. Energy Combust. Sci.*, vol. 22, no. 2, pp. 189–200, 1996.

[3] R. E. Barrett and U. S. A. S. R. S. O. B. C. Division, *Slagging and Fouling in Pulverized-coal-fired Utility Boilers: A survey of boiler design practices for avoiding slagging and fouling*. Electric Power Research Inst., 1987.

[4] M. Pronobis, S. Kalisz, and M. Polok, “The impact of coal characteristics on the fouling of stoker-fired boiler convection surfaces,” *Fuel*, vol. 112, pp. 473–482, 2013.

[5] J. G. Singer, *Combustion, fossil power systems: a reference book on fuel burning and steam generation*. Combustion Engineering, 1981.

[6] H. Wang, “Modeling of ash deposition in large-scale combustion facilities burning pulverized coal,” *Prog. Energy Combust. Sci.*, vol. 23, no. 3, pp. 267–282, 1997.

[7] E. Teruel, C. Cortés, L. Ignacio Díez, and I. Arauzo, “Monitoring and prediction of fouling in coal-fired utility boilers using neural networks,” *Chem. Eng. Sci.*, vol. 60, no. 18, pp. 5035–5048, 2005.

[8] Y. Shi and J. Wang, “Ash fouling monitoring and key variables analysis for coal fired power plant boiler,” *Therm. Sci.*, vol. 19, no. 1, pp. 253–265, 2015.

[9] S. Zhang, G. Shen, L. An, Y. Niu, and G. Jiang, “Monitoring ash fouling in power station boiler furnaces using acoustic pyrometry,” *Chem. Eng. Sci.*, vol. 126, pp. 216–223, 2015.

[10] T. Truong, S. Anema, K. Kirkpatrick, and H. Chen, “The use of a heat flux sensor for in-line monitoring of fouling of non-heated surfaces,” *Food Bioprod. Process. Trans. Inst. Chem. Eng. Part C*, vol. 80, no. 4, pp. 260–269, 2002.

[11] R. Jethra, “Improving temperature measurement in power plants – power engineering,” *Power Eng.*, 2013.

[12] K. Qiu, H. Zhang, H. Zhou, B. Zhou, L. Li, and K. Cen, “Experimental investigation of ash deposits characteristics of co-combustion of coal and rice hull using a digital image technique,” *Appl. Therm. Eng.*, vol. 70, no. 1, pp. 77–89, 2014.

[13] B. K. N. Rao, *Handbook of Condition Monitoring*. Kidlington, Oxford, United Kingdom: Elsevier Advanced Technology, 1996.

[14] H. Sohn, C. R. Farrar, F. Hemez, and J. Czarnecki, “A review of structural health monitoring literature 1996 – 2001,” *Third World Conf. Struct. Control*, 2002.

[15] C. R. Farrar and K. Worden, “An introduction to structural health monitoring.,” *Philos. Trans. A. Math. Phys. Eng. Sci.*, vol. 365, no. 1851, pp. 303–315, 2007.

[16] F.-K. Chang, “Structural Health Monitoring 2013, Volume 1 and 2 - A Roadmap to Intelligent Structures,” *DEStech Publ.*, 2016.

[17] K. Worden and J. M. Dulieu-Barton, “An overview of intelligent fault detection in systems and structures,” *Struct. Heal. Monit.*, vol. 3, no. 1, p. 85, 2004.

[18] A. Deraemaeker *et al.*, *New trends in vibration based structural health monitoring*, no. 520. 2010.

[19] W. Staszewski, G. Tomlinson, and C. Boller, *Health monitoring of aerospace structures smart sensor technologies and signal processing*. 2004.

[20] J. P. Lynch and K. J. Loh, “A summary review of wireless sensors and sensor networks for

structural health monitoring," *Shock Vib. Dig.*, vol. 38, no. 2, pp. 91–128, 2006.

[21] V. Giurgiutiu, *Structural health monitoring with piezoelectric wafer active sensors*. 2014.

[22] D. Li, S.-C. M. Ho, G. Song, L. Ren, and H. Li, "A review of damage detection methods for wind turbine blades," *Smart Mater. Struct.*, vol. 24, no. 3, p. 033001, 2015.

[23] S. N. Ishutkin, G. E. Kuz'min, and V. V. Pai, "Thermocouple measurements of temperature in the shock compression of metals," *Combust. Explos. Shock Waves*, vol. 22, no. 5, pp. 582–589, 1986.

[24] P. R. N. Childs, J. R. Greenwood, and C. A. Long, "Review of temperature measurement," *Rev. Sci. Instrum.*, vol. 71, no. 8, pp. 2959–2978, 2000.

[25] K. Shannon and B. Butler, "A review of error associated with thermocouple temperature measurement in fire environments," *... Int. Wildl. Fire Ecol. an Fire ...*, no. October, pp. 7–9, 2003.

[26] M. Pickford, "Strain gauge technology," *J. Mech. Work. Technol.*, vol. 9, no. 3, pp. 332–334, 1984.

[27] R. F. Wolffenbuttel and A. R. Schekkerman, "Integrated instrumentation amplifier for the phase readout of piezoresistive strain gauges," *IEEE Trans. Instrum. Meas.*, vol. 43, no. 6, pp. 906–911, 1994.

[28] S. Kon and R. Horowitz, "A high-resolution MEMS piezoelectric strain sensor for structural vibration detection," *IEEE Sens. J.*, vol. 8, no. 12, pp. 2027–2035, 2008.

[29] S. Tadigadapa and K. Mateti, "Piezoelectric MEMS sensors: State-of-the-art and perspectives," *Meas. Sci. Technol.*, vol. 20, no. 9, 2009.

[30] T. G. Giallorenzi *et al.*, "Optical fiber sensor technology," *IEEE Trans. Microw. Theory Tech.*, vol. 30, no. 4, pp. 472–511, 1982.

[31] B. Lee, “Review of the present status of optical fiber sensors,” *Opt. Fiber Technol.*, vol. 9, no. 2, pp. 57–79, 2003.

[32] A. D. Kersey, “A review of recent developments in fiber optic sensor technology,” *Optical Fiber Technology*, vol. 2, no. 3. pp. 291–317, 1996.

[33] A. K. Singh, Y. Zhu, M. Han, and H. Huang, “Simultaneous load and temperature measurement using Lophine-coated fiber Bragg gratings,” *Smart Mater. Struct.*, vol. 25, no. 11, p. 115019, 2016.

[34] A. K. Singh, S. Berggren, Y. Zhu, M. Han, and H. Huang, “Simultaneous strain and temperature measurement using a single fiber Bragg grating embedded in a composite laminate,” *Smart Mater. Struct.*, vol. 26, no. 11, p. 115019, 2017.

[35] D. Estrin, L. Girod, G. Pottie, and M. Srivastava, “Instrumenting the world with wireless sensor networks,” *2001 IEEE Int. Conf. Acoust. Speech, Signal Process. Proc. (Cat. No.01CH37221)*, vol. 4, pp. 2033–2036, 2001.

[36] K. Romer and F. Mattern, “The design space of wireless sensor networks,” *IEEE Wirel. Commun.*, vol. 11, no. 6, pp. 54–61, 2004.

[37] Q. Tan *et al.*, “Antenna-resonator integrated wireless passive temperature sensor based on low-temperature co-fired ceramic for harsh environment,” *Sensors Actuators, A Phys.*, vol. 236, pp. 299–308, 2015.

[38] J. Yick, B. Mukherjee, and D. Ghosal, “Wireless sensor network survey,” *Comput. Networks*, vol. 52, no. 12, pp. 2292–2330, 2008.

[39] V. C. Gungor and G. P. Hancke, “Industrial wireless sensor networks: Challenges, design principles, and technical approaches,” *IEEE Trans. Ind. Electron.*, vol. 56, no. 10, pp. 4258–4265, 2009.

[40] Z. Lei and W. Zhi, “Integration of RFID into wireless sensor networks: Architectures, opportunities and challenging problems,” in *Proceedings - Fifth International Conference on Grid and Cooperative Computing, GCC 2006 - Workshops*, 2006, pp. 463–469.

[41] M. Kuorilehto, M. Kohvakka, J. Suhonen, P. Hamalainen, M. Hamalainen, and T. D. Hamalainen, *Ultra-Low Energy Wireless Sensor Networks in Practice: Theory, Realization and Deployment*. 2007.

[42] J. M. Reason and J. M. Rabaey, “A study of energy consumption and reliability in a multi-hop sensor network,” *ACM SIGMOBILE Mob. Comput. Commun. Rev.*, vol. 8, no. 1, p. 84, 2004.

[43] H. Huang, “Flexible wireless antenna sensor: A review,” *IEEE Sensors Journal*, vol. 13, no. 10. pp. 3865–3872, 2013.

[44] J. Polastre, R. Szewczyk, and D. Culler, “Telos: Enabling ultra-low power wireless research,” *2005 4th Int. Symp. Inf. Process. Sens. Networks, IPSN 2005*, vol. 2005, pp. 364–369, 2005.

[45] B. F. Spencer, M. E. Ruiz-Sandoval, and N. Kurata, “Smart sensing technology: Opportunities and challenges,” *Struct. Control Heal. Monit.*, vol. 11, no. 4, pp. 349–368, 2004.

[46] M. Ruiz-Sandoval, T. Nagayama, and B. F. Spencer, “Sensor development using berkeley mote platform,” *J. Earthq. Eng.*, vol. 10, no. 2, pp. 289–309, 2006.

[47] J. Hill, R. Szewczyk, A. Woo, S. Hollar, D. Culler, and K. Pister, “System architecture directions for networked sensors,” *ACM SIGOPS Oper. Syst. Rev.*, vol. 34, no. 5, pp. 93–104, 2000.

[48] Y. S. Lin, D. Sylvester, and D. Blaauw, “An ultra low power 1V, 220nW temperature sensor

for passive wireless applications," in *Proceedings of the Custom Integrated Circuits Conference*, 2008, pp. 507–510.

[49] A. Deivasigamani, A. Daliri, C. H. Wang, and S. John, "A review of passive wireless sensors for structural health monitoring," *Modern Applied Science*, vol. 7, no. 2. pp. 57–76, 2013.

[50] C. Sun, J. Cheng, and T. Ohira, *Handbook on advancements in smart antenna technologies for wireless networks*. 2008.

[51] Z. N. Chen, D. Liu, H. Nakano, X. Qing, and T. Zwick, *Handbook of antenna technologies*, vol. 1–4. 2016.

[52] V. Chawla and D. S. Ha, "An overview of passive RFID," *IEEE Commun. Mag.*, vol. 45, no. 9, pp. 11–17, 2007.

[53] S. L. Garfinkel, A. Juels, and R. Pappu, "RFID privacy: An overview of problems and proposed solutions," *IEEE Security and Privacy*, vol. 3, no. 3. pp. 34–43, 2005.

[54] R. Weinstein, "RFID: A technical overview and its application to the enterprise," in *IT Professional*, 2005, vol. 7, no. 3, pp. 27–33.

[55] N. C. Karmakar, *Handbook of Smart Antennas for RFID Systems*. Hoboken, NJ, USA: Wiley, 2010.

[56] N. C. Karmakar, E. M. Amin, and J. K. Saha, *Chipless RFID sensors*. Hoboken, NJ, USA: Wiley, 2016.

[57] K. Opasjumruskit *et al.*, "Self-powered wireless temperature sensors exploit RFID technology," *IEEE Pervasive Computing*, vol. 5, no. 1. pp. 54–61, 2006.

[58] R. Bhattacharyya, C. Floerkemeier, and S. Sarma, "RFID tag antenna based temperature sensing," in *2010 IEEE International Conference on RFID (IEEE RFID 2010)*, 2010, pp.

8–15.

[59] A. P. Sample, D. J. Yeager, P. S. Powledge, A. V. Mamishev, and J. R. Smith, “Design of an RFID-based battery-free programmable sensing platform,” *IEEE Trans. Instrum. Meas.*, vol. 57, no. 11, pp. 2608–2615, 2008.

[60] F. Kocer and M. P. Flynn, “An RF-powered, wireless CMOS temperature sensor,” *IEEE Sens. J.*, vol. 6, no. 3, pp. 557–564, 2006.

[61] C. Xu, P. Gao, W. Che, X. Tan, N. Yan, and H. Min, “An ultra-low-power CMOS temperature sensor for RFID applications,” *J. Semicond.*, vol. 30, no. 4, p. 045003, 2009.

[62] Y. Wang, Y. Jia, Q. Chen, and Y. Wang, “A passive wireless temperature sensor for harsh environment applications,” *Sensors*, vol. 8, no. 12, pp. 7982–7995, 2008.

[63] X. Yi *et al.*, “Passive wireless smart-skin sensor using RFID-based folded patch antennas,” *Int. J. Smart Nano Mater.*, vol. 2, no. 1, pp. 22–38, 2011.

[64] X. Yi, C. Cho, J. Cooper, Y. Wang, M. M. Tentzeris, and R. T. Leon, “Passive wireless antenna sensor for strain and crack sensing - Electromagnetic modeling, simulation, and testing,” *Smart Mater. Struct.*, vol. 22, no. 8, p. 085009, 2013.

[65] X. Yi, T. Wu, Y. Wang, and M. M. Tentzeris, “Sensitivity modeling of an RFID-based strain-sensing antenna with dielectric constant change,” *IEEE Sens. J.*, vol. 15, no. 11, pp. 6147–6155, 2015.

[66] X. Yi, C. Cho, B. Cook, Y. Wang, M. M. Tentzeris, and R. T. Leon, “Design and simulation of a slotted patch antenna sensor for wireless strain sensing,” in *Proceedings of SPIE - The International Society for Optical Engineering*, 2013, vol. 8694, p. 86941J.

[67] D. Li, C. Cho, and Y. Wang, “Patch antenna sensor rosettes for surface strain measurement,” *Smart Infrastruct. Constr.*, vol. 170, no. 2, pp. 39–49, 2017.

[68] S. Merilampi, T. Björninen, L. Ukkonen, P. Ruuskanen, and L. Sydänheimo, "Embedded wireless strain sensors based on printed RFID tag," *Sens. Rev.*, vol. 31, no. 1, pp. 32–40, 2011.

[69] C. Occhiuzzi, C. Paggi, and G. Marrocco, "Passive RFID strain-sensor based on meander-line antennas," *IEEE Trans. Antennas Propag.*, vol. 59, no. 12, pp. 4836–4840, 2011.

[70] S. Preradovic and N. Karmakar, "Chipless RFID tag with integrated sensor," in *2010 IEEE Sensors*, 2010, pp. 1277–1281.

[71] D. Girbau, Á. Ramos, A. Lazaro, S. Rima, and R. Villarino, "Passive wireless temperature sensor based on time-coded UWB chipless RFID tags," *IEEE Trans. Microw. Theory Tech.*, vol. 60, no. 11, pp. 3623–3632, 2012.

[72] A. Pohl, "A review of wireless SAW sensors," *IEEE Trans. Ultrason. Ferroelectr. Freq. Control*, vol. 47, no. 2, pp. 317–332, 2000.

[73] L. M. Reindl, A. Pohl, G. Scholl, and R. Weigel, "SAW-Based radio sensor systems," *IEEE Sens. J.*, vol. 1, no. 1, pp. 69–78, 2001.

[74] V. Kalinin, "Wireless physical SAW sensors for automotive applications," in *IEEE International Ultrasonics Symposium, IUS*, 2011, pp. 212–221.

[75] L. Reindl and W. Ruile, "Programmable reflectors for SAW-ID-tags," *Proc. IEEE Ultrason. Symp.*, pp. 125–130, 1993.

[76] L. M. Reindl and I. M. Shrena, "Wireless measurement of temperature using surface acoustic waves sensors," *IEEE Trans. Ultrason. Ferroelectr. Freq. Control*, vol. 51, no. 11, pp. 1457–1463, 2004.

[77] U. Wolff, F. L. Dickert, G. K. Fischerauer, W. Greibl, and C. C. W. Ruppel, "SAW sensors for harsh environments," *IEEE Sens. J.*, vol. 1, no. 1, pp. 4–13, 2001.

[78] R. Hauser *et al.*, "A wireless SAW-based temperature sensor for harsh environment," *Proc. IEEE Sensors, 2004.*, pp. 860–863, 2004.

[79] J. R. Humphries and D. C. Malocha, "Wireless SAW Strain Sensor Using Orthogonal Frequency Coding," *IEEE Sens. J.*, vol. 15, no. 10, pp. 5527–5534, 2015.

[80] J. R. Humphries and D. C. Malocha, "Passive, wireless SAW OFC strain sensor," in *2012 IEEE International Frequency Control Symposium, IFCS 2012, Proceedings*, 2012, pp. 41–46.

[81] J. Reibel, U. Stahl, T. Wessa, and M. Rapp, "Gas analysis with SAW sensor systems," *Sensors Actuators, B Chem.*, vol. 65, no. 1, pp. 173–175, 2000.

[82] G. Treitz, T. M. A. Gronewold, E. Quandt, and M. Zabe-Kühn, "Combination of a SAW-biosensor with MALDI mass spectrometric analysis," *Biosens. Bioelectron.*, vol. 23, no. 10, pp. 1496–1502, 2008.

[83] M. I. Rocha-Gaso, C. March-Iborra, Á. Montoya-Baides, and A. Arnau-Vives, "Surface generated acoustic wave biosensors for the detection of pathogens: A review," *Sensors*, vol. 9, no. 7, pp. 5740–5769, 2009.

[84] A. Kawalec and M. Pasternak, "Microwave saw humidity sensor," in *16th International Conference on Microwaves, Radar and Wireless Communications, MIKON 2006*, 2007.

[85] F. S. Irani and B. Tunaboylu, "SAW humidity sensor sensitivity enhancement via electrospraying of silver nanowires," *Sensors (Switzerland)*, vol. 16, no. 12, 2016.

[86] A. Kang, C. Zhang, X. Ji, T. Han, R. Li, and X. Li, "SAW-RFID enabled temperature sensor," *Sensors Actuators, A Phys.*, vol. 201, pp. 105–113, 2013.

[87] B. Drafts, "Acoustic wave technology sensors," *IEEE Trans. Microw. Theory Tech.*, vol. 49, no. 4 II, pp. 795–802, 2001.

[88] J. D. Maines and E. G. S. Paige, “Surface-Acoustic-Wave sevices for signal processing applications,” *Proc. IEEE*, vol. 64, no. 5, pp. 639–652, 1976.

[89] J. H. Hines, “Review of recent passive wireless SAW sensor and sensor-tag activity,” in *4th Annual Caneus Fly-By-Wireless Workshop, FBW 11*, 2011, pp. 68–69.

[90] J. C. Butler, A. J. Vigliotti, F. W. Verdi, and S. M. Walsh, “Wireless, passive, resonant-circuit, inductively coupled, inductive strain sensor,” *Sensors Actuators, A Phys.*, vol. 102, no. 1–2, pp. 61–66, 2002.

[91] T. Salpavaara, J. Verho, P. Kumpulainen, and J. Lekkala, “Wireless interrogation techniques for sensors utilizing inductively coupled resonance circuits,” in *Procedia Engineering*, 2010, vol. 5, pp. 216–219.

[92] K. J. Loh, J. P. Lynch, and N. A. Kotov, “Inductively coupled nanocomposite Wireless strain and pH sensors,” in *Smart Structures and Systems*, 2008, vol. 4, no. 5, pp. 531–548.

[93] H. Zhang, Y. Hong, B. Ge, T. Liang, and J. Xiong, “A novel readout system for wireless passive pressure sensors,” *Photonic Sensors*, vol. 4, no. 1, pp. 70–76, 2014.

[94] T. Salpavaara, J. Verho, P. Kumpulainen, and J. Lekkala, “Readout methods for an inductively coupled resonance sensor used in pressure garment application,” in *Sensors and Actuators, A: Physical*, 2011, vol. 172, no. 1, pp. 109–116.

[95] V. Sridhar and K. Takahata, “A hydrogel-based passive wireless sensor using a flex-circuit inductive transducer,” *Sensors Actuators, A Phys.*, vol. 155, no. 1, pp. 58–65, 2009.

[96] J. Lekkala, T. Salpavaara, J. Verho, and J. Riistama, “Simple inductively coupled resonance sensor for ECG and heart rate monitoring,” in *Procedia Engineering*, 2010, vol. 5, pp. 1438–1441.

[97] J. Riistama, E. Aittokallio, J. Verho, and J. Lekkala, “Totally passive wireless biopotential

measurement sensor by utilizing inductively coupled resonance circuits," *Sensors Actuators, A Phys.*, vol. 157, no. 2, pp. 313–321, 2010.

[98] C. A. Balanis, *Antenna Theory Analysis and Design*, 3rd ed. Hoboken, NJ: Wiley, 2005.

[99] X. Guo *et al.*, "Flexible and reversibly deformable radio-frequency antenna based on stretchable SWCNTs/PANI/Lycra conductive fabric," *Smart Mater. Struct.*, vol. 26, no. 10, p. 105036, 2017.

[100] R. K. Yadav, J. Kishor, and R. L. Yadava, "Effects of temperature variations on microstrip antenna," *Int. J. Networks Commun.*, vol. 3, no. 1, pp. 21–24, 2013.

[101] S. Maurya, R. L. Yadava, and R. K. Yadav, "Effect of temperature variation on microstrip patch antenna and temperature compensation technique," *Int. J. Wirel. Commun. Mob. Comput.*, vol. 1, no. 1, p. 35, 2013.

[102] I. Mohammad, V. Gowda, H. Zhai, and H. Huang, "Detecting crack orientation using patch antenna sensors," *Meas. Sci. Technol.*, vol. 23, no. 1, 2012.

[103] I. Mohammad and H. Huang, "Shear sensing based on a microstrip patch antenna," *Meas. Sci. Technol.*, vol. 23, no. 10, 2012.

[104] H. Huang, F. Farahanipad, and A. K. Singh, "A stacked dual-frequency microstrip patch antenna for simultaneous shear and pressure displacement sensing," *IEEE Sensors Journal*, 2017.

[105] H. Cheng, S. Ebadi, X. Ren, and X. Gong, "Wireless passive high-temperature sensor based on multifunctional reflective patch antenna up to 1050 degrees centigrade," *Sensors Actuators, A Phys.*, vol. 222, pp. 204–211, 2015.

[106] J. Sanders, J. Yao, and H. Huang, "Microstrip patch antenna temperature sensor," *IEEE Sens. J.*, vol. 15, no. c, pp. 1–1, 2015.

[107] U. Tata, H. Huang, R. L. Carter, and J. C. Chiao, “Exploiting a patch antenna for strain measurements,” *Meas. Sci. Technol.*, vol. 20, no. 1, p. 015201, 2009.

[108] A. Daliri, A. Galehdar, S. John, C. H. Wang, W. S. T. Rowe, and K. Ghorbani, “Wireless strain measurement using circular microstrip patch antennas,” *Sensors Actuators, A Phys.*, vol. 184, pp. 86–92, 2012.

[109] W. Wang, T. Liu, H. Ge, and M. Liu, “Strain measurement based on microstrip patch antennas,” in *2015 Annual Reliability and Maintainability Symposium (RAMS)*, 2015, vol. 2015–May, pp. 1–6.

[110] J. Yao, S. Tjuatja, and H. Huang, “Real-time vibratory strain sensing using passive wireless antenna sensor,” *IEEE Sens. J.*, vol. 15, no. 8, pp. 4338–4345, 2015.

[111] X. Xu and H. Huang, “Battery-less wireless interrogation of microstrip patch antenna for strain sensing,” *Smart Mater. Struct.*, vol. 21, no. 12, p. 125007, 2012.

[112] I. Mohammad and H. Huang, “Monitoring fatigue crack growth and opening using antenna sensors,” *Smart Mater. Struct.*, vol. 19, no. 5, 2010.

[113] X. Xu and H. Huang, “Multiplexing passive wireless antenna sensors for multi-site crack detection and monitoring,” *Smart Mater. Struct.*, vol. 21, no. 1, 2012.

[114] X. Yi, R. Vyas, C. Cho, C. Fang, J. Cooper, and Y. Wang, “Thermal effects on a passive wireless antenna sensor for strain and crack sensing,” vol. 8345, pp. 1–11, 2012.

[115] M. Lukacs, X. Ren, and X. Gong, “Wirelessly sensing resonant frequency of passive resonators with different Q factors,” in *IEEE Antennas and Propagation Society, AP-S International Symposium (Digest)*, 2011, pp. 1143–1146.

[116] A. T. Blischak and M. Manteghi, “Embedded singularity chipless RFID tags,” *IEEE Trans. Antennas Propag.*, vol. 59, no. 11, pp. 3961–3968, 2011.

[117] S. Deshmukh and H. Huang, “Wireless interrogation of passive antenna sensors,” *Meas. Sci. Technol.*, vol. 21, no. 3, p. 035201, 2010.

[118] D. J. Thomson, D. Card, and G. E. Bridges, “RF Cavity Passive Wireless Sensors With Time-Domain Gating-Based Interrogation for SHM of Civil Structures,” *IEEE Sens. J.*, vol. 9, no. 11, pp. 1430–1438, 2009.

[119] Electronic Communications Committee (ECC), “Measurements using Fast Fourier Transform (FFT),” no. January, 2005.

[120] X. Xu and H. Huang, “Battery-less wireless interrogation of microstrip patch antenna for strain sensing,” *Smart Mater. Struct.*, vol. 21, no. 12, 2012.

[121] A. Daliri, A. Galehdar, W. S. T. Rowe, S. John, C. H. Wang, and K. Ghorbani, “Quality factor effect on the wireless range of microstrip patch antenna strain sensors,” *Sensors (Switzerland)*, vol. 14, no. 1, pp. 595–605, 2014.

[122] a. Bhattacharyya and T. Tralman, “Effects of dielectric superstrate on patch antennas,” *Electron. Lett.*, vol. 24, no. 6, p. 356, 1988.

[123] I. Bahl, P. Bhartia, and S. Stuchly, “Design of microstrip antennas covered with a dielectric layer,” *IEEE Trans. Antennas Propag.*, vol. 30, no. 2, pp. 314–318, 1982.

[124] V. Saidulu and K. S. Rao, “Study of the dielectric superstrate thickness effects on microstrip patch antennas,” *J. Electron. Commun. Eng.*, vol. 11, no. 1, pp. 55–65, 2016.

[125] R. K. Yadav and R. L. Yadava, “Superstrate loaded rectangular microstrip patch antennas - an overview,” *J. Information, Intell. Knowl.*, vol. 3, no. 2, pp. 107–124, 2011.

[126] N. G. Alexópoulos and D. R. Jackson, “Fundamental Superstrate (Cover) Effects on Printed Circuit Antennas,” *IEEE Trans. Antennas Propag.*, vol. 32, no. 8, pp. 807–816, 1984.

[127] R. Kumar and P. Malathi, “Effects of superstrates on the resonant frequency of rectangular

microstrip antennas," *Microw. Opt. Technol. Lett.*, vol. 49, no. 12, pp. 2946–2950, 2007.

[128] H. A. Hammas, "Radiation performance evaluation of microstrip antenna covered With a dielectric layer," *Eng. Technol. J.*, vol. 27, no. 7, pp. 1280–1286, 2009.

[129] H. Cheng, S. Ebadi, and X. Gong, "A low-profile wireless passive temperature sensor using resonator/antenna integration up to 1000°C," *IEEE Antennas Wirel. Propag. Lett.*, vol. 11, pp. 369–372, 2012.

[130] L. G. Stolarczyk and G. L. Stolarczyk, "Ice detection apparatus for transportation safety," US5474261A, 1995.

[131] Telewave Inc., "Types of antenna coatings," 2017. [Online]. Available: https://www.telewave.com/2017/09/18/types-antenna-coatings/.

[132] European Space Agency, "RF testing of antenna coatings," 2016. [Online]. Available: http://www.esa.int/spaceinimages/Images/2016/07/RF_testing_of_antenna_coatings.

[133] R. Garg, *Microstrip antenna design handbook*. 2001.

[134] R. W. Borio and A. A. Levasseur, "Overview of coal ash deposition in boilers.," *ACS Div. Fuel Chem. Prepr.*, vol. 29, no. 4, pp. 193–203, 1984.

[135] S. O. Nelson, "Dielectric properties measurement techniques and applications," *Trans. Am. Soc. Agric. Eng.*, vol. 42, no. 2, pp. 523–529, 1999.

[136] M. S. Venkatesh and G. S. V. Raghavan, "An overview of dielectric properties measuring techniques," *Canadian Biosystems Engineering / Le Genie des biosystems au Canada*, vol. 47. 2005.

[137] P. Troughton, "Measurement techniques in microstrip," *Electron. Lett.*, vol. 5, no. 2, pp. 1968–1969, 1969.

[138] J. M. Heinola, P. Silventoinen, K. Latti, M. Kettunen, and J. P. Stron, "Determination of

dielectric constant and dissipation factor of a printed circuit board material using a microstrip ring resonator structure," *Mikon-2004, Vol 1, Conf. Proc.*, no. 1, pp. 202–205, 2004.

[139] S. R. G. Sofin and R. C. Aiyer, "Measurement of dielectric constant using a microwave microstrip ring resonator (MMRR) at 10 GHz irrespective of the type of overlay," *Microw. Opt. Technol. Lett.*, vol. 47, no. 1, pp. 11–14, 2005.

[140] A. Rashidian, M. Aligodarz, and D. Klymyshyn, "Dielectric characterization of materials using a modified microstrip ring resonator technique," *IEEE Trans. Dielectr. Electr. Insul.*, vol. 19, no. 4, pp. 1392–1399, 2012.

[141] J. M. Heinola and K. Tolsa, "Dielectric characterization of printed wiring board materials using ring resonator techniques: A comparison of calculation models," *IEEE Trans. Dielectr. Electr. Insul.*, vol. 13, no. 4, pp. 717–726, 2006.

[142] T. C. Edwards and M. B. Steer, *Foundations of interconnect and microstrip design: Third edition*. 2013.

[143] B. C. Wadell, *Transmission line design handbook*. 1991.

[144] D. M. Pozar, *Microwave engineering*. New York: Wiley, 1998.

[145] K. R. Carver and J. W. Mink, "Microstrip antenna technology," *IEEE Trans. Antennas Propag.*, vol. 29, no. 1, pp. 2–24, 1981.

[146] Y. T. Lo, D. Solomon, and W. Richards, "Theory and experiment on microstrip antennas," *IEEE Trans. Antennas Propag.*, vol. 27, no. 2, pp. 137–145, 1979.

[147] W. F. Richards, Y. T. Lo, and D. D. Harrison, "An improved theory for microstrip antennas and applications," *IEEE Trans. Antennas Propag.*, vol. 29, no. 1, pp. 38–46, 1981.

[148] F. M. Tchafa and H. Huang, "Microstrip patch antenna for simultaneous strain and

temperature sensing," *Smart Mater. Struct.*, vol. 27, no. 6, pp. 2629–2636, 2018.

[149] Rogers Corporation, "RT/duroid 5870/5880 high frequency laminates." .

[150] J. Davis, *Metals Handbook Desk Edition*. CRC Press, 1998.

[151] R. S. Figliola and D. E. Beasley, *Theory and Design for Mechanical Measurements*, 5th ed. Hoboken, NJ, USA: J. Wiley, 2011.

[152] J. P. Bentley, *Principles of Measurement Systems*, 4th ed. Upper Saddle River, NJ, USA: Pearson Prentice Hall, 2005.

[153] Rogers Corporation, "RO3200 Series Circuit Materials Data Sheet." .

[154] KAB Electro Acoustics, "Dielectric properties of materials." [Online]. Available: https://www.kabusa.com/Dilectric-Constants.pdf.

[155] H. Liu, H. Tan, Q. Gao, X. Wang, and T. Xu, "Microwave attenuation characteristics of unburned carbon in fly ash," *Fuel*, vol. 89, no. 11, pp. 3352–3357, 2010.

[156] U. Kaatze, "Techniques for measuring the microwave dielectric properties of materials," *Metrologia*, vol. 47, no. 2, pp. 91–113, 2010.

[157] J. M. Heinola and P. Silventoinen, "Use of harmonics of microstrip ring resonator structure on determination of dielectric properties," *IEEE Antennas Propag. Soc. AP-S Int. Symp.*, vol. 3 A, pp. 396–399, 2005.

[158] Rogers Corporation, "RO3000 Series Circuit Materials Data Sheet." .

[159] U. Tata, H. Huang, R. L. Carter, and J. C. Chiao, "Exploiting a patch antenna for strain measurements," *Meas. Sci. Technol.*, vol. 20, no. 1, p. 015201, 2009.

[160] W. Emrich, *Handbook of Charcoal Making: The Traditional and Industrial Methods*. Springer Science & Business Media, 1985.

[161] L. F. Chen, C. K. Ong, C. P. Neo, V. V Varadan, and V. K. Varadan, *Microwave*

Electronics: Measurement and Materials Characterization. Wiley, 2004.

[162] J. Yao, "Dynamic wireless interrogation of antenna-sensor in harsh environment," University of Texas at Arlington, 2016.

[163] J. Yao, F. Mbanya Tchafa, A. Jain, S. Tjuatja, and H. Huang, "Far-field interrogation of microstrip patch antenna for temperature sensing without electronics," *IEEE Sens. J.*, vol. 16, no. 19, pp. 7053–7060, 2016.

[164] L. W. Li, Y. N. Li, T. S. Yeo, J. R. Mosig, and O. J. F. Martin, "A broadband and high-gain metamaterial microstrip antenna," *Appl. Phys. Lett.*, vol. 96, no. 16, p. 164101, 2010.

[165] H. Mosallaei and K. Sarabandi, "Antenna miniaturization and bandwidth enhancement using a reactive impedance substrate," *IEEE Trans. Antennas Propag.*, vol. 52, no. 9, pp. 2403–2414, 2004.

[166] H. Huang and T. Bednorz, "Introducing S-parameters for ultrasound-based structural health monitoring," *IEEE Trans. Ultrason. Ferroelectr. Freq. Control*, vol. 61, no. 11, pp. 1856–1863, 2014.

[167] Kai Chang and Lung-Hwa Hsieh, *Microwave ring circuits and related structures*. Wiley, 2004.

[168] M. Kirschning and R. H. Jansen, "Accurate model for effective dielectric constant of microstrip with validity up to millimetre-wave frequencies," *Electron. Lett.*, vol. 18, no. 6, pp. 272–273, 1982.

[169] P. J. Petersan and S. M. Anlage, "Measurement of resonant frequency and quality factor of microwave resonators: Comparison of methods," *Journal of Applied Physics*, vol. 84, no. 6. pp. 3392–3402, 1998.

[170] M. V. Schneider, "Microstrip lines for microwave integrated circuits," *Bell Syst. Tech. J.*,

vol. 48, no. 5, pp. 1421–1444, 1969.

[171] R. A. Pucel, D. J. Mass, and C. P. Hartwig, “Losses in microstrip,” *IEEE Trans. Microw. Theory Tech.*, vol. 16, no. 12, p. 1064, 1968.

[172] S. P. Morgan, “Effect of surface roughness on eddy current losses at microwave frequencies,” *J. Appl. Phys.*, vol. 20, no. 4, pp. 352–362, 1949.

[173] M. V. Schneider, “Dielectric loss in integrated microwave circuits,” *Bell Syst. Tech. J.*, vol. 48, no. 7, pp. 2325–2332, 1969.

[174] R. J. P. Douville and D. S. James, “Experimental study of symmetric microstrip bends and their compensation,” *IEEE Trans. Microw. Theory Tech.*, vol. 26, no. 3, pp. 175–182, 1978.